Study of Unparticle plus Lepton Signatures at CMS

von

Hendrik Jansen

Diplomarbeit in Physik

vorgelegt der

Fakultät für Mathematik, Informatik und Naturwissenschaften
der Rheinisch-Westfälischen Technischen Hochschule Aachen

im Oktober 2009

angefertigt im

III. Physikalischen Institut A
Prof. Dr. Thomas Hebbeker

Abstract

This diploma thesis describes a study of the discovery and exclusion potential of unparticle signatures with the CMS experiment at the LHC at a center-of-mass energy of 10 TeV during early data taking. The reviewed channel contains the real production of a vector unparticle and an associated SM Z boson. As unparticles leave no trace in the detector, missing transverse energy is their dominant indication of existence. The SM Z boson has various decay channels, the muonic one is chosen herein.

"*Unparticle stuff* will astonish us immediately", H. Georgi states in his first unparticle paper in Spring 2007. More than 200 papers published so far containing "unparticle(s)" in the header do not beg to differ. Many new theories for physics beyond the SM involving more or less new particle states try to overcome certain shortcomings of the SM. They all have one thing in common, they are *more particles*. The concept of unparticles is different. It is just **ONE** new object, and it is **NOT** a particle. What constitutes a particle state? Of course the fact that it has a fixed mass eigenvalue. There is *the* electron rest mass, no other. Unparticles are different, occupying a continuous mass spectrum. This is the result of a new symmetry embedded in unparticle theory, extending the Poincaré group by the conformal group.

Unparticle theory provides suitable solutions to some SM problems. But why bother about yet another theory? As the underlying truth is yet to be discovered – hopefully evidences will be collected at the LHC – all theories are equally possible. Theories like the more talked over *supersymmetry* are not more likely just because we have not seen an evidence of them for over 40 years.

In this thesis, discovery and exclusion potentials are derived making use of the CL_s method after separating signal events from SM events making use of a conventional cut-based analysis. The events have been simulated with the full detector simulation.

It is possible to discover a real vector unparticle signature at a one-sided 5σ CL in the muonic channel in 100 pb^{-1} in a certain range of the unparticle parameter space. Adding the electronic decay channel of the Z boson increases the sensitivity and therefore the discovery range. If no signal is present, an exclusion for $\Lambda_{\mathcal{U}} = 2$ TeV of vector unparticles for $1.01 < d_{\mathcal{U}} < 1.24$ can be set at 95% CL, where $d_{\mathcal{U}}$ is the scaling dimension and $\Lambda_{\mathcal{U}}$ is the renormalization scale of the unparticle sector.

Zusammenfassung

Diese Diplomarbeit beschäftigt sich mit der Untersuchung des Entdeckungs- und Ausschließungspotentials von Unparticle-Signaturen mit dem CMS Experiment, welches Teilchenkollisionen am LHC bei einer Schwerpunktsenergie von 10 TeV vermisst und bezieht sich dabei auf eine Datenmenge, die 100 pb^{-1} entspricht. Der untersuchte Kanal enthält die reale Produktion von Vektor-Unparticles und ein assoziiertes SM Z Boson. Da Unparticles keine Spur im Detektor hinterlassen, ist fehlende transversale Energie der dominante Indikator ihrer Präsenz. Das SM Z Boson hat verschiedene Zerfallskanäle, worunter der Myonische in dieser Arbeit gewählt wurde.

"*Unparticle stuff* will astonish us immediately", behauptete H. Georgi in seinem ersten Unparticle-Papier, herausgebracht im Frühjahr 2007. Mehr als 200 veröffentlichte Arbeiten mit "Unparticle(s)" in der Überschrift zeugen von diesem Erstaunen. Es gibt viele neue Theorien für die Physik jenseits des SMs, die alle mehr oder weniger neue Teilchenzustände postulieren. Damit sollen Unzulänglichkeiten des SMs gelöst werden. Sie alle haben eine Sache gemeinsam: Sie postulieren *mehr Teilchen*. Das Konzept der Unparticles verfolgt einen anderen Weg. Nur **EIN** neues Objekt wird eingeführt, und es ist **KEIN** Teilchen im klassischem Sinne. Was macht eigentlich einen Teilchenzustand aus? Natürlich das Faktum, dass es einen fixen Masseneigenwert hat. Es gibt *die* Elektronruhemasse, keine andere. Unparticles unterscheiden sich durch ihr kontinuierliches Massenspektrum. Das ist die Folge der konformen Symmetrie, die in der Unparticle-Theorie eingebunden ist.

Einige Probleme des SM können mit der Einführung von Unparticles gelöst werden. Aber gibt es nicht schon genug Theorien, die genau dies tun? Brauchen wir noch Weitere? Die zugrunde liegende Wahrheit ist immernoch unbekannt und hoffentlich können neue Einblicke mittels des LHCs gewonnen werden. Keine neue Theorie ist a priori zu bevorzugen und die LHC Daten müssen unvoreingenommen analysiert werden.

In dieser Arbeit werden Entdeckungs- und Ausschlusspotential mittels der CL_s-Methode berechnet, nachdem Signalereignisse von SM-Ereignissen durch eine konventionelle, schnittbasierte Analyse getrennt wurden. Die Ereignisse selber wurden mit der vollen Detektorsimulation simuliert.

Es ist möglich in dem untersuchten Kanal für einen beschränkten Bereich des Unparticle-Parameterraumes ein Signal von realen Vektor-Unparticles mit einer Signifikanz größer als 5σ zu finden. Wenn man den Elektronenkanal hinzunimmt, kann die Signifikanz sogar noch gesteigert werden. Sollte kein Signal gefunden werden, kann ein großer Ausschlussbereich abgesteckt werden. Bei einer Unparticle Renormalizierungsskala $\Lambda_{\mathcal{U}}$ von 2 TeV kann das Signal für $1.01 < d_{\mathcal{U}} < 1.24$ mit einem 95% Vertrauensintervall ausgeschlossen werden, wobei $d_{\mathcal{U}}$ die Skalendimension des invarianten Sektors beschreibt.

Contents

Chapter 1

Introduction

"And who cares?", I was asked, and it was a legitimate question, whereon I did not have a prompt answer. The question arose after an exemplification of my thesis' topic at a convivial evening with friends. Of course I can name tens of people who care about my "exotic" topic, but compared to the world population, this is unconvincing. So is there a general interest of the effort being made in particle physics? I think yes. From my very own point of view, young investigators are given the possibility to study new ideas. This stimulates creativity – and creativity is the cornerstone of all copious inventions. The bottom line is, the direct outcome of a thesis in particle physics may only be relevant to particle physicists themselves, but the acquired qualifications are the seeds for yet to be discovered developments.

Maybe people do not appreciate the fact that physicists created a **Standard Model of particle physics** (SM) describing matter as quarks and leptons instead of fire, water, earth, and air, as was suggested by Anaximenes of Miletus. But they do appreciate digital cameras and high-speed internet connections.[1] The development of such technologies would not have been possible with Miletus' very basic model of reality. The SM does not only model matter as quarks and leptons, it describes as well three of the known four forces that interact among them making use of local gauge theories. For the *gravitational* force, the one most perceived by humans, a quantum theory is still lacking. Kids observe the *electromagnetic* force as "funny hairs" after rubbing a rubber balloon off their hair. But ask someone on the streets if they know about the *weak* and the *strong* force. They usually do not. However, the implications of the weak force are well known in nuclear medicine. Scintigraphy is an imaging method that uses radioactive isotopes and relies on the process of radioactive decays in the diagnosis of diseases.

Let's have a look at the question from social science's point of view. Following Maslow's hierarchy of needs [1], physics is, at an outside estimate, the very top of it. Most important are of course *physiological needs* like breathing, food and water, sleep, and sex. As second comes *safety*, representing the security of the own body, the family, health, resources, and property. Next in line are *love* and *esteem* followed by *self-actualization*, under which the exercise of one's job is to be settled, e.g. as a physicist. From my point of view, *satisfaction of curiosity* is somehow missing. Otherwise, the day-to-day television program would be

[1] So does the Nobel committee. The recent Nobel Price in physics (2009) was granted for the development of silicon photo detectors and fiber glass technology.

unexplainable to me. And there would be no reason to report about the start of one of the largest experiments built my humans, the **Large Hadron Collider**. End of summer 2008 the media hyped the prospect of collisions, which ought to be produced by the LHC – unfortunately rather in the light of an imminent apocalypse than with respect to the exciting new phase that particle physicists yearned and still yearn for. "But hey", I have never encountered so many questions from family members and friends about what I do, about what particle physicists do, as during this period of time. The structure of the answers that I gave follow the structure of this thesis, which is the following:

Foremost, an introduction to the Standard Model of particle physics is presented and followed by the new physics under study, the effective theory of unparticles, in Chap. 2. Then, the experimental setup is reviewed containing details about the Large Hadron Collider, the Compact Muon Solenoid and the process of reconstruction of physical objects in CMS, see Chap. 3. Details concerning the Monte Carlo simulation are outlined in Chap. 4. The main aspect of this thesis, the analysis, is presented in detail in Chap. 5.

Units and Conventions

In this thesis *natural* units are used, which are defined by setting

$$\hbar = c = 1. \tag{1.1}$$

Energy, mass, momentum, time, and length are thus measured in the following dimensions of " eV":

$$[\text{energy}] = [\text{mass}] = [\text{momentum}] = [\text{time}]^{-1} = [\text{length}]^{-1} = \text{eV} \tag{1.2}$$

where 1 eV is the energy gain of a particle with charge $e = 1.602 \cdot 10^{-19}$ C traversing a potential difference of 1 V.

Furthermore, where not specified otherwise, the following conventions have been used:

- The Z^0 boson's charge (0) is suppressed.
- The $W^{\pm}$ boson's charge is suppressed.
- The name electron (muon) is used for both, electrons (muons) and positrons (anti-muons). Same holds for neutrinos.

Chapter 2

Theoretical Foundations

2.1 The Standard Model

The *Standard Model* [2–5] of particle physics is one of the main achievements in physics in the last century. It describes electromagnetic, weak, and strong interactions – so three of the known four forces – with high accuracy and stands numerous experimental tests. Matter seems to be built up from point-like, structureless, spin-1/2 fermions. The forces among them are carried by fundamental spin-1 gauge bosons for all but the gravitational force. They are described making use of local gauge theories. Mathematically, a particle is a field in space and time that satisfies certain conditions. The calculations in the massless limit at tree level already match the experimental estimates quite well. To do better, higher order diagrams and more importantly *masses* have to be accounted for. But massive particles can not be described in the SM. One solution is the spontaneous symmetry breaking via the so-called "Higgs-mechanism". Thereby, both, fermions and bosons, can acquire mass by interacting with the *Higgs field*. The spin-0 Higgs boson has evaded discovery so far and is the main missing piece in the puzzle. Furthermore, one has not been able to include gravity in the SM, as a quantum theory of gravity is still lacking. An overview of the particle content in the SM is given in Fig. 2.1.

The SM is a gauge theory, based on the symmetry group $SU(3)_C \otimes SU(2)_L \otimes U(1)_Y$, where C denotes *color*, L *left-handed* and Y *hypercharge*, describing the *strong*, the *weak* and the *electromagnetic* interaction, respectively. The force carriers are spin-1 gauge fields: eight massless gluons, three massive bosons, namely the $W^{\pm}$ and the Z, and the massless photon communicate the respective forces. Hence an object has to be "charged" (with color, weak iso-spin, electric charge) under a certain symmetry to take part in interactions.

Experiments revealed a three-fold generation structure for fermions, that is leptons and quarks, differing only by mass and flavor quantum number, but having the same gauge interaction:

$$\begin{bmatrix} \nu_e & u \\ e^- & d' \end{bmatrix}, \begin{bmatrix} \nu_\mu & c \\ \mu^- & s' \end{bmatrix}, \begin{bmatrix} \nu_\tau & t \\ \tau^- & b' \end{bmatrix}. \tag{2.1}$$

Here, electrons and electron neutrinos have been grouped with up- and down-quarks, as they are the lightest members of each type (charged lepton, neutral lepton, up-type quark, down-type quark). The same mass-ordering scheme has been applied for the other two generations. Each family itself is ordered in SU(2) doublets and singlets for *left-handed*

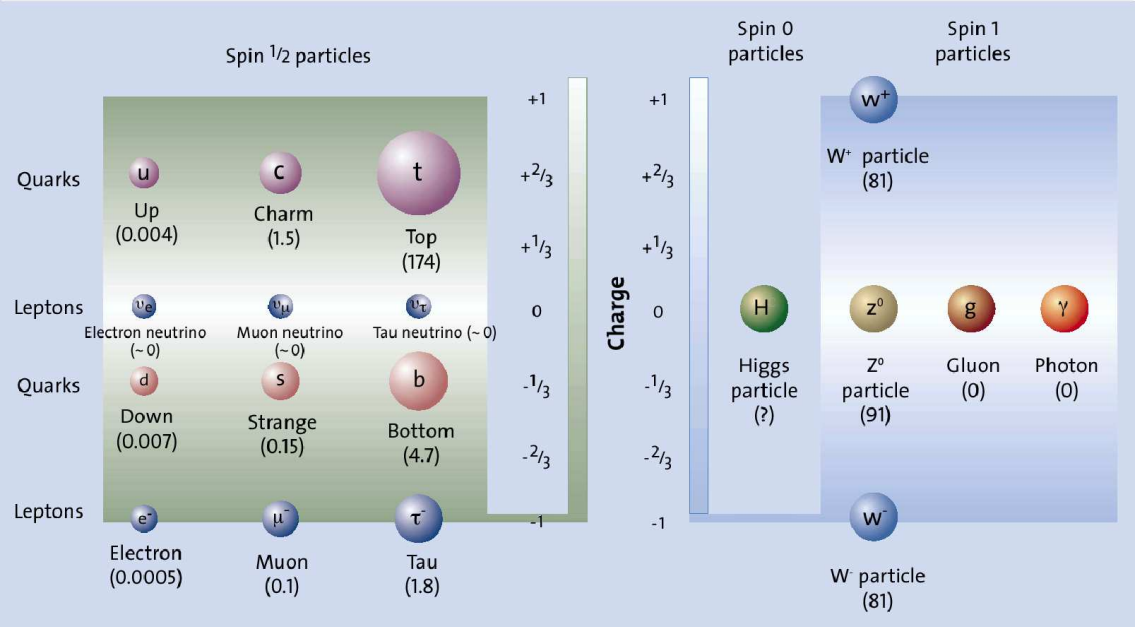

Figure 2.1: *Overview of the Standard Model particles ordered by charge and spin [6]. Masses in* GeV *are given in parentheses.*

and *right-handed* helicity, respectively. The quarks appear with an extra quantum number, *color*, which can be denoted red, blue or green. One generation can be decomposed as:

$$\begin{bmatrix} \nu_l & q_u \\ l^- & q_d \end{bmatrix} \equiv \begin{pmatrix} \nu_l \\ l^- \end{pmatrix}_L + \begin{pmatrix} q_u \\ q_d \end{pmatrix}_L + l_R^- + q_{uR} + q_{dR} \tag{2.2}$$

plus the corresponding antiparticles. The structure allows for an anticipation of a right-handed neutrino ν_R (and the left-handed anti-neutrino $\bar{\nu}_L$), but only ONE left-handed and ONE right-handed neutrino have been observed and declared to be the Dirac neutrinos appearing in the above equations.[1]

For an adequate description, one has to introduce masses into the model, which breaks gauge symmetry. The so called Spontaneous Symmetry Breaking (SSB) of the electroweak group to the electromagnetic subgroup

$$SU(2)_L \otimes U(1)_Y \xrightarrow{\text{SSB}} U(1)_{\text{QED}} \tag{2.3}$$

introduces these masses accommodating a fully symmetric Lagrangian and thus preserving renormalizability.

The fourth interaction, *gravity*, is still not included in the framework of the SM, because a quantum field theory of it is still lacking. Ideas to construct such a theory usually involve a spin-2 *graviton* that mediates the gravitational interaction. As stressed above, not all forces can mediate between all particles. The particle must not be a singlet under the corresponding symmetry group, hence it has do be charged, such that the force can couple to this charge. Gravity is thought to couple to energy. As energy and mass can be seen equivalently, it couples to all known particles.

[1] The difference between ν and $\bar{\nu}$ has been observed in charged pion decays, the Z width suggests a difference between ν_L and ν_R. But it remains unknown, if neutrinos are Dirac or Majorana particles.

The strengths of the four forces, presented in coupling strengths, are shown in Tab. 2.1 along with its approximated range and the corresponding force carrier. The weak interaction is so short ranged due to its massive bosons, the strong one because its bosons take part in strong self-interaction as the gluons carry color themselves. Both gravity and electromagnetic interaction have infinite reach as their potential goes with $1/r$.

Force	coupling strength α_i	Range in m	Carrier
strong	1	10^{-15}	gluon
electromagnetic	10^{-2}	∞	photon (γ)
weak	10^{-6}	10^{-18}	W,Z boson
gravitational	10^{-42}	∞	graviton

Table 2.1: *The fundamental forces sorted by their coupling strength at low energies [7] between a quark and a gluon (strong), two electrons (electromagnetic and gravitational),* u- *and* $\bar{\text{d}}$*-quarks in* π^+ *decays (weak).*

Although gravity is the weakest force of all, it is the one most perceived in everyday live, as a buttered bread tends to fall down when we release it, rather than to hover in the air.[2] Planets and their satellites, the solar system and even galaxies are held together by gravity. Electromagnetic forces are widely known from magnetic toys or electrostatic charging, resulting in funny hairs. Atoms are built from a positively charged nucleus and surrounding negatively charged electrons, which attract each other via the electromagnetic force. The strong force is not something encountered in everyday life, although it binds the individual nucleons to form the nuclei. The weak force is encountered in β-decays, which occur in radioactive nuclei, or e.g. in the sun.

2.1.1 Quantum Electrodynamics

In physics, a very powerful tool is *symmetry*. As we expect physics not to change under certain transformations, e.g. the physics of a billiard shot should be the same no matter from which direction it is looked at, we can use these symmetries to determine certain properties of the physics itself.

Let's see what one can do using symmetry starting with the Lagrangian of a free, massive Dirac fermion:

$$\mathcal{L}_0 = i\overline{\psi}(x)\gamma^\mu\partial_\mu\psi(x) - m\overline{\psi}(x)\psi(x). \tag{2.4}$$

Under a *global* $U(1)$ transformation $\mathcal{L}_0$ is invariant, as phases cancel out:

$$\psi(x) \xrightarrow{\text{U(1)}} \psi'(x) \equiv \exp\{iQ\theta\}\,\psi(x), \tag{2.5}$$

where $Q\theta$ is a pure convention-dependent quantity.[3] θ is called the phase and Q can in general be identified with the fermions charge number (-1 for an electron).[4] Now, one requires symmetry even under *local* phase transformation $\theta = \theta(x)$, which is called "gauge principle". Obviously, $\mathcal{L}_0$ is not invariant under such local gauge transformation, as the

[2] That people say it tends to fall on the buttered side is out of the scope of this work.
[3] Remember that overall phases are not measurable in quantum mechanics.
[4] Note that Q could be different for every fermion without destroying gauge symmetry!

phase's derivative comes into play. To reinstall local symmetry, one introduces a new spin-1 field A_μ, which transforms as

$$A_\mu(x) \xrightarrow{\mathrm{U(1)}} A'_\mu \equiv A_\mu(x) - \frac{1}{e}\partial_\mu\theta(x) \tag{2.6}$$

and the *covariant derivative* is defined as

$$D_\mu\psi(x) \equiv [\partial_\mu + ieQA_\mu(x)]\,\psi(x). \tag{2.7}$$

As desired, D_μ transforms as the field itself and the Lagrangian

$$\mathcal{L} \equiv i\overline{\psi}(x)\gamma^\mu D_\mu\psi(x) - m\overline{\psi}(x)\psi(x) \tag{2.8}$$

holds the required invariance under local $U(1)$ transformation. The introduced field A_μ is invoked by the gauge principle and couples to charged fermions with the strength eQ. For completeness' sake, a gauge-invariant kinetic term of the field is added to the Lagrangian

$$\mathcal{L}_{kin} \equiv -\frac{1}{4}F_{\mu\nu}(x)F^{\mu\nu}(x), \tag{2.9}$$

where $F_{\mu\nu} \equiv \partial_\mu A_\nu - \partial_\nu A_\mu$ is known as the electromagnetic field strength. As the photon is massless ($m_\gamma < 10^{-18}$ [8]), one would like to check if a mass term $\mathcal{L}_{mass} = \frac{1}{2}m^2A^\mu A_\mu$ is forbidden by gauge principle. It is.

2.1.2 Quantum Chromodynamics

Baryons and mesons are observed in a great variety of states pointing to an underlying substructure. Again, the use of symmetry considerations is very beneficial. Assuming mesons to be bound $q\overline{q}$ states and baryons to be bound qqq states, all observed states (and only these states!) are predicted making use of the symmetry group $SU(N)$, where N is the number of considered quark flavors. However, states have been observed that are predicted by symmetry but forbidden by Fermi-Dirac statistics. The Δ^{++} is a spin-3/2 state composed of three u-quarks with the spin configuration $|uuu|\uparrow\uparrow\uparrow\rangle$. To solve this dilemma, a new quantum number is introduced, *color*, coming in $N_C = 3$ flavors: red, blue and green. Therefore baryons can be written as $|q_\alpha q_\beta q_\gamma\rangle$ and mesons as $\left|q_\alpha\overline{q}_\beta\right\rangle$. This would drastically increase the number of predicted states. As no *colorful* mesons nor baryons have been observed, the *confinement hypothesis* is formulated: All asymptotic states are white, that is singlets under rotation in color space. Thus we write the baryon and meson states as:

$$B = \frac{1}{\sqrt{6}}\epsilon^{\alpha\beta\gamma}\,|q_\alpha q_\beta q_\gamma\rangle\,, \qquad M = \frac{1}{\sqrt{3}}\delta^{\alpha\beta}\left|q_\alpha\overline{q}_\beta\right\rangle. \tag{2.10}$$

The introduction of color seems to be quite ad-hoc and an experimental fact proving the existence of this additional quantum number is needed. At a e^+e^--collider, the ratio of the hadronic and muonic cross sections is

$$R_{e^+e^-} \equiv \frac{\sigma(e^+e^- \to hadrons)}{\sigma(e^+e^- \to \mu^+\mu^-)}. \tag{2.11}$$

As color increases the number of possible hadronic final states, the ratio should be sensitive to N_C. Below the Z peak, where the photon propagator dominates for both $e^+e^- \to q\overline{q}$

and $e^+e^- \to \mu^+\mu^-$, the electric charge is mainly responsible for the coupling, and the ratio is given by the sum of the quark electric charges squared:

$$R_{e^+e^-} \approx N_C \sum_{f=1}^{N_f} Q_f^2, \tag{2.12}$$

where N_f is the number of quark flavors actually allowed to be produced by phase space. The measured world average on $R_{e^+e^-}$ clearly shows that $N_C = 3$ [9].

As in QED, one can derive the Lagrangian that includes interaction terms starting from the free, massive quarks and then demanding global and later local symmetry under the appropriate transformation, which is the $SU(3)_C$ transformation in color space. The difference to the QED case is, that now one has to deal with 3×3 instead of 1×1 matrices (being plain numbers), which leads to *eight* spin-1 fields instead of one. Furthermore, 3×3 matrices do not commute. This *non-abelian* behavior leads to additional terms involving triple and quartic gluon interaction.

With q_f^α representing a quark field of flavor f and color α and a vector in color space $q_f^T \equiv (q_f^1, q_f^2, q_f^3)$, one can write the invariant Lagrangian of QCD as

$$\mathcal{L}_{QCD} \equiv -\frac{1}{4} G_a^{\mu\nu} G^a_{\mu\nu} + \sum_f \overline{q}_f (i\gamma^\mu D_\mu - m_f) q_f \quad \text{, with} \tag{2.13}$$

$$D^\mu q_f \equiv \left[\partial^\mu + i g_s \frac{\lambda^a}{2} G_a^\mu(x) \right] q_f, \tag{2.14}$$

where $G_a^{\mu\nu}$ are the gluon field strengths. The invariant derivative D_μ contains the eight gluon fields G_a^μ and the eight generators of the fundamental representation of the $SU(3)$. These are $\frac{1}{2}\lambda^a$ fulfilling the commutation relations

$$\left[\frac{\lambda^a}{2}, \frac{\lambda^b}{2} \right] = i f^{abc} \frac{\lambda^c}{2}, \tag{2.15}$$

where f^{abc} are the $SU(3)$ structure constants.

Gluons have first been discovered at the e^+e^- collider PETRA at DESY and re-discovered at the ALEPH detector at LEP in $Z \to q\overline{q}g$ reactions [10], where a final state quark radiated a gluon. The quark content of baryons and mesons can be probed by deep inelastic scattering of electrons off e.g. protons or pions.

2.1.3 Quantum Flavordynamics

There is more in nature than QED and QCD. E.g. β-decays of certain nuclei or the muon decay cannot be described with the electromagnetic nor the strong force, as they are not capable of handling flavor changing processes. Another experimental fact that only left-handed (right-handed) fermions (anti-fermions) take part in muon decays remains unexplainable as well.

The transition from a charged fermion to an uncharged one, e.g. from an electron neutrino to an electron, is possible in nature; that is why the two are arranged in one doublet. The simplest group allowing for doublet representations, and therefore transitions,

is $SU(2)$. In order to include electromagnetic interactions, the group under consideration is:

$$G \equiv SU(2)_L \otimes U(1)_Y, \tag{2.16}$$

where L denotes left-handed fields and Y is called hypercharge. Starting out with the quark content of a single generation, results are carbon copies for leptons and other generations, we order the fields as in Eq. 2.2:

$$\psi_1(x) = \begin{pmatrix} u \\ d \end{pmatrix}_L, \qquad \psi_2(x) = u_R, \qquad \psi_3(x) = d_R. \tag{2.17}$$

The free Lagrangian is:

$$\mathcal{L}_0 = \sum_{j=1}^{3} i\overline{\psi}_j(x)\gamma^\mu \partial_\mu \psi_j(x) \tag{2.18}$$

and fields transform under global G as:

$$\begin{aligned} \psi_1(x) &\xrightarrow{\text{G}} \psi_1'(x) \equiv \exp\{iy_1\beta\}\, U_L \psi_1(x) \\ \psi_{2,3}(x) &\xrightarrow{\text{G}} \psi_{2,3}'(x) \equiv \exp\{iy_{2,3}\beta\}\, \psi_{2,3}(x), \end{aligned} \tag{2.19}$$

with

$$U_L \equiv \exp\left\{i\frac{\sigma_i}{2}\alpha^i\right\}, \qquad (i = 1, 2, 3) \tag{2.20}$$

acting only on the doublet. In analogy to QED, the $y_{j=1,2,3}$ are called hypercharges, and $\alpha^i(x)$, $\beta(x)$ are the space-time-dependent phases of the transformation. The σ_i are the generators of the fundamental representation of the $SU(2)_L$. Again, they don't commute, leading to self-interactions between the induced fields. The induced fields appear, as in the QED and QCD case, in the covariant derivative, once local gauge symmetry is required:

$$\begin{aligned} D_\mu \psi_1 &\equiv \left[\partial_\mu + ig\widetilde{W}_\mu(x) + ig' y_1 B_\mu(x)\right] \psi_1(x) \\ D_\mu \psi_{2,3} &\equiv \left[\partial_\mu + ig' y_{2,3} B_\mu(x)\right] \psi_{2,3}(x), \end{aligned} \tag{2.21}$$

where

$$\widetilde{W}_\mu(x) \equiv \frac{\sigma_i}{2} W_\mu^i(x) \tag{2.22}$$

is a $SU(2)_L$ matrix field. One obtains four spin-1 fields for four gauge parameters α_i, β. W_μ^1 and W_μ^2 mediate the observed charged-current interaction with $W^\pm = (W_\mu^1 \mp iW_\mu^2)/\sqrt{2}$, the two neutral fields are W_μ^3 and B_μ. These are not the physical γ and Z states, as can easily be seen from Eq. 2.21, since $g' y_j = eQ_j$ in case B_μ represents the photon, but additionally $y_1 = y_2 = y_3$ has to be true as the photon does not distinguish between left-handed and right-handed fields. These two requirements cannot be fulfilled simultaneously. The neutral-current Lagrangian can be re-written in terms of a mixture of B_μ and W_μ^3

$$\begin{pmatrix} W_\mu^3 \\ B_\mu \end{pmatrix} \equiv \begin{pmatrix} \cos\theta_W & \sin\theta_W \\ -\sin\theta_W & \cos\theta_W \end{pmatrix} \begin{pmatrix} Z_\mu \\ A_\mu \end{pmatrix}. \tag{2.23}$$

The mass of the physical Z boson is unequal to zero, which breaks local gauge symmetry. Until the next chapter, let's assume that something breaks the symmetry generating non-zero boson masses and that the neutral mass eigenstates are a mixture of W_μ^3 and B_μ.

Actually, the Higgs-mechanism gives a physical meaning to the mixing angle θ_W. The neutral current Lagrangian re-written in terms of Z_μ and A_μ reads:

$$\mathcal{L}_{\mathrm{NC}} = -\sum_j \overline{\psi}_j \gamma^\mu \left\{ A_\mu \left[g\frac{\sigma_3}{2}\sin\theta_W + g' y_j \cos\theta_W \right] + Z_\mu \left[g\frac{\sigma_3}{2}\cos\theta_W - g' y_j \sin\theta_W \right] \right\} \psi_j. \tag{2.24}$$

The A_μ piece describes QED if the following conditions are imposed:

$$g\sin\theta_W = g'\cos\theta_W = e, \qquad Y = Q - T_3, \tag{2.25}$$

where T_3 is the weak isospin quantum number and the hypercharge Y finally is fixed in terms of this weak isospin and electric charge. Note, that the first equation relates the $SU(2)_L$ and the $U(1)_Y$ couplings to the electromagnetic coupling, unifying both two forces in one *electroweak* force. A table summarizing these quantum numbers for all fermions within one family is given below (Tab. 2.2).

Including the gauge-invariant kinetic terms for the gauge fields, again by constructing corresponding field strengths $B_{\mu\nu}$ and $W^i_{\mu\nu}$, the massless, invariant Lagrangian reads:

$$\mathcal{L}_{QFD,\not{m}} = \sum_{j=1}^{3} i\overline{\psi}_j(x)\gamma^\mu D_\mu \psi_j(x) - \frac{1}{4}B^{\mu\nu}B_{\mu\nu} - \frac{1}{4}W_i^{\mu\nu}W^i_{\mu\nu}. \tag{2.26}$$

This looks nice, as we have obtained the results in the same way for QED and QCD as well, but the big problem is, that it is wrong. The weak gauge bosons are found to be massive particles, but massive bosons would break the gauge symmetry. Likewise unsatisfactory, we started with massless fermions as masses would lead to mixing between right-handed and left-handed states spoiling earlier symmetry considerations. So how to introduce masses, which would break the gauge symmetry without actually breaking it? This is covered in short in the next subsection.

Fermion	Charge	Weak Isospin	Weak hypercharge
	Q	T_3	Y
l_L	-1	-1/2	-1/2
l_R	-1	0	-1
ν_L	0	1/2	-1/2
ν_R	0	0	0
q_{uL}	2/3	1/2	1/6
q_{uR}	2/3	0	2/3
q_{dL}	-1/3	-1/2	1/6
q_{dR}	-1/3	0	-1/3

Table 2.2: *The quantum numbers charge, weak isospin and hypercharge are shown for fermions of one generation.*

2.1.4 Spontaneous Symmetry Breaking

The simplest remedy among others is to introduce an $SU(2)_L$ doublet of complex scalar fields

$$\Phi(x) \equiv \begin{pmatrix} \Phi^{(+)}(x) \\ \Phi^{(0)}(x) \end{pmatrix}, \tag{2.27}$$

with a gauged scalar Lagrangian of the form

$$\mathcal{L}_S = (D_\mu \Phi)^\dagger D^\mu \Phi - \mu^2 \Phi^\dagger \Phi - h\left(\Phi^\dagger \Phi\right)^2 \qquad (h > 0, \mu^2 < 0) \tag{2.28}$$

$$D^\mu \Phi = \left[\partial^\mu + ig\widetilde{W}^\mu + ig' y_\Phi B^\mu\right] \Phi\,, \qquad y_\Phi = Q_\Phi - T_3 = \frac{1}{2}, \tag{2.29}$$

which is invariant under $SU(2)_L \otimes U(1)_Y$ transformations. It introduces an infinite set of degenerate states with minimum energy:

$$\left|\left\langle 0 \left| \Phi^{(0)} \right| 0 \right\rangle\right| = \sqrt{\frac{-\mu^2}{2h}} \equiv \frac{v}{\sqrt{2}}. \tag{2.30}$$

In this minimal extension, where only one $SU(2)$ doublet is introduced, the charged component $\Phi^{(+)}$ cannot acquire a vacuum expectation value, as charge is a conserved quantity.

The introduced doublet contains four degrees of freedom, three are used to give the weak bosons an extra degree of freedom, which means, that they can have a longitudinal component, hence mass, and the fourth is the Higgs field.

A consequence of the symmetry properties of $\mathcal{L}_S$ is the prediction of a relation between the two boson masses M_Z and M_W:

$$M_Z \cos\theta_W = M_W = \frac{1}{2} v g, \tag{2.31}$$

which nicely fits experimental data.

The Higgs boson mass remains as a free parameter in the SM. LEP has set a lower bound of 114 GeV at 95% CL for the SM Higgs mass in direct searches [11]. At Tevatron, the regions between 160 and 170 GeV could be excluded at 95% CL [12]. Via the so-called *Yukawa couplings* the Higgs can as well give masses to fermions. If this is realized in nature, it will be probed at the LHC.

There are known problems and issues that forbid the interpolation of the low-energy SM physics to energies above the TeV scale. Therefore, new physics is expected to show up at this scale and one ansatz to explain these new phenomena involves unparticle physics, which are described in detail in the next section. After introducing unparticles, some SM problems are reviewed and accompanied by their unparticle solution.

2.2 Beyond the Standard Model

The scale invariant sector's particularity is not the production of new heavier particles than those observed in the SM. (An example for such a theory is SUSY [13].) In unparticle physics, the observation of the disappearance of energy is the main characteristic. Unparticles can as well enhance cross sections of particular processes due to virtual effects, but the more striking signatures are those with missing energy.

Since the momentum fractions x_1, x_2 carried by the interacting partons are not known and particles almost collinear to the beam evade detection, the center-of-mass energy of a collision remains unknown. Therefore, a quantity like *missing energy* cannot be used. However, particles collinear to the beam carry little transverse momentum and the colliding partons have small relative angular momentum due to their small impact parameter. Thus, the final transverse energy can be measured precisely and the initial conditions are known as well. Missing transverse energy ($\not{E}_{\mathrm{T}}$) is therefore a meaningful quantity. The evidence of unparticle stuff that has left the detector undetected is therefore $\not{E}_{\mathrm{T}}$.

2.2.1 Conformal Field Theory

Conformal Field Theory (CFT) [14] is a quantum theory, which is invariant under conformal transformations. It provides a framework to understand scale-invariant theories, as conformal invariance includes invariance under scale transformation. Mathematically, the conformal group is the subgroup of coordinate transformations that leaves the metric invariant up to a scale:

$$x \to x' \text{ (change of coordinates)} \quad \Longrightarrow \quad g_{\mu\nu}(x) \to g'_{\mu\nu}(x') = \Omega(x) g_{\mu\nu}(x). \tag{2.32}$$

This allows for additional transformations in Minkowski space. Besides the Poincaré transformations

$$x^\mu \to x'^\mu = \mathbf{\Lambda} x^\mu + a^\mu, \tag{2.33}$$

where $\mathbf{\Lambda}$ is a Lorentz tensor and a^μ a Lorentz vector, there is the scale transformation (dilatation)

$$x^\mu \to x'^\mu = s x^\mu \tag{2.34}$$

with $s \in \mathbb{R}^{>0}$ and the special conformal transformation

$$x^\mu \to x'^\mu = \frac{x^\mu + a^\mu x^2}{1 + 2ax + a^2 x^2}, \tag{2.35}$$

where a^μ is a 4-vector describing the transformation, a (x) the usual norm of the 4-vector a^μ (x^μ), and x^2 the norm squared. Hence, the number of generators increases from 10 (Poincaré) to 15, one for the scale and four for the special conformal transformation. Of course in our case, we are interested in the representations of the conformal group involving operators, which are eigenfunctions of the dilatation generator with an eigenvalue equal to the scaling dimension of the operator. In other words, the operator transforms under $x \to x' = sx$ as

$$O_{\mathcal{U}}(x) \to O'_{\mathcal{U}}(x') = s^{-d} O_{\mathcal{U}}(x). \tag{2.36}$$

Unitarity sets a lower bound on d: $d \geq 1$. Conformal invariance sets the same lower bound for scalar operators, but higher ($d_{\mathcal{U}} > 3$) for vector and even higher ($d_{\mathcal{U}} > 4$) for

tensor operators, see [15] for details. Scale-invariant theories are generally conformal [16]. If conformal invariance is not exactly conserved and only scale invariance was present no bounds can be set, but "no one knows how to build such a theory and it would have to be very odd" [17].

Interesting is the fact that a CFT does not have an S-matrix. The standard definition of asymptotic states is not possible, since a scale determining what is long or short is missing. Hence, nothing can be infinitely separated and therefore the interactions are equally important at all scales. The absence of an S-matrix has a further important implication, as thereby the conformal extension of the Poincaré group evades the Coleman-Mandula-Theorem [18].

2.2.2 Georgi's Scheme

In spring 2007, the theorist H. Georgi proposed a new scenario, where a scale-invariant conformal sector couples to the SM [19–21]. The objects propagating in this scale-invariant sector do not have a discrete mass eigenvalue, but rather a continuous mass distribution unless the mass is zero. Due to this particular feature they are called unparticles. Phenomenologically, the unparticle model is a special case of so-called Hidden Valley models [22] and from theoretical aspects, it is included in HEIDI[5] models [23].

In quantum theory the wave-particle duality manifests itself through a definite dispersion relation $\omega^2 = k^2 + m^2$, where the mass fixes the low-frequency cut-off. But scale-invariant objects cannot have a definite mass unless this mass is zero, since a scale transformation multiplies all dimensional quantities by a rescaling factor raised to the mass dimension, so a nonzero mass is not scale-invariant.

Georgi's scheme goes like this:

The high-energy theory contains the SM Lagrangian, the Lagrangian of the new theory and an interaction term:

$$\mathcal{L} = \mathcal{L}_{\mathrm{SM}} + \mathcal{L}_{\mathcal{BZ}} + \mathcal{L}_{\mathrm{int}}. \tag{2.37}$$

$\mathcal{L}_{\mathrm{int}}$ describes an interaction between the SM and the so-called *Banks-Zaks* ($\mathcal{BZ}$) [24] sector through exchange of particles, not unparticles, with a large mass $M_{\mathcal{U}}$. Unparticle stuff is denoted with the subscript $\mathcal{U}$. We will see later, why the ultraviolet part of the theory is called "$\mathcal{BZ}$". Below $M_{\mathcal{U}}$, we can write the interaction in terms of an effective Lagrangian with non-renormalizable couplings

$$\mathcal{L}_{\mathrm{int}}^{\mathrm{eff}} = \frac{1}{M_{\mathcal{U}}^{d_{\mathcal{BZ}}+d_{\mathrm{SM}}-4}} O_{\mathrm{SM}} O_{\mathcal{BZ}}, \tag{2.38}$$

where O_{SM} ($O_{\mathcal{BZ}}$) represents a SM ($\mathcal{BZ}$) operator and d_{SM} ($d_{\mathcal{BZ}}$) is the dimension of the SM ($\mathcal{BZ}$) operator, respectively. $\mathcal{L}_{\mathcal{BZ}}$ has a non-trivial infrared (IR) fixed point, which emerges in the renormalization group running at the scale $\Lambda_{\mathcal{U}}$. We'll see later what an infrared fixed point is. Below the scale $\Lambda_{\mathcal{U}}$ in the IR, an effective field theory (EFT) in terms of unparticle operators is formulated, where $\mathcal{BZ}$ operators match onto unparticle operators $O_{\mathcal{U}}$ of dimension $d_{\mathcal{U}}$

$$\mathcal{L}_{\mathrm{int}}^{\mathrm{eff}} = \frac{1}{M_{\mathcal{U}}^{d_{\mathcal{BZ}}+d_{\mathrm{SM}}-4}} O_{\mathrm{SM}} O_{\mathcal{BZ}} \rightarrow \mathcal{L}_{\mathrm{IR}}^{\mathrm{eff}} = C_{\mathcal{U}} \frac{\Lambda_{\mathcal{U}}^{d_{\mathcal{BZ}}-d_{\mathcal{U}}}}{M_{\mathcal{U}}^{d_{\mathcal{BZ}}+d_{\mathrm{SM}}-4}} O_{\mathrm{SM}} O_{\mathcal{U}}. \tag{2.39}$$

[5] homophone for **hi**gher **di**mensional

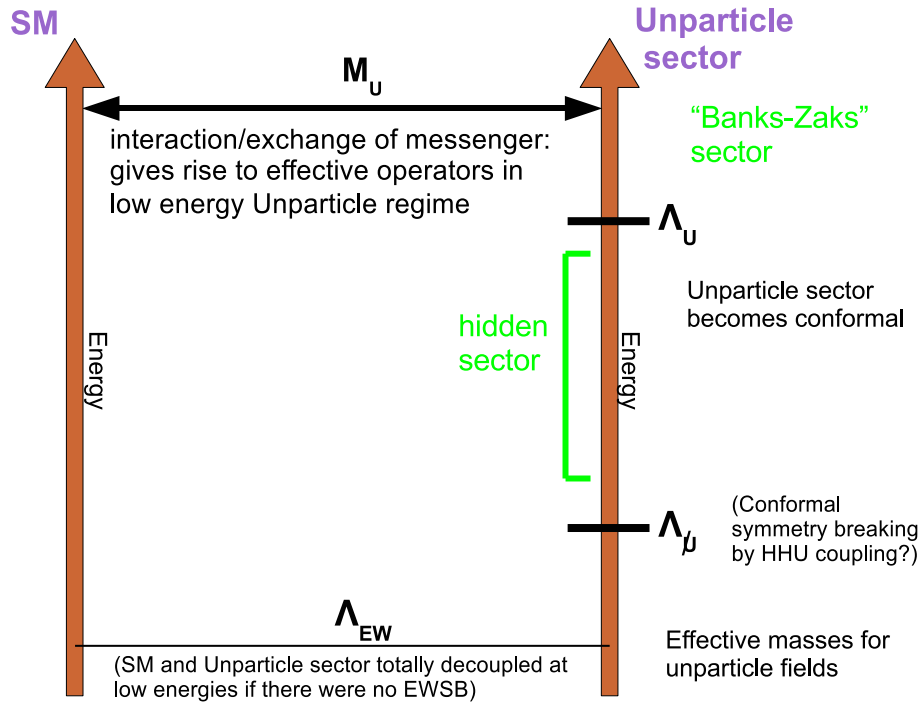

Figure 2.2: *Illustration of Georgi's scheme.*

The unparticle sector in the EFT holds conformal invariance due to the IR fixed point. A conformal invariant theory is as well scale-invariant.[6] This scale invariance constrains certain properties of the theory, e.g. the two-point correlation function for virtual unparticle propagation.

Conformal invariance can be broken at some scale. Details are given below in Sec. 2.2.5. The whole scheme is illustrated in Fig. 2.2.

2.2.3 Infrared Fixed Point

The running of the couplings is usually given by a differential equation of the form

$$\mu \frac{dg}{d\mu} = \beta(g), \tag{2.40}$$

where μ is the scale at which the coupling is probed and β is the β-function describing the evolution. The initial condition is $g(\mu_0) \equiv g_0$, that is, that the coupling is fixed to a certain value g_0 at the scale μ_0. A *fixed point* is then associated with a zero in the β-function $\beta(g) = 0$.

Let g^* be a simple zero of the β-function. In the vicinity of g^* the linear approximation of the β-function is just $\beta(g) = \beta^*(g - g^*)$, with β^* being a constant. A solution of the differential Eq. 2.40 is found to be

$$g(\mu) = g^* + (g_0 - g^*)\mathrm{e}^{\beta^* \ln \frac{\mu}{\mu_0}}. \tag{2.41}$$

[6] No counterexample is known so far.

Now, there are two cases to be looked at: $\beta^* < 0$ and $\beta^* > 0$. For $\beta^* < 0$ and $\mu \to \infty$, we get $g(\mu) \to g^*$, which is called a ultraviolet fixed point, since the energy scale approaches infinity. However, for $\beta^* > 0$ and $\mu \to 0$, we get $g(\mu) \to g^*$ in the infrared limit. This kind of behavior is assumed in Banks-Zaks fields, describing a theory with non-integer number of massless fermions [24].

As stressed above, the IR fixed point makes the IR theory scale-invariant and the operators of the $\mathcal{BZ}$ sector match onto operators of an EFT with conformal symmetry. In order to understand this, we look at the correlation of functions at long distances (low momentum), which can be expressed in terms of a n-point Green's function G [25]

$$\langle \Phi(sx_1), ..., \Phi(sx_n) \rangle \equiv G(sx_1, ..., sx_n; c_i), \tag{2.42}$$

where s is a dimensionless scale factor with $s \gg 1$ for large distances in our case, and the c_i are the coefficients in the action $S = \int d^4x \sum_i c_i \Theta_i(x)$. $\Theta_i(x)$ are operators of dimension d_i, hence the coefficients have dimension $[c_i] = 4 - d_i$. G is in general a function of some coupling strength α and mass m as well, and has the following property:

$$G(sx_1, ..., sx_n; \alpha, m, c_i) = s^{-d_G} G(x_1, ..., x_n; \alpha, s \cdot m, s^{4-d_i} \cdot c_i), \tag{2.43}$$

where d_G is just the scaling dimension of G. Note the appearance of s in front of m! So in order to have a scale-invariant theory at the classical level there must not be a dimensionful parameter, hence masses have to be exactly zero and the dimensions of the unparticle operators have to equal four. This is like in massless QED without quantum effects, where no screening takes place.

However, at the quantum level quantum corrections change the scaling dimension of the operators from their classical value. The change of the scaling properties is associated with the introduction of the new scale μ in the renormalization process. Without going into detail here, the clue is that the renormalization group equations (RGE) are changed due to quantum loops and hence Eq. 2.43 has to be re-written as

$$\begin{aligned} &G(sx_1, ..., sx_n; \alpha(\mu), m(\mu), c_i(\mu); \mu) = \\ s^{-d_G} \exp\left\{ -\int_{\frac{\mu}{s}}^{\mu} d\ln\mu\, \gamma_G \right\} &G(x_1, ..., x_n; \alpha\left(\frac{\mu}{s}\right), s \cdot m\left(\frac{\mu}{s}\right), s^{4-d_i} \cdot c_i\left(\frac{\mu}{s}\right); \mu). \end{aligned} \tag{2.44}$$

This fundamental results tells us a lot. The behavior of the Green functions at large distance (left-hand side), thus $s \gg 1$, is given by the running of the parameters of the theory as functions of the scale factor s. Additionally, the global scaling is modified by the exponential term. γ_G is the so-called anomalous dimension and emerges through the scale transformation; it is a remnant of the application of the RGEs.[7] The same holds true for the operators Θ_i, which have an anomalous dimension γ_i.

So the theory is clearly not scale-invariant, as the coupling parameters depend on the energy scale. The same happens in massless QED, where quantum loops increase the electric charge with increasing energy. So how to re-install scale invariance at a quantum level for the unparticle theory?

[7] Both the operators Θ_i and the Green's function satisfy the RGEs.

The remedy is the IR fixed point. At the IR fixed point, the coupling parameters become *independent* of the energy scale and the anomalous dimensions are constants and a simple covariant scaling is recovered:

$$\begin{gathered} G(sx_1, ..., sx_n; \alpha(\mu), m(\mu), c_i(\mu); \mu) = \\ s^{-d_G} s^{-\gamma_G^*} G(x_1, ..., x_n; \alpha^*, s \cdot m^{1+\gamma_m}, s^{4-d_i-\gamma_i^*} \cdot c_i; \mu), \end{gathered} \tag{2.45}$$

with starred quantities taken at the scale of the IR fixed point. Compared to the classical case, the Green's function scales in the same manner, but with a modified global scaling dimension γ_G^*. Again, with only dimensionless parameters the scale invariance in restored, now in a quantum theory at the IR fixed point. The scaling of an operator at the IR fixed point is then

$$\langle \Theta_i(sx_i, \mu) \rangle = s^{-d_i} \underbrace{\exp\left\{-\gamma_i^* \ln s\right\}}_{s^{-\gamma_i^*}} \langle \Theta_i(x_i; \mu) \rangle \,. \tag{2.46}$$

2.2.4 Effective Theory

As the high-energy theory is not known, we try to extract some physics within an effective theory below the scale $\Lambda_{\mathcal{U}}$, where we write the Lagrangian in terms of SM and unparticle operators. Note the numerous papers about unparticle phenomenology, cf. [26] and references therein.

The unparticle can produce virtual and real effects, showing up in internal lines or being a final state particle, respectively. The two-point correlation function of the virtual unparticle operator is given by, cf. [27],

$$\int d^4x \, \mathrm{e}^{iPx} \left\langle 0 \left| TO(x)O^\dagger(x) \right| 0 \right\rangle = \int \frac{dM^2}{2\pi} \rho_{\mathcal{U}}(M^2) \frac{i}{P^2 - M^2 + i\epsilon}, \tag{2.47}$$

where $TO(x)O^\dagger(x)$ denotes the time-ordered product of the unparticle operators O, M is the mass of the unparticle and P its momentum. Scale-invariance fixes the spectral function $\rho_{\mathcal{U}}$ to be a power of M^2:

$$\rho_{\mathcal{U}}(M^2) = A_{d_{\mathcal{U}}} (M^2)^{d_{\mathcal{U}}-2}. \tag{2.48}$$

$A_{d_{\mathcal{U}}}$ is an arbitrary normalization constant chosen by convention to be [19]

$$A_{d_{\mathcal{U}}} = \frac{16\pi^{5/2}}{(2\pi)^{2d_{\mathcal{U}}}} \frac{\Gamma(d_{\mathcal{U}} + 1/2)}{\Gamma(d_{\mathcal{U}} - 1)\Gamma(2d_{\mathcal{U}})}. \tag{2.49}$$

The phase space then resembles that of $d_{\mathcal{U}}$ massless particles. An unparticle therefore looks like a non-integer number $d_{\mathcal{U}}$ of invisible massless particles. Note that the integral diverges for $d_{\mathcal{U}} \geq 2$, but the theory in the UV is described by non-scale-invariant operators $O_{\mathcal{BZ}}$ and scale-invariance no longer fixes the spectral function as in Eq. 2.48.

The process under study in this thesis is depicted in Fig. 2.3(c,d). It involves a SM coupling of two fermions to a Z boson and a new coupling of two fermions to an unparticle, hence this is real unparticle production. In case the unparticle is an object with Lorentz index μ, hence is a vector unparticle, only t- and u-channel exchange is allowed, whereas a scalar unparticle would allow for an s-channel process as well (a). But this would include

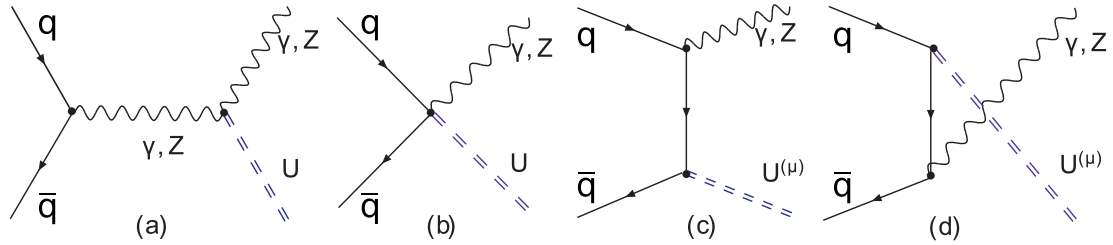

Figure 2.3: *The Feyman graphs are depicted for the process under study. For spin-1 unparticles, only the t-channel and the u-channel contributes (c,d), whereas for spin-0 unparticles the s-channel has non-vanishing contribution as well (a). But this would premise a coupling of the form $ZZ\,\mathcal{U}$, which has not been included yet in Pythia. Also the point-like four vertex interaction (b) has not been considered. So only spin-1 t- and u-channel processes are studied.*

a new coupling $ZZ\,\mathcal{U}$, which has not been accounted for yet. Neither has the point-like four vertex interaction (b) been considered. So only t- and u-channel processes have been studied for the vector case.

Fig. 2.4 shows a mass distribution for two real unparticle scenarios, which have similar properties for the spectral function. Note that this is not the spectral function itself, but rather a convolution of the partonic cross section $\hat{\sigma}$ with the parton density functions. Hence, even for $d_{\mathcal{U}} = 2$ the mass distribution is not flat. The distributions have been produced with the Pythia8 Monte Carlo (MC) generator [28]. More details on MC production are to be found in Sec. 4.1 and Sec. 4.4.

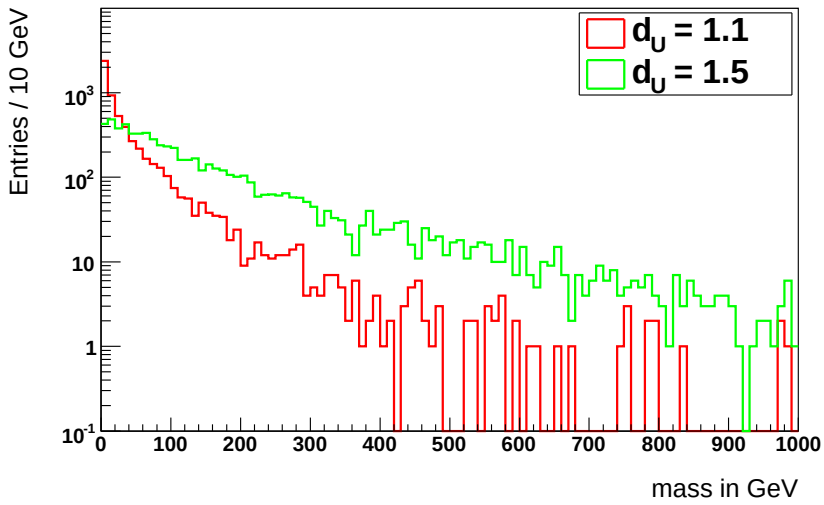

Figure 2.4: *The unparticle mass distribution for two different values of $d_{\mathcal{U}}$ on generator level is shown. For larger $d_{\mathcal{U}}$ higher masses are less suppressed. The plot is shown unnormalized for 10K events at $\sqrt{s} = 10$ TeV. Note the logarithmic scale on the vertical axis.*

The different mass distributions have only a small impact on the kinematics as can be seen from Fig. 2.5, where the p_{T} spectrum of the unparticle is shown for two different values of $d_{\mathcal{U}}$. The spectrum is only a little harder for the higher $d_{\mathcal{U}}$ case.

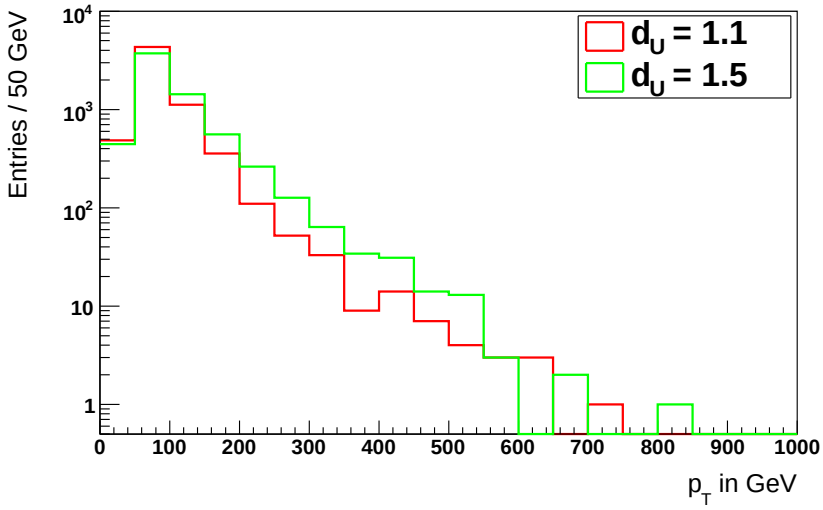

Figure 2.5: *The unparticle p_T distribution for two different values of $d_\mathcal{U}$ on generator level is shown. For larger $d_\mathcal{U}$ the p_T spectrum is slightly harder. The plot is shown unnormalized for 10K events at $\sqrt{s} = 10$ TeV. Note the logarithmic scale on the vertical axis.*

The effective possible couplings of SM fermions to unparticles, cf. Eq. 2.39, are listed below for the scalar, pseudo-scalar, vector and pseudo-vector case [29]. They are expressed in terms of the effective coupling λ, the unparticle renormalization scale $\Lambda_\mathcal{U}$, and the scaling dimension $d_\mathcal{U}$, which are the main free parameters of the theory:

$$\begin{aligned} \text{Spin} - 0: &\quad \frac{\lambda_0}{\Lambda_\mathcal{U}^{d_\mathcal{U}-1}} \overline{f} f O, \frac{\lambda_0'}{\Lambda_\mathcal{U}^{d_\mathcal{U}-1}} \overline{f} i\gamma^5 f O \\ \text{Spin} - 1: &\quad \frac{\lambda_1}{\Lambda_\mathcal{U}^{d_\mathcal{U}-1}} \overline{f} \gamma_\mu f O^\mu, \frac{\lambda_1'}{\Lambda_\mathcal{U}^{d_\mathcal{U}-1}} \overline{f} \gamma_\mu \gamma_5 f O^\mu. \end{aligned} \tag{2.50}$$

In many papers, e.g. [29], it is argued that the couplings λ are of order $\mathcal{O}(1)$.

So what happens once unparticle stuff is produced? In general, unparticles can couple back to SM particles. One example is the decay into two photons [30]. But this is not the usual case, as it is induced by higher order processes. Being a SM singlet, the usual case is to not couple to matter, hence leaving the detector undetected. One should think of unparticle stuff as another way in which energy and momentum can be carried in addition to the usual particle states. In practice energy can simply be carried away by unparticles and effectively disappear [31].

2.2.5 Breaking of Conformal Invariance

In case the unparticle couples to the SM Higgs boson as well, scale invariance is expected to be broken at low energies [32]. In the infrared the coupling is given as:

$$\mathcal{L}_{\text{Higgs}}^{\text{eff}} = C_\mathcal{U} \frac{\Lambda^{d_{\mathcal{BZ}} - d_\mathcal{U}}}{M_\mathcal{U}^{d_{\mathcal{BZ}}-2}} |H^\dagger H| O_\mathcal{U}. \tag{2.51}$$

For $1 < d_\mathcal{U} < 2$ this coupling is relevant in CFT and changes the low energy physics of the unparticle sector significantly. As stressed before, only if no dimensionful parameter

enters the theory it can be scale-invariant. Once the Higgs acquires a vacuum expectation value v, this introduces a scale in the theory and conformal invariance is lost at a scale

$$(\Lambda_{\mathcal{U}})^{4-d_{\mathcal{U}}} = \frac{\Lambda_{\mathcal{U}}^{d_{\mathcal{BZ}}-d_{\mathcal{U}}}}{M_{\mathcal{U}}^{d_{\mathcal{BZ}}-2}} v^2. \tag{2.52}$$

Below $\Lambda_{\mathcal{U}}$ the unparticle sector will probably become a traditional particle sector. This has implications for unparticle studies at certain colliders with typical energy Q, as unparticle physics will only be relevant if

$$\Lambda_{\mathcal{U}} < Q \qquad \Longrightarrow \qquad (Q)^{4-d_{\mathcal{U}}} > \frac{\Lambda_{\mathcal{U}}^{d_{\mathcal{BZ}}-d_{\mathcal{U}}}}{M_{\mathcal{U}}^{d_{\mathcal{BZ}}-2}} v^2. \tag{2.53}$$

2.2.6 Example of a Matrix Element Calculation

The MC generator Pythia8 needs some input to generate processes. To simplify matters, the calculation of the matrix element and the differential cross section for the process $q\overline{q} \to \mathcal{U} + Z$ is shown for the scaler case [33].

As discussed in Sec. 2.2.4, the SM Lagrangian is extended by additional terms such as

$$\mathcal{L} = \frac{O_{\mathcal{U}}}{\Lambda_{\mathcal{U}}^{d_{\mathcal{U}}-1}} \overline{q} \left(\lambda_0 \mathbb{1} + \lambda_0' i\gamma_5\right) q, \tag{2.54}$$

where now scalar λ_0 and pseudo-scalar (λ_0') coupling is considered. Both non-zero λ_0 and λ_0' would break $\mathcal{CP}$, hence only one (λ_0) is chosen to contribute. For a spin-0 unparticle, one has to add amplitudes for the three channels s, t and u. Note that the coupling includes a quark mass factor m_q/v, where v is the electroweak scale, as chirality flipping suppresses the process. The s-channel is not considered, cf. Sec. 2.2.4.

First, we define the Mandelstam variables for the parton process $q\overline{q} \to \mathcal{U}Z$ as

$$s = (p_q + p_{\overline{q}})^2, \quad t = (p_q - p_Z)^2, \quad u = (p_q - P)^2, \tag{2.55}$$

where P is the momentum carried away by the unparticle. For simplicity, we further define

$$\beta = \left(1 + \frac{m_Z^4}{s^2} + \frac{(P^2)^2}{s^2} - 2\frac{m_Z^2 P^2}{s^2} - 2\frac{m_Z^2}{s} - 2\frac{P^2}{s}\right)^{\frac{1}{2}}. \tag{2.56}$$

Then, under the assumption that the Z boson is produced at an angle θ in the center-of-mass frame, t and u can be written as:

$$\begin{aligned} t &= m_Z^2 - \frac{1}{2}\left(s + m_Z^2 - P^2\right)(1 - \beta\cos\theta) \\ u &= m_Z^2 - \frac{1}{2}\left(s + m_Z^2 - P^2\right)(1 + \beta\cos\theta). \end{aligned} \tag{2.57}$$

It can be shown that the amplitude at tree level squared reads:

$$\begin{aligned} |A|^2 = 4\Big[-\frac{s}{t} - \left(1 - \frac{m_Z}{t}\right)\left(1 - \frac{P^2}{t}\right) - \frac{s}{u} - \left(1 - \frac{m_Z}{u}\right)\left(1 - \frac{P^2}{u}\right) \\ +2\left(1 - \frac{P^2}{t}\right)\left(1 - \frac{P^2}{u}\right)\Big], \end{aligned} \tag{2.58}$$

where the first two terms are from t-channel, the next two from u-channel production and the last from the interference term. The spin- and color-averaged matrix element is then:

$$\sum |M|^2 = \left(\frac{1}{4}\right)_{\text{spin}} \left(\frac{1}{3}\right)_{\text{color}} \left(\frac{e^2}{\sin^2\theta_W \cos^2\theta_W}\right) (g_{L,q}^2 + g_{R,q}^2)\lambda_0^2 |A|^2, \tag{2.59}$$

with $g_{L,d} = -\frac{1}{2} + \frac{1}{3}\sin^2\theta_W$, $g_{R,d} = +\frac{1}{3}\sin^2\theta_W$, $g_{L,u} = \frac{1}{2} - \frac{2}{3}\sin^2\theta_W$ and $g_{L,d} = -\frac{2}{3}\sin^2\theta_W$.

Finally, the differential cross section can be written as:

$$d\sigma = \left(\frac{1}{2s}\right)_{\text{flux}} \sum |M|^2 \left(\frac{\beta}{8\pi}\right) \left(\frac{d\cos\theta}{2}\right) A_{d_\mathcal{U}} \left(\frac{P^2}{\Lambda_\mathcal{U}^2}\right)^{d_\mathcal{U}-2} \frac{dP^2}{2\pi\Lambda_\mathcal{U}^2}. \tag{2.60}$$

The inclusive cross section as a function of $d_\mathcal{U}$ and $\Lambda_\mathcal{U}$ is shown in Sec. 4.4.

2.2.7 Some Problems of the SM, and their UNremedies

The SM is tested and validated to high accuracy at low energies. Thus, new theories have to reproduce low energy physics the way the SM does. However, the SM is not capable of making accurate high-energy predictions, as there are known issues.

- The electromagnetic and the weak force are unified to build the electroweak force. This suggests that an overall unification with only one unified coupling could exist at high energies. The running of the coupling in the SM does not achieve such a unification of electromagnetic, weak and strong force.
- The WW scattering is predicted to rise with energy, which violates unitarity at the TeV scale. A SM remedy is the introduction of the Higgs boson, which gives also an explanation for the mechanism of the electroweak symmetry breaking, but it might well be a different mechanism.
- The most probable mass for the Higgs is derived to be around 85 ± 30 GeV, cf. Fig. 2.6 (left), but LEP excluded the Higgs in direct searches up to a mass of 114 GeV [11]. This is only a 1σ deviation and hence statistically not significant, but still a lower bound would be more desirable.
- Electroweak precision measurements at LEP revealed a nearly 3σ deviation in the prediction for the forward-backward asymmetry parameter A_{FB} to its measured value, cf. Fig. 2.6 (right). This may well be only a fluctuation, as many parameters have been fitted, but it might be a hint towards new physics as well.
- Dark Matter has e.g. been observed in rotation curves of galaxies, but we do not know what it is made of. Even worse, only approximately 5% of the content of the universe is baryonic matter, the rest is *dark matter* and the so-called *dark energy* associated with Einstein's cosmological constant.

Many different approaches have been followed trying to overcome these and other issues. Here, some of the solutions involving unparticles are discussed.

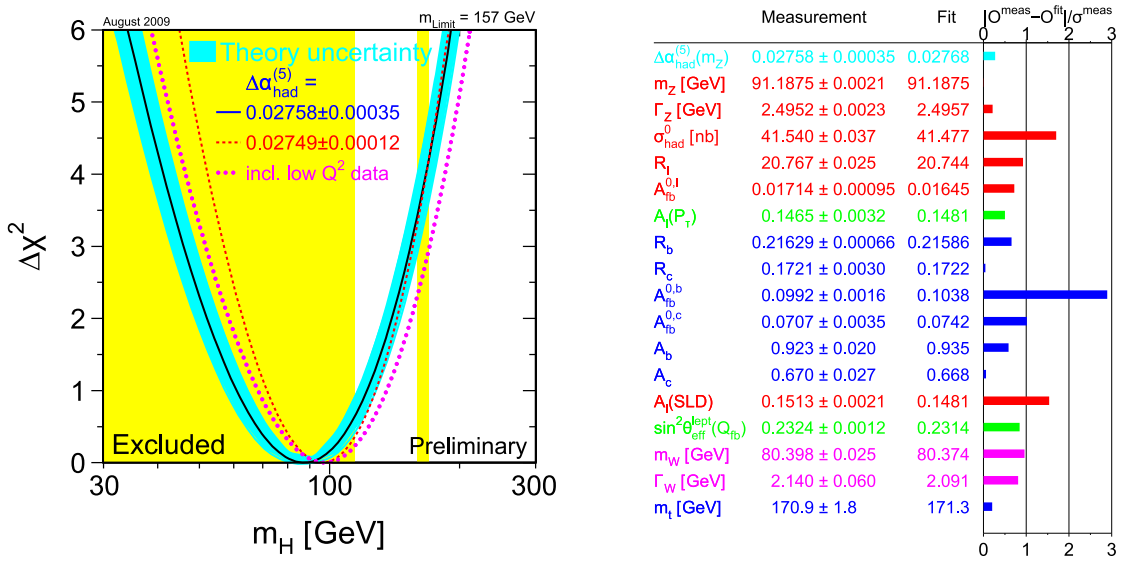

Figure 2.6: ***Left:*** *$\Delta\chi^2 = \chi^2 - \chi^2_{\min}$ versus M_H, from the global fit to the electroweak data. The vertical band indicates the 95% exclusion limit from direct searches.* ***Right:*** *Comparison between the measurements included in the combined analysis of the SM and the results from the global electroweak fit [34, 35].*

Unification

The implementation of new particles, or unparticles, leads to new possible processes. These new internal lines change the evolution of the RGEs, and thus the running of the couplings. In Ref. [36] a coupling of the unparticle sector to the SM Higgs sector is assumed. This breaks the conformal invariance, as described in Sec. 2.2.5, and the unparticle develops a VEV, which works as a threshold correction in the evolution of the SM gauge couplings up to the conformal breaking scale. One such example of a possible alteration is depicted in Fig. 2.7 below. It makes use of a threshold correction at 1 TeV. The couplings unify at approximately 10^{15} GeV.

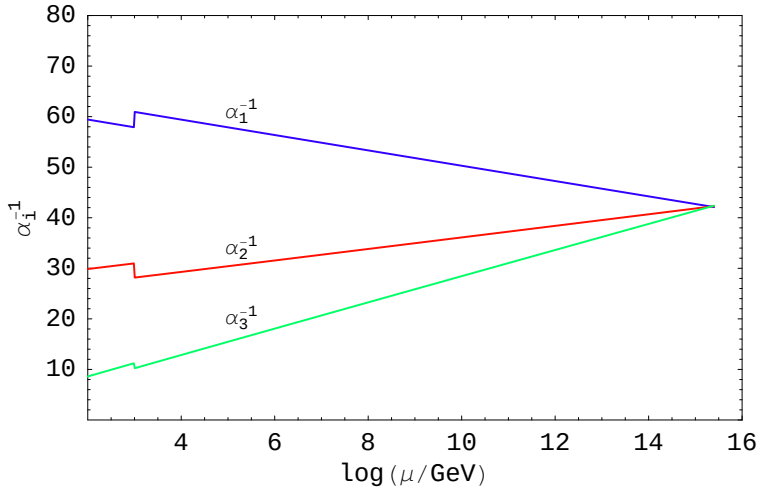

Figure 2.7: *Evolution of α_i^{-1} with unparticle threshold corrections at 1 TeV. Unification occurs at $M_{\rm GUT} = 2 \cdot 10^{15}$ [36].*

WW Unitarity and EWSB

If the Higgs is not a SM Higgs, but is replaced by an unparticle Higgs, aka Unhiggs, things get more complicated. However, the insertion of this Unhiggs leads to new diagrams as shown in Fig. 2.8. These diagrams unitarize the SM WW scattering. Even more, the Unhiggs breaks electroweak symmetry as well. In Ref. [37] more details can be found.

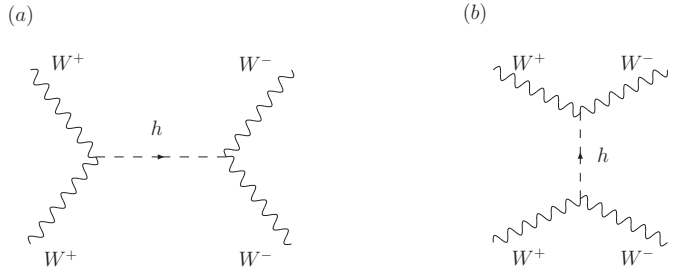

Figure 2.8: *The Unhiggs-WW diagrams are shown.*

LEP Bounds on the Higgs mass

When the Unhiggs h replaces the SM Higgs, there are two ways how this can lower the observed Higgs mass bound. One is to change the branching fraction of $h \to b\bar{b}$ and the other is to suppress the cross section for Unhiggs production in general. Considering the latter, let ξ^2 be the ratio of production cross sections for some Higgs object plus Z boson at LEP for Unhiggs over SM-Higgs:

$$\xi^2 \equiv \frac{\sigma_{Unh}(e^+e^- \to hZ)}{\sigma_{SM}(e^+e^- \to HZ)}. \tag{2.61}$$

The ξ^2 against the scaling dimension $d_{\mathcal{U}}$ is shown in Fig. 2.9. The suppression of the Unhiggs-Gauge couplings allows for an Unhiggs lighter than 114 GeV [37]. Additionally, the mass spectrum of the Unhiggs does not have to be anything close to the one of the SM Higgs.

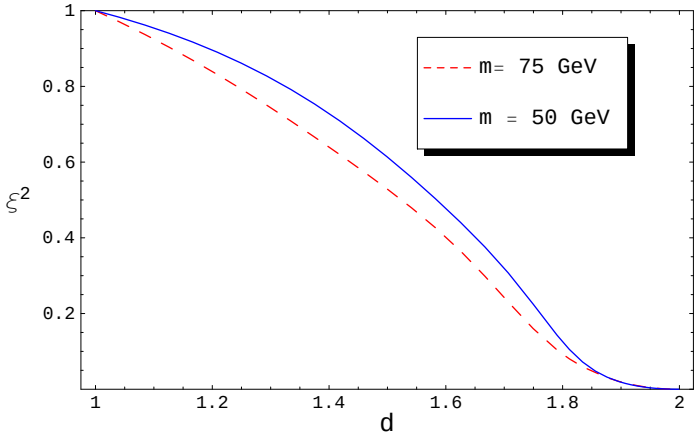

Figure 2.9: *The suppression of the Unhiggs production at LEP for Unhiggs mass of 50 (75)* GeV.

A_{FB} at LEP

The forward-backward asymmetry for production of fermion pairs of flavor f is defined as

$$A_{FB}^{0,f} = \frac{\sigma_F^{0,f} - \sigma_B^{0,f}}{\sigma_F^{0,f} + \sigma_B^{0,f}}, \tag{2.62}$$

where superscript 0 denotes quantities at the Z resonance and

$$\sigma_F^{0,f} = \int_0^{\pi/2} \frac{d\sigma_f^0}{d\cos\theta} d\cos\theta \ , \qquad \sigma_B^{0,f} = \int_{\pi/2}^{\pi} \frac{d\sigma_f^0}{d\cos\theta} d\cos\theta. \tag{2.63}$$

This and other observables have been measured and are compared to a SM global fit [34, 35]. $A_{FB}^{0,f}$ for b-quarks is measured to be 0.0992 ± 0.0016, whereas the SM fit predicts 0.1037 ± 0.0008, which is almost a 3σ deviation. For light quarks, no significant deviation was found, hence a flavor-dependent coupling of unparticles to fermions is needed. Ref. [38] explains, how unparticles can alter the value for $A_{FB}^{0,b}$. The main idea is that unparticles can have a large imaginary contribution in the propagator at the Z resonance and thus interfere with the SM, whereas theories with new heavy particles are out of phase with the SM by almost 90°at this resonance.

Dark Matter

The observed cold dark matter density can be explained with unparticle dark matter, provided a parity is introduced in unparticle physics [39]. Such parity is not assumed in this thesis. Under this parity the unparticle is odd, whereas all SM particles are even. Again, a coupling of the unparticle to a Higgs doublet is required. The electroweak symmetry breaking triggers the acquisition of mass for the unparticle and thus it becomes the WIMP[8] dark matter candidate. Evaluating the relic abundance of unparticle dark matter, the WMAP allowed region gives rise to an unparticle mass around the electroweak scale, cf. Fig. 2.10.

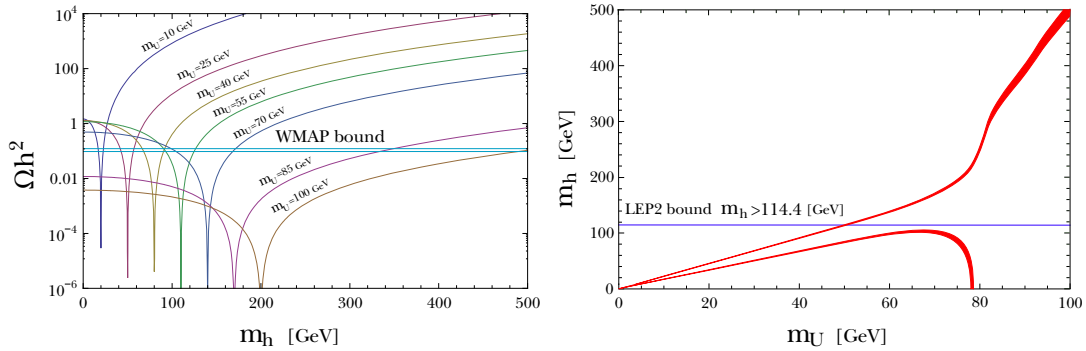

Figure 2.10: ***Left:*** *The relic abundance of the unparticle dark matter as a function of the Higgs boson mass for fixed unparticle masses, together with the WMAP measurements,* $0.096 \leq \Omega_{\mathcal{U}} h^2 \leq 0.122$. ***Right:*** *The contour plot of the relic abundance of the unparticle dark matter* Ωh^2 *in* $(m_{\mathcal{U}}, m_h)$*-plane. The two thin, shaded areas are the allowed regions for the WMAP measurements at* 2σ *confidence level [39].*

[8] **W**eakly **I**nteracting **M**assive **P**article

Chapter 3

Experimental Setup

3.1 The Large Hadron Collider

3.1.1 Collider Physics

Various experiments have been built over the last decades reaching higher and higher center-of-mass energies and thereby opening new windows to explore properties of the underlying truth. Two main designs exist, the fixed-target experiment and the collider. While there are different pros and cons, one main argument for the collider setup is that the maximum center-of-mass energy is higher. For a fixed-target experiment, the relation between the beam energy E_{beam} and the center-of-mass energy E_{cm}, commonly referred to as $\sqrt{s}$, is

$$\sqrt{s} = E_{\text{cm}} = \sqrt{2E_{\text{beam}}m_p}, \tag{3.1}$$

whereas the relation for two colliding beams is

$$\sqrt{s} = E_{\text{cm}} = 2E_{\text{beam}}. \tag{3.2}$$

But why do we ramp up our collider energies? As presented in the last chapter, the SM has open questions and their answers could well be found in high-energy experiments. Many new theories predict solutions involving new heavy particles, and these new particles can best be probed by producing them, which requires at least a center-of-mass energy of the particle's mass. Otherwise its existence could only be seen in indirect measurements, hence in cross sections deviating from the SM predictions. Similar arguments hold true for unparticles as well. As described in Sec. 2.2, some theories involve a conformal breaking scale, hence a minimum energy is required to produce unparticles. Furthermore, the cross section is energy dependent. The partonic cross section of course decreases with increasing energy above the conformal breaking scale. But as high momentum fraction x in the parton density functions, see below, are required to produce unparticles with mass of the order 100 GeV, the production cross section increases with higher energies within a large energy range, even above the TeV scale, as higher x become more likely with higher center-of-mass energies.

So looking back, it is not surprising, that the weak gauge bosons have been discovered at UA1/2, a $p\bar{p}$ collider with 450 GeV center-of-mass energy, and later studied with unprecedented precision at LEP, an e^+e^- collider with up to 200 GeV center-of-mass energy.

Another milestone in particle physics, and of course of the SM itself, was the discovery of the top quark at the Tevatron in 1995. There, proton-antiproton collision took place at 1.8 TeV in Run I. The Large Hadron Collider (LHC) [40] is the next step taken by mankind to investigate further, what the basic ingredients of our world are.

The experimental environment is very clean and well-defined at electron colliders, since, as far as we know, leptons are point-like, elementary particles, hence without underlying substructure. This implies that the initial state is known and can be used as experimental input, which is not possible at a hadron collider, where the colliding partons p_1 and p_2 carry a momentum fraction x_1 and x_2, thus the effective center-of-mass energy is

$$\sqrt{s'} = \sqrt{sx_1x_2}. \tag{3.3}$$

The proton's remnants usually fly quasi-parallel to the beam and escape undetected, making it impossible to reconstruct the center-of-mass frame of the collision. A fraction of the remnants can as well traverse the detector components, making it hard to pick out and identify particles coming from the interesting hard interaction.

So building electron colliders with higher and higher beam energies would be desirable, but there are limitations. A linear collider would have to be several tens of kilometers long to reach an unexplored energy range. In a ring collider synchroton radiation limits the maximum reachable energy, since the energy loss per revolution is proportional to $E^4/(m^4R)$ for a particle with energy E, mass m at a collider with radius R. Concepts colliding heavier copies of the electron, like the muon, have been studied [41], but technical challenges have not been overcome yet.

Increasing beam energies is one issue, another is to increase the rate with which collisions occur. The protons circulating in the LHC are bundled into a so-called bunch. The more protons per bunch , and the more bunches are filled in the LHC, the more collisions take place. Thus, the rate of a given process is higher as well. The number of events per second produced in LHC collisions is given by

$$\dot{N}_{evt} = \sigma_{tot} \cdot L. \tag{3.4}$$

L is the machine luminosity and σ_{tot} is the total, weighted sum of cross sections of all possible processes of particle i with particle j:

$$\sigma_{tot} = \sum_{i,j} \int dx_i \int dx_j \, f_i(x_i, Q^2) f_j(x_j, Q^2) \hat{\sigma}_{ij}(Q^2), \tag{3.5}$$

where $f_i(x_i, Q^2)$ ($f_j(x_j, Q^2)$) is the probability to find a parton i (j) with momentum fraction x_i (x_j) at an energy scale Q^2, called *Parton Density Function* and $\hat{\sigma}_{ij}(Q^2)$ is the partonic cross section. σ_{tot} is dominated by elastic proton-proton scattering. QCD multijet events have fairly high cross sections as well, whereas the cross sections of new physics effects are usually expected to be orders of magnitude smaller, which leads to the requirement to efficiently select interesting events, see section 3.2.5. Fig. 3.1 shows cross sections and event rates as a function of center-of-mass energy.

In principle, the luminosity depends only on beam parameters and can be expressed for Gaussian beam distribution as

$$L = \frac{N_b^2 n_b f_{rev} \gamma_r}{4\pi \varepsilon_n \beta^*} F, \tag{3.6}$$

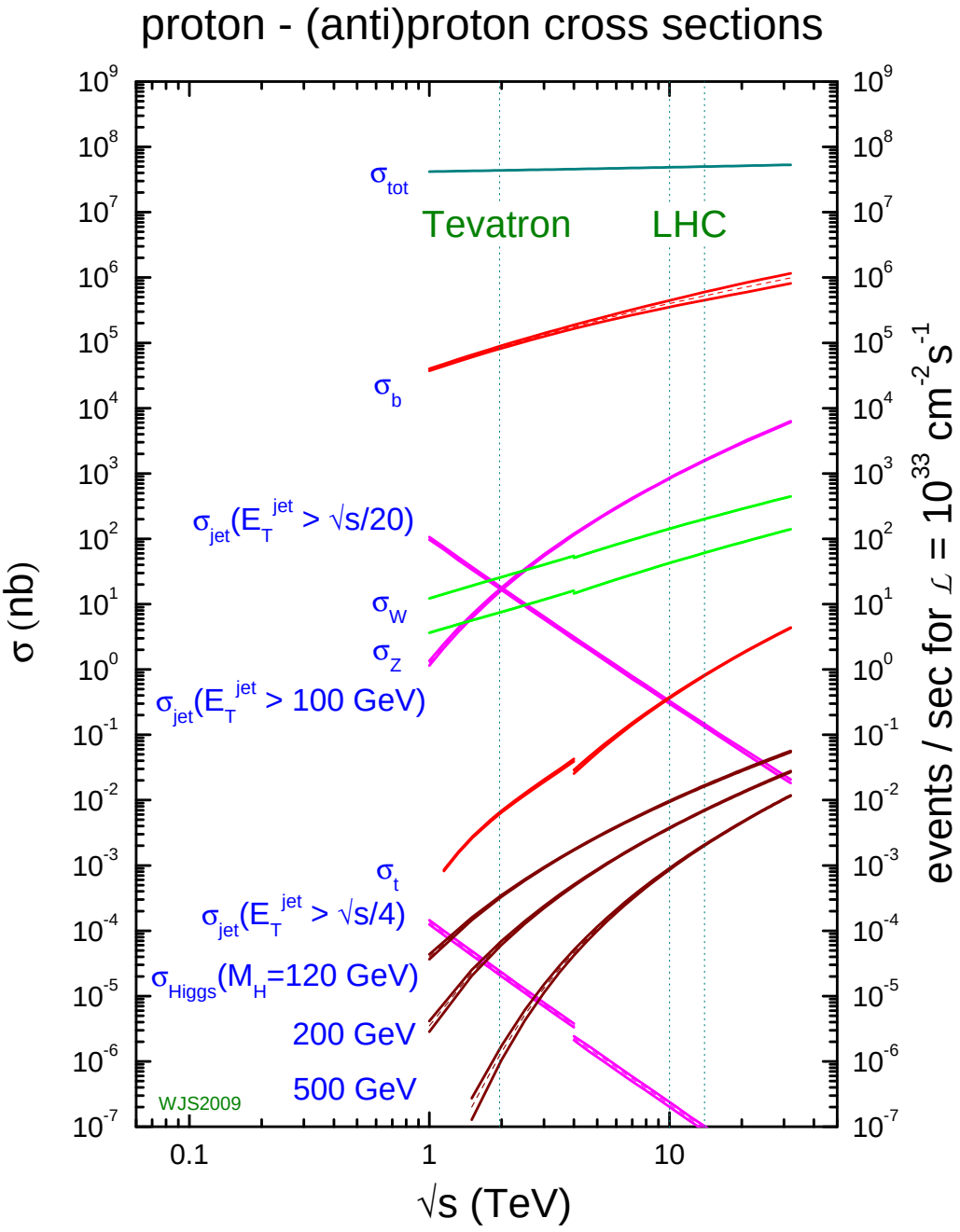

Figure 3.1: *Cross sections and event rates at hadron colliders as a function of the center-of-mass energy [42].*

where N_b is the number of protons per bunch, n_b is the numbers of bunches per beam, f_{rev} the revolution frequency with an upper limit fixed by the speed of light, γ_r the relativistic gamma factor, ε_n the normalized transverse beam emittance, β^* the beta function at the interaction point (IP) and F the geometric luminosity reduction factor due to the crossing angle at the IP

$$F = \left(1 + \left(\frac{\theta_c \sigma_z}{2\sigma^*}\right)^2\right)^{-1/2}, \tag{3.7}$$

where $\theta_c = 300\mu$rad is the full nominal crossing angle at the IP, σ_z the root mean square (RMS) of the bunch length and σ^* the RMS of the transverse beam size at the IP.

3.1.2 Design and Start-up Conditions

Making use of the former LEP tunnel, the LHC is situated at the French-Swiss boarder, west of Lac Leman, and is one of the largest machines ever built by mankind. The tunnel has a circumference of 27 km and lies between 45 and 170 m below the surface. The high energetic beams have to be kept on track. Using superconducting magnets is the method of choice to accomplish this. The LHC is capable of operating with proton beams or beams of heavy ions. At design conditions, it will run at a luminosity of $L = 10^{34}\,\mathrm{cm}^{-2}\,\mathrm{s}^{-1}$ for pp beams at a center-of-mass energy of 14 TeV, supplying the high luminosity experiments CMS[1], see section 3.2, and ATLAS[2] [43] with collisions every 25 ns. Low luminosity runs at $L = 10^{29}\,\mathrm{cm}^{-2}\,\mathrm{s}^{-1}$ and $L = 10^{32}\,\mathrm{cm}^{-2}\,\mathrm{s}^{-1}$ provide data for the elastic scattering experiment TOTEM[3] [44] and the b-physics experiment LHCb[4] [45], respectively. While operating with lead ions at 1150 TeV, the ALICE[5] [46] detector is a dedicated tool to investigate heavy ion physics at a peak luminosity of $L = 10^{27}\,\mathrm{cm}^{-2}\,\mathrm{s}^{-1}$.

In order to reach the design luminosity, 2808 proton bunches are filled in the LHC, separated by roughly 8 m, or 25 ns. The number of protons per bunch is limited by the non-linear beam-beam interaction that each proton experiences per bunch crossing. In combination with the constraints from the mechanical aperture, the nominal peak beam size is 1.2 mm, the maximum bunch intensity is thus $N_b = 1.15 \times 10^{11}$. The high beam intensity guarantees a sufficient rate of *hard interactions*, the source of possibly interesting processes, but these are accompanied by roughly 20 *soft interactions* per bunch crossing, called the *pile-up* events. Although it might be interesting to study these as well, cf. e.g. [47], they are considered background for most experiments and are to be distinguished from hard scattering processes.

1232 superconducting dipole magnets are used to keep the accelerated protons on track, as their trajectory is bent traversing a magnetic dipole field. The use of well established technologies, the superconducting cables are made of NbTi as utilized at Tevatron, DESY, and RHIC, were chosen for cost reduction and reliability. The operating temperature of 1.9 K is achieved by superfluid helium cooling. Using these state-of-the-art technologies, a maximum magnetic field strength of 8.4 Tesla is obtained, providing the possibility of

[1] **C**ompact **M**uon **S**olenoid
[2] **A** **T**oroidal **L**HC **A**pparatus
[3] **TOT**al and **E**lastic **M**easurements
[4] The **L**arge **H**adron **C**ollider **b**eauty Experiment
[5] **A** **L**arge **I**on **C**ollider **E**xperiment

operating with 7 TeV beams. For the dipoles, the "twin-core" design was chosen, i.e., two beam pipes with own coils share a common cold mass and cryostat, with the magnetic flux circulating in the opposite sense through the two channels. Only close to the four IPs, the beams share one pipe.

The proton bunches fed into the LHC have passed through multiple acceleration cycles, as the LHC cannot handle too low energetic protons. The injector chain Linac 2 - Proton Synchrotron Booster (PSB) - Proton Synchrotron (PS) - Super Proton Synchrotron (SPS) is depicted in Fig. 3.2.

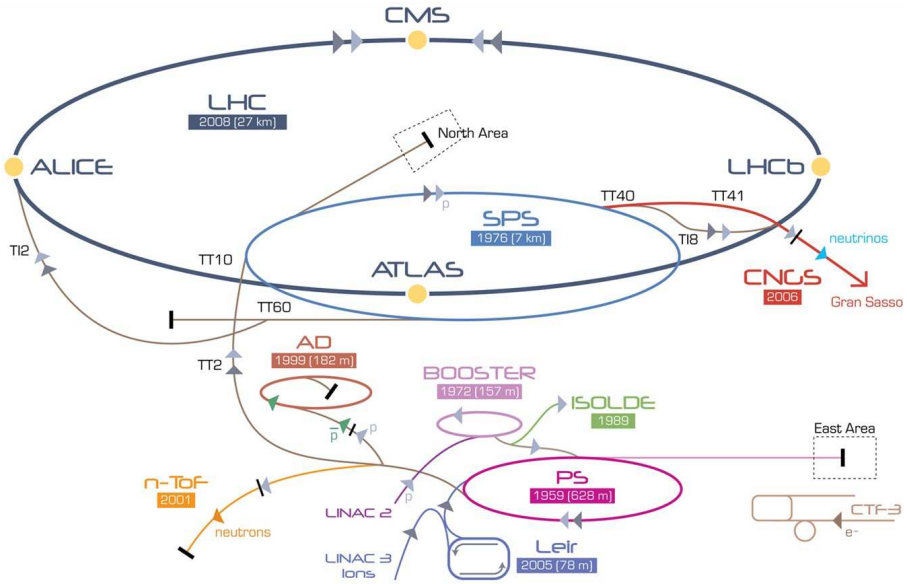

Figure 3.2: *The injector chain for LHC [48].*

First, hydrogen is ionized in a plasmatron and the resulting protons are accelerated with Linac 2 to 50 MeV. Three of the four identical PSB rings, each 1/4 of the PS circumference long, are filled each with one bunch from Linac 2. At this stage, the bunch has a length of 30 μs. They accelerate the protons to 1.4 GeV and squeeze the bunches to a length of 90 ns. Two batches, each containing three bunches, one from every PSB, are then filled into the PS, the second one 1.2 seconds after the first. There, the bunches are split up,

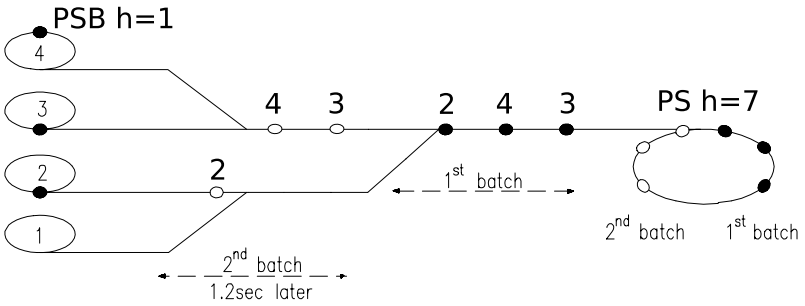

Figure 3.3: *The two batch filling scheme for LHC [40].*

accelerated to 25 GeV, and split up again, resulting in batches of 72 bunches with the desired 25 ns spacing. Again the bunches are compressed, now to 4 ns, and 4 PS cycles

are fed into the SPS, where a further acceleration to 450 GeV takes place. Finally, 24 SPS supercycles are injected into the LHC, where the protons obtain their final energy. Of course both LHC rings have to be filled. Then, the LHC is ready to produce collisions. The whole procedure is expected to take about one hour.

Mostly due to *pp* collisions itself, but as well due to beam-gas collisions, the beam intensity subsequently reduces . It is expected that data taking will last 6 to 12 hours per run. About 100 fb^{-1} are estimated to be collected per year at peak luminosity.

Detailed information about the LHC and its injector chain can be found in Ref. [49].

Start-up Conditions

The start-up conditions of the LHC in terms of beam energy, number of bunches, protons per bunch, etc. are well below the design conditions and change frequently. An incident on September 19, 2008, due to a faulty electrical connection between two of the accelerator's dipole magnets[6] led to a helium leak in sector 3-4. In the following, every connection was checked and some had to be replaced, which required a partial warm-up of the LHC. It has been decided that the LHC will run for the first part of the 2009-2010 run at 3.5 TeV per beam, with the energy rising later in the run. How much integrated luminosity will be collected at 7 TeV center-of-mass energy is yet to be seen. Former plans involved 10 TeV runs with approximately 100 pb^{-1} integrated luminosity. Background sample sizes have been adjusted to this expectation.

The foreseen LHC activity timeline is summarized in Tab. 3.1.

Month	Comment	Energy [TeV]	Max. number of bunches	Protons /Bunch	Integrated Luminosity
1	Beam commissioning				First collisions
2	Pilot physics	3.5	43	$3 \cdot 10^{10}$	100-200 nb^{-1}
3-5		3.5	43-156	$5\text{-}10 \cdot 10^{10}$	1-36 pb^{-1}
7-10		5.0	156-432	$7\text{-}9 \cdot 10^{10}$	26-110 pb^{-1}

Table 3.1: *LHC 2009 - 2010 expected luminosity performance [50].*

3.2 The Compact Muon Solenoid

The Compact Muon Solenoid [51] is a multi-purpose apparatus designed to measure precisely the products from *pp* collisions produced via the LHC. The detector lies approximately 88 m beneath the earth, nearby the French village Cessy. As described in the last section, the LHC will operate at design conditions of 7 TeV beam energy and $10^{34}\,\text{cm}^{-2}\,\text{s}^{-1}$ peak luminosity, requiring a bunch spacing of 25 ns. Every bunch crossing results in more than 20 *pp* interactions leading to more than 1000 charged particles traversing the detector, producing electric signals. This high particle flux – 10^9 particles per second – makes high demands on detector techniques and materials: the detector response has to be very fast in order to distinguish between different bunch crossings, it must be radiation hard to ensure

[6] http://press.web.cern.ch/press/PressReleases/Releases2008/PR14.08E.html

long endurance, and of course precise and reliable. The vast amount of data produced by the frequent reactions cannot and does not have to be saved completely. Only interesting events will be stored persistently. This common "needle in a haystack problem" is solved via multiple trigger levels that reduce the rate from 40 MHz to 100 events per second.

The main goals of the LHC is to discover the underlying mechanism that breaks electroweak symmetry and to answer questions left open by the SM. These answers could well be found in the TeV region. The detector requirements that have to be fulfilled in order to meet this goals, are shortly summed:

- Good muon identification, momentum resolution and charge identification over the widest possible p_{T} and η range, permitting a good dimuon mass resolution;
- Good charged-particle momentum resolution and reconstruction efficiency in the inner tracker accompanied by efficient τ and b-tagging;
- Good electromagnetic energy resolution resulting in good diphoton and dielectron mass resolution;
- Good missing transverse energy resolution, therefore premising a hermetic geometric coverage.

The coordinate system used in CMS has its origin at the nominal interaction point. The x-axis points to LHC's midpoint, the y-axis vertically upwards, and hence the z-axis is parallel to the beam direction in a right-handed coordinate system. (Missing) Energy or momentum transverse to the beam are thus derived using x and y components. Often cylindric coordinates are useful, with ϕ defined as the azimuthal angle measured in the $x-y$ plane and θ the polar angle measured from the z-axis. This choice originates from the assumed azimuthal symmetry of scattering processes. But θ is not a good quantity, since it is not Lorentz invariant. Instead, the pseudorapidity is defined as $\eta = -\ln\tan(\theta/2)$; a difference of pseudorapidities is Lorentz invariant. This is important, because a boost along the beam axis due to different Bjorken x values of the colliding partons cancels out and the difference in η is the same as in the center-of-mass frame.

At a lepton collider with equal beam energies, the center-of-mass frame of the colliding particles corresponds to the laboratory frame. For a hadron collider, this is not the case, since the momentum fraction $x_{1,2}$ of the two partons are likely two be unequal. However, averaged over many collisions, the activity in the detector will have azimuthal symmetry as well as a point-symmetry in z direction[7]. Therefore, a cylindrical layout is chosen for the CMS detector, with a bore in the middle supplying space for the beam pipe and onion-like arranged layers of detectors.

CMS is designed to precisely measure SM particles, which exist in large diversity. Photons from electromagnetic reactions require different detection techniques than hadrons from strong color interaction. Muons usually deposit little energy whilst traversing the detector and decay afterwards outside of the detector. Taus decay very rapidly and thus close to the IP. In addition, different quantities are ought to be measured, e.g. energy and transverse momentum. Obviously, diverse detector components are needed to overcome this challenge. The installed components are:

[7] aside from contributions due to forward-backward asymmetry

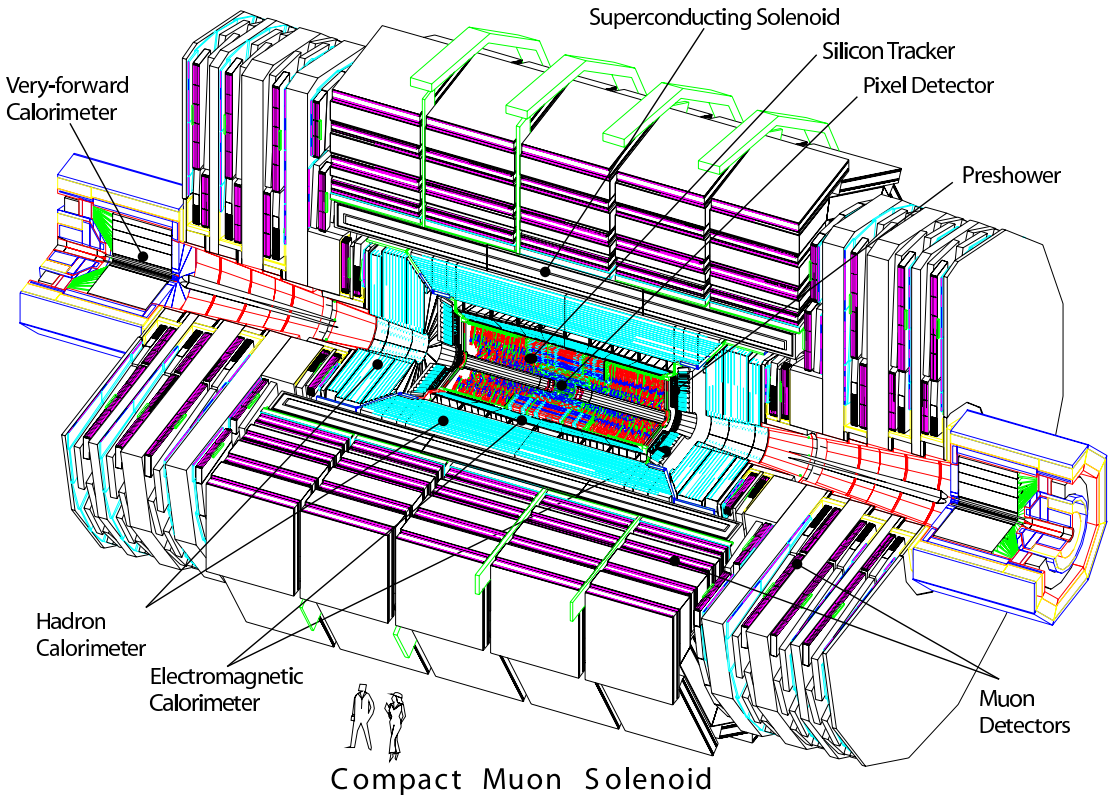

Figure 3.4: *A perspective view of the CMS detector [52].*

- the silicon inner tracker with pixel and strip detectors,
- the electromagnetic calorimeter made of lead tungstate ($PBW0_4$) crystals,
- the hadronic calorimeter, a brass/scintillator sampling calorimeter,
- the 3.8 T superconducting solenoid providing large bending power in order to measure momentum transverse to the beam,
- the muon system that uses three different techniques of gas detectors, namely Cathode Strip Chambers (CSC), Drift tubes (DT) and Resistive Plate Chambers (RPC)

Great care was taken to minimize dead regions and dead material. In total, the CMS detector weighs 12500 tons, has a diameter of 15 m, and is 21 m long. The barrel is divided into five wheels, with the IP at the center of wheel 0. At each end an endcap is put in place.

The mode of operation of every component is described in the following sections. A detailed description can be found in the CMS detector paper [52], providing all facts and figures.

3.2.1 Solenoid

The magnet is a distinguishing factor of CMS and its geometry found its way into the name itself. In contrast to ATLAS, where a toroidal field geometry is used in the muon

system and a solenoidal one in the tracker, CMS makes use of a global, solenoidal one. Being 12.8 m long and with a diameter of 5.9 m, the four layers of superconducting NbTi coils provide a homogeneous, 3.8 T strong magnetic field inside of the coils. 2.6 GJ are stored in the fields during operation. The superconductor is cooled down to 4.5 K in order to provide fields of such strength. Three return yokes in the barrel region and three in each endcap guide the flux on the outside of the coils, with the muon system interleaved within the yokes. 10'000 out of the CMS' total 12'500 tons are due to these yokes.

This concept has pros and cons. On the one hand, it provides a very strong and homogeneous field in the inside of the magnet's volume, making very precise measurements of charged particle's trajectory possible. The z-position of a vertex is not affected, as the field is parallel to the beam axis providing the possibility of a vertex fit. On the other hand, the coil sets a spatial limitation on detector components put in the inside. The remaining fraction of energy carried by charged particles that are not stopped in the calorimeter is unknown. That is mostly a problem at small η, where material budget is smallest. Moreover, a strong magnetic field is needed outside the coil to provide sufficient bending of muon trajectories. Therefore, the yoke is put in place with the interleaved muon stations. The iron yoke itself is quite dense, which leads to multiple scattering of muons therein. A further drawback, the fields in the endcaps are very inhomogeneous and a possible deterioration of measurements in the muon endcaps have to be taken into account/have to be accepted.

All details are to be found in [53].

3.2.2 Inner Tracker

Closest to the beam pipe the inner tracker (see Fig. 3.5) is mounted, designed to measure the trajectories of charged particles as precise and as efficient as possible. It has a length of 5.8 m and a diameter of 2.5 m and consists of two different sub-detectors: the silicon pixel detector and subsequently the silicon strip detector. Approximately 1000 charged particles are expected to traverse the inner tracker every 25 ns, making the need of a radiation hard technology unavoidable. Furthermore, a high spatial resolution and a fast response are basic requirements to be fulfilled, making precise vertex position measurements and bunch crossing identification possible. Armed with these characteristics the chance of identifying, and thus rejecting, minimum bias events is higher. Additional secondary vertices of the hard interaction produced by hadrons with c- or b-quark content or by taus that travel a few millimeters before they decay, won't resist detection.

Making use of layers of pixels and layers of strips, both high precision and affordable costs are achieved. The doped silicon semiconductor technique works roughly as follows. A charged particle produces electron-hole pairs that travel to the upper/lower electrodes by way of moderate bias voltage. The analog pulse height is being read out and combined from adjacent pixels/strips, since charge-sharing among them increases spatial resolution.

With the B-field parallel to the the z-axis inside the tracker, the transverse momenta of charged particles can be determined by measuring their bending in the $r-\phi$-plane. A compromise had to be found between the high power density of on-detector electronics making high precision measurements possible, but in turn requiring cooling, and a minimum of material budget in order to limit multiple scattering, bremsstrahlung, photon conversion

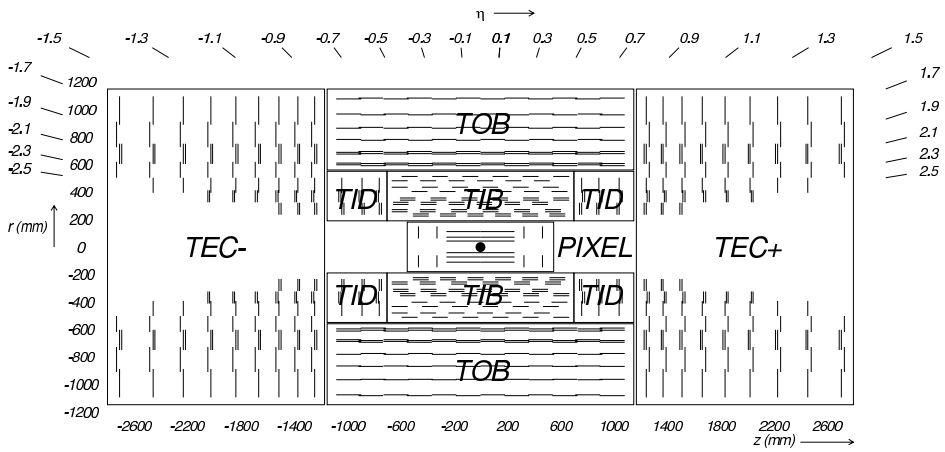

Figure 3.5: *Schematic cross section through the CMS tracker. Each line represents a detector module. Double lines indicate back-to-back modules which deliver stereo hits [52]. The components are the following: Tracker Inner Barrel (TIB), Tracker Outer Barrel (TOB), Tracker Inner Disk (TID), Tracker End Cap (TEC) and the pixel detector (PIXEL).*

and nuclear interaction. A cooling to $-10°$C is needed to abate radiation damage, as a lower temperature leads to less mobility of the defects in the semiconductor. This avoids the clustering of defects that would worsen the conductivity.

A detailed description of the inner tracker can be found in [54]. The following two subsections give a rough overview about the most important facts.

Silicon pixel detector

At the heart of the tracker lies a three-layered, cylindrical silicon pixel detector with the layers located at 4.4, 7.3 and 10.2 cm distance from the IP. It is enclosed by two endcaps at $z = \pm 34.5$ and 46.5 cm. 1440 modules - their arrangement is shown in Fig. 3.6 - cover a pseudorapidity range of $|\eta| < 2.5$. Here, the seed for later track finding algorithms is set and usually at least two hits are found. The pixels have a size of 100x150 μm^2 and a resolution of 17 (10) μm in z (ϕ)-direction is achieved using information from charge-sharing. The analog signal is converted to light and transmitted to the readout electronics via optical fibers to reduce the material budget.

Silicon strip detector

Adding more layers of pixel detectors would have been too costly, thus silicon strip detectors are the method of choice to gain more hits for track finding algorithms but keeping costs low. Moreover, the occupancy, i.e. the particle flux per cell, decreases with increasing radius. Between $r = 20$ and $r = 116$ cm 10 of such layers have been put in place, four in the Tracker Inner Barrel (TIB) and six in the Tracker Outer Barrel (TOB), accompanied by three discs in the Tracker Inner Disc (TID) and nine discs in the Tracker End Cap (TEC). The strip pitch sizes usually 80-120 μm. 15‘158 modules with 24‘244 sensors cover about 9.3 million strips, an active area of 198 m^2. Again, a pseudorapidity of $|\eta| < 2.5$ is covered. Some modules are mounted with two slightly skewed sensors, making resolution in

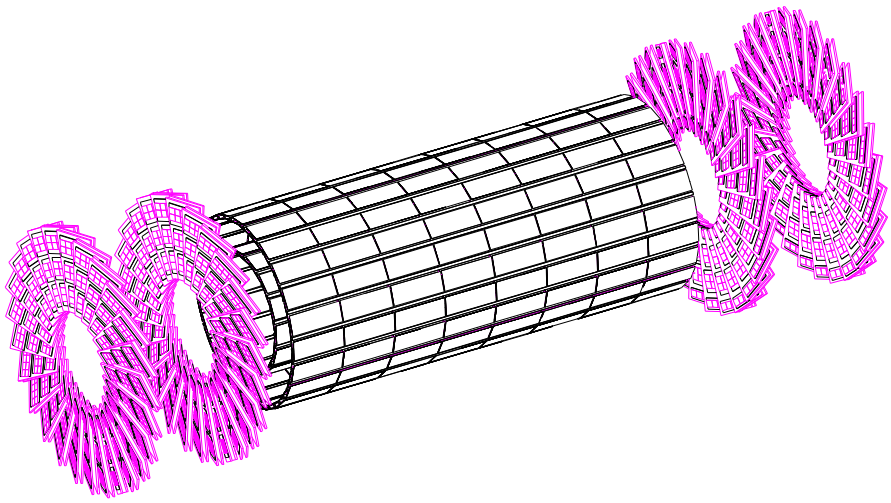

Figure 3.6: *Perspective view of the CMS pixel system [54].*

space possible, whereas one strip measures hits only along one dimension. The innermost strip modules achieve a spatial resolution of 15 μm at a strip pitch of 61 μm.

Combining 66 million pixels and 9.3 million strips allows a transverse momentum resolution of

$$\frac{\Delta p_{\mathrm{T}}}{p_{\mathrm{T}}} = 0.15 p_{\mathrm{T}}[\,\mathrm{TeV}] \oplus 0.5\%, \tag{3.8}$$

proper alignment provided.

3.2.3 Calorimeter

As stressed several times in the last chapter, the inner tracker measures the transverse momentum of charged particles, whereas neutral particles do not produce hits there at all. On that account, the subsequent detector is designed to quantify the particle's energy, for both charged and uncharged particles.

The energy is measured by collecting the light that is produced during the deceleration process. The measured amount of light does not correspond to the particle's energy in case of leakage. For MIPs[8] like muons or hardly interacting particles like neutrinos, this procedure is not possible at all, since their interaction length is too long. Electrons and photons are absorbed readily, hadrons travel further before being stopped, and muons with a p_{T} larger than about 10 GeV will not be stopped in the detector at all as they interact much less on their way through the detector. Anyway, the former two are best stopped by heavy elements, providing a large number of hull electrons and large nuclei, thus giving electrons and photons the possibility to scatter and hadrons to interact strongly again with those nuclei. Consequently, a two-stepped design has been followed, arranging firstly a layer of active material to stop light electromagnetic particles, the electromagnetic calorimeter (ECAL), and secondly a thick layer to stop hadrons, the hadronic calorimeter (HCAL). Of course it is advantageous to allow for the finest possible granularity in η and ϕ ensuring a good angular resolution and to have a good energy resolution. A compromise between costs and quality had to be found.

[8] **M**inimal **I**onizing **P**articles

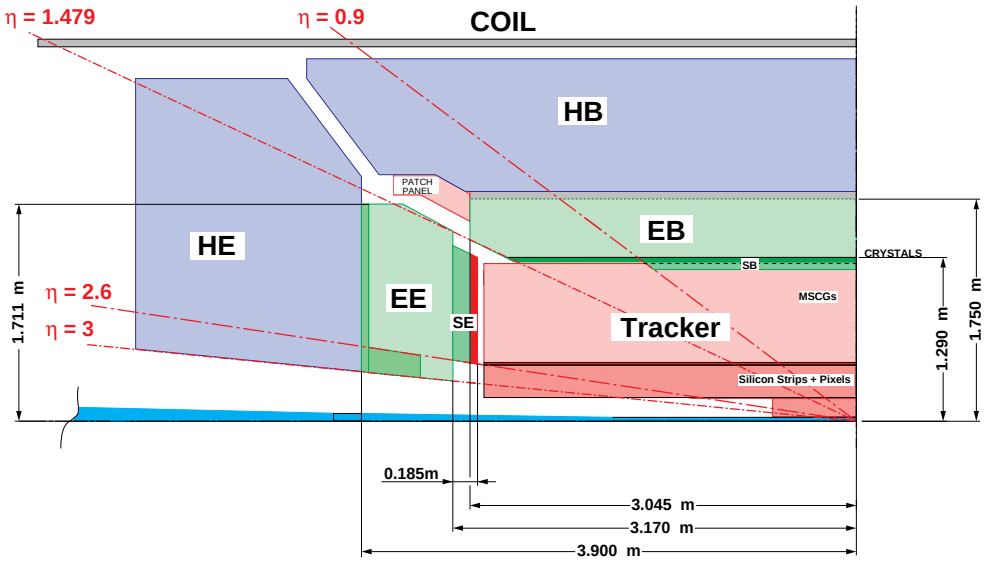

Figure 3.7: *Schematic view of one quadrant of the tracker and calorimeter of CMS [55].*

A schematic, longitudinal view of the calorimeters is depicted in Fig. 3.7. More information is available in [55, 56].

Electromagnetic Calorimeter

The basic properties of the electromagnetic calorimeter are:

- It consists of 61200 inorganic, homogeneous crystals made of lead tungstate ($PbWO_4$) and is read out by avalanche photodiodes (APD) in the barrel region (EB) and 7324 crystals read out by vacuum phototriodes (VPT) in each endcap (EE). They are arranged mechanically as can be seen from Fig. 3.8. The crystals in the EB have a cross section of 22x22 mm^2 at the front face and 26x26 m^2 at the rear face. They provide about 25 interaction lengths ensuring almost no leakage. The front face of the EB crystals are at a radius of 129 cm, whereas the EE crystals are placed 315.4 cm away from the nominal IP. Barrel (endcap) crystals have a total weight of 67.4 (24.0) tons.
- The EB (EE) covers a pseudorapidity range of $|\eta| < 1.479$ ($1.479 < |\eta| < 3.0$).
- One reason for choosing lead tungstate is that 80% of the produced light is emmitted within 25 ns. Hence, the deposited energy can be assigned to a certain bunch crossing. Approximately 4.5 photoelectrons per MeV are collected in both APDs and VPTs.
- Moreover, lead tungstate has a small Moliere radius[9] of 2.2 cm and a small readiation length of 0.89 cm providing a fine granularity and a compact ECAL.
- However, the light yield of $PbWO_4$ is temperature dependent, hence a temperature as stable as possible is needed.

[9] A cylinder with radius of twice the Moliere radius $r = 2R_M$ contains on average 95% of the absorbed energy [57].

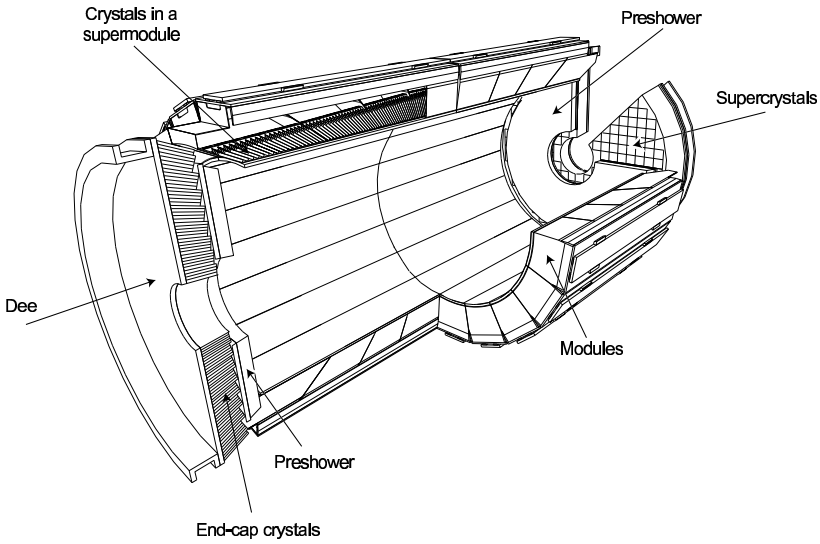

Figure 3.8: *Layout of the CMS electromagnetic calorimeter showing the arrangement of crystal modules, supermodules and endcaps, with the preshower in front [52].*

- Radiation damage decreases with lower temperatures, recovery through thermal effects increase with rising temperature, an optimal balance is found at 18°C demanding a thermal screen between tracker and ECAL.

No measurement is perfect, neither is the energy measurement of the ECAL. Main sources of uncertainties are the intrinsic electronic noise of the used electronics and noise produced by pile-up, the probabilistic nature of photon collection and absorption and calibration errors. Using calibration measurements carried out before final assembly, the expected resolution of the ECAL is [52]:

$$\left(\frac{\sigma}{E}\right)^2 = \left(\frac{2.8\%}{\sqrt{E/\,\mathrm{GeV}}}\right)^2 + \left(\frac{0.12}{E/\,\mathrm{GeV}}\right)^2 + (0.30\%)^2\,. \tag{3.9}$$

Hadronic Calorimeter

Outside of the ECAL, the hadronic calorimeter follows. It consists of four main parts: The Hadron Barrel (HB), the Hadron Endcap (HE), the Hadron Outer (HO) and the Hadron very forward (HF) calorimeter, covering a pseudorapidity of $|\eta| < 1.3$, $1.3 < |\eta| < 3.0$, $|\eta| < 1.3$ and $3.0 < |\eta| < 5.2$, respectively. It is designed to quantify the hadronic activity of the events and is important for $\not{E}_{\mathrm{T}}$ measurements. In contrast to the ECAL, the HCAL is a sampling calorimeter. The large hadronic interaction length and the spatial constraints necessitate the usage of a sandwich design, using absorber material to force showering of the hadrons and active material to detect the showers.

The HB is placed between the outer extent of the EB (at $r = 177$ cm) and the inner extent of the magnet's coil (at $r = 295$ cm). As seen from the inside out, first comes a 9 mm thick active scintillator layer[10], followed by a 40 mm thick steel front plate. Then 15 layers

[10] made of Bicron BC408

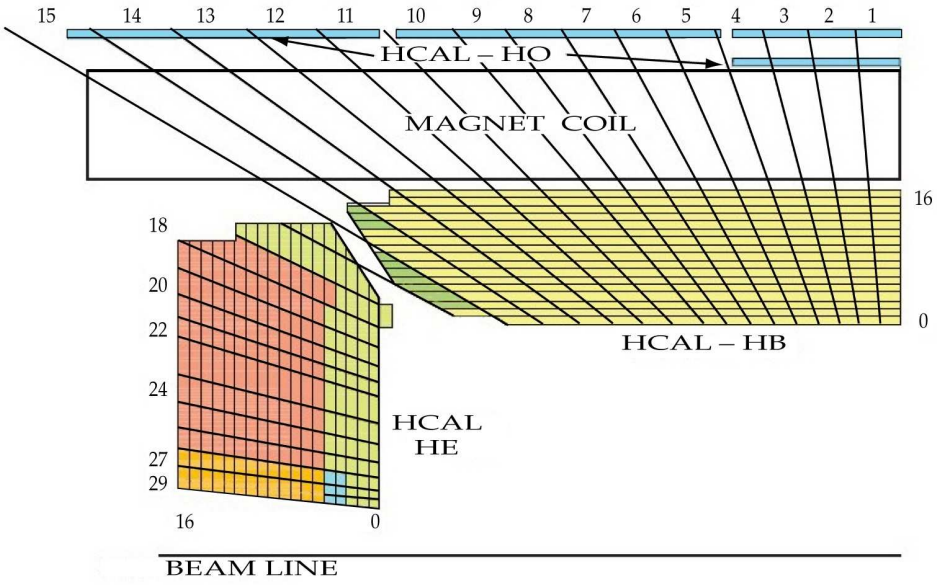

Figure 3.9: *The HCAL tower segmentation in the $r-z$-plane for one-fourth of the HB, HO, and HE detectors. The shading represents the optical grouping of scintillator layers into different longitudinal readouts [56].*

of 3.7 mm thick scintillator [11] take turns with 14 layers of approximately 50 mm thick brass layers and the last absorber before the coil is a 75 mm thick steel plate. Finally an active layer of 9 mm thickness finishes the HB. They are being read-out using wavelength-shifting fibers. Subdivided into 16 sectors along η and 72 sectors along ϕ, the achieved segmentation is $(\Delta\phi, \Delta\eta) = (0.087, 0.087)$. The multiple layers suggest a segmented readout along the longitudinal coordinate. However, this has not been implemented, but is subject to upgrades.

At $\eta = 0$, only about five interaction lengths are provided by the HB. Thus, the HO is placed after the coil, using the coil itself as absorber. Its arrangement is shown in blue in Fig. 3.9. Hadronic jets with delayed showering or very energetic jets are thus caught after the coil in the HO. A minimum of 11.8 interaction lengths is achieved, with contributions from ECAL, HCAL, the coil, support structure and the first layer of the iron return yoke.

In the HE a similar scheme is used. Again from the inside out, starting at $z = \pm 11.2$ m from the IP, a 9 mm thick scintillator layer - for the first layer Bicron BC408 is chosen - is put in front of the 17 sandwiched layers of brass, 79 mm, and scintillator material - Kuraray SCSN81 - of 3.7 mm thickness. The granularity decreases from $(\Delta\phi, \Delta\eta) = (0.087, 0.087)$ for $|\eta| < 1.6$ to $(\Delta\phi, \Delta\eta) = (0.17, 0.17)$ for $|\eta| > 1.6$. EE and HE sum up to about 10 interaction lengths.

The longitudinal read-out segmentation for the HB, the HO and the HE is visualized in Fig. 3.9. The resolution obtained with these detectors can be parametrized by [56]:

$$\left(\frac{\sigma}{E}\right)^2 = \left(\frac{120\%}{\sqrt{E/\,\mathrm{GeV}}}\right)^2 + (6.9\%)^2 \tag{3.10}$$

[11] made of Kuraray SCSN81

The forward calorimeter will be exposed to unprecedented particle fluxes. To give an idea of the quantities, approximately 100 GeV is deposited in the detectors with $|\eta| < 3.0$ and 760 GeV in the HF for every pp collision. Thus, very radiation hard technology has to be used. The chosen design is quartz fibers with embedded steel absorbers. The material sums up to 10 interaction lengths. Mostly electromagnetic particles produce Cherenkov light traversing the steel and the light is collected in the fibers measuring the electromagnetic component of the showers.

3.2.4 Muon System

Besides the solenoid, another distinguishing feature is represented in the name "CMS". Special attention is drawn on detecting muons, as the muon is produced in important channels, e.g. $Z \to \mu\mu$, and the muon could be a sign of yet to be probed processes like the "golden" Higgs-channel $H \to ZZ \to 4\mu$, $Z' \to \mu\mu$, etc. Of course, there are electron channels for the above mentioned processes as well, but the muon is easier to detect, as the muon is a MIP and usually does not shower at all. It reaches the muon system (MS) fairly unaffected, but still ionizes atoms on its way.

Not quite surprisingly, CMS demands high standards in not only detecting muons, but as well precisely measuring their trajectories in a wide energy range. Thus, a large area with multiple layers has to be covered in order to assure various hits along the particle's trajectory and a full hermeticity. These standards are met using the combined power of the tracker and the MS, as multiple scattering in the return yokes dominates the resolution in the muon system for a muon p_{T} smaller than roughly 200 - 300 GeV and thus the tracker information is more precise for its determination. But this does not mean that the MS is obsolete, on the contrary. The read-out of the tracker is too slow to use it for triggering purposes. Moreover, as the particle flux close to the IP is high resulting in many hits with indistinguishable origin, the MS provides highly accurate trigger information that there was a muon and where, making it possible to interpolate back the muon's trajectory to the tracker. Thus, hits in the tracker can be assigned to a particular muon, and these hits are then used for the actual reconstruction algorithm, see details in 3.3.1. For higher momenta, the MS resolution gets more and more important for the overall p_{T} resolution, cf. Fig. 3.10, as the trajectory is more straight and using the long lever arm is more beneficial.

Again, there is a individual design for barrel and endcaps, a cylindrical layout in the barrel and discs in the endcaps, as requirements differ. Three gas detector techniques come into operation in the MS. Their mode of operation is similar, but the distinguishing differences make them appropriate for each scope of duties. Basically, a muon ionizes gas while traversing the muon system, a high voltage disperses the charges, and an avalanche of electrons induces (influences) mirror charges on the cathode, which are amplified and measured.

A combination of Drift Tube chambers (DT) and Resistive Plate Chambers (RPC) are used in the barrel, as the magnetic field is still quite homogeneous and mostly present in the iron yokes, and the particle flux is low, making the use of DT possible. The DTs provide precise spatial measurements and the RPCs precise timing information, but as well spatial information is extracted from the RPCs and chronological information from the DTs, but with worse resolution. They cover both $|\eta|$ values smaller than 1.2.

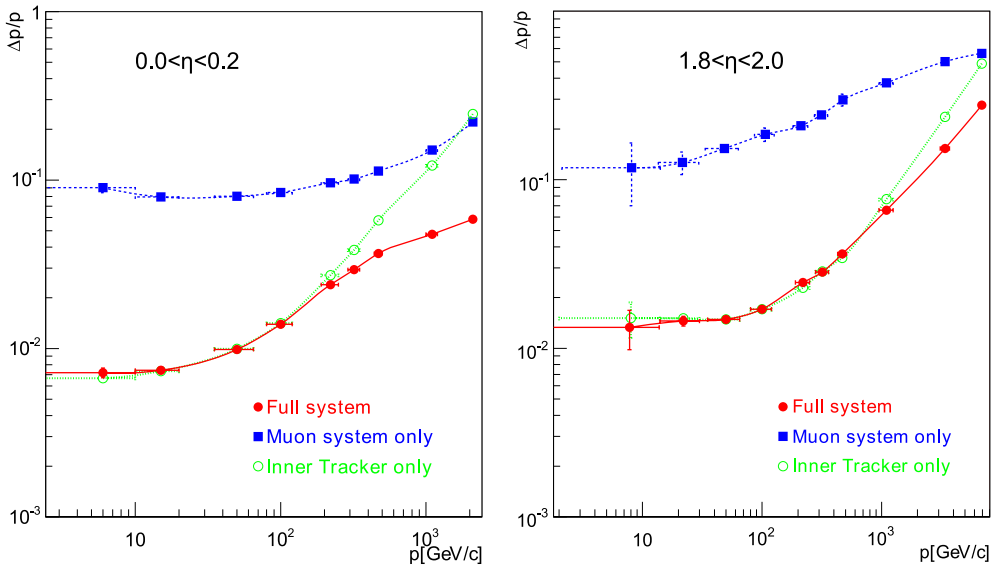

Figure 3.10: *The muon momentum resolution versus p using the muon system only, the inner tracker only, or both ("full system"). a) barrel, $|\eta| < 0.2$; b) endcap, $1.8 < |\eta| < 2.0$ [58].*

In the endcaps a combination of Cathode Strip Chambers (CSC) and, again, RPCs is chosen. A detector technology that is not effected by the deteriorated magnetic fields and that can reliably operate at high particle fluxes is needed. The CSCs provide this as drift distances are very short, of the order of few millimeters. They measure the position of the hits and the RPCs provide timing information. The CSCs cover a pseudorapidity of $0.9 < |\eta| < 2.4$, whereas the endcap RPCs cover $0.9 < |\eta| < 2.1$.

In total the MS covers an area of 25'000 m^2. Detailed explanation can be found in [59].

Drift tube chambers

The drift tube chambers are arranged as follows. The $r-\phi$-plane is divided into 12 sectors, each with four stations interleaved by the return yoke, as can be seen from Fig. 3.11. Thus, combining 12 stations for a given r approximates a concentric layer. Divided up into five wheels along the z-axis, the barrel MS consists of 12x4x5=240 chambers (MB). The inner three chambers contain three so-called superlayers (SL), of which the upper and the lower one measure the ϕ coordinate and the middle one the coordinate along z. The fourth MB is equipped with only two SLs, measuring only the ϕ coordinate.

Each SL is built of four layers of drift tube cells covering a surface of 11.5x42 mm^2. Every cell has a central anode wire, two cathode strips at the I-beams and additional field forming strips located at the top/bottom of each cell, illustrated in Fig. 3.12. The maximum drift length is 21 mm resulting in a maximum drift time of 380 ns for a gas mixture of 85% Ar + 15% CO_2, which corresponds to not more than 16 bunch crossings. At first, 16 bunch crossings seem to be too long to unambiguously pin point the hits to a single muon, but as the flux is low, there is only negligible occupancy. Each position of each hit is measured with an accuracy of 250 μm, using eight hits improves it to 100 μm along ϕ.

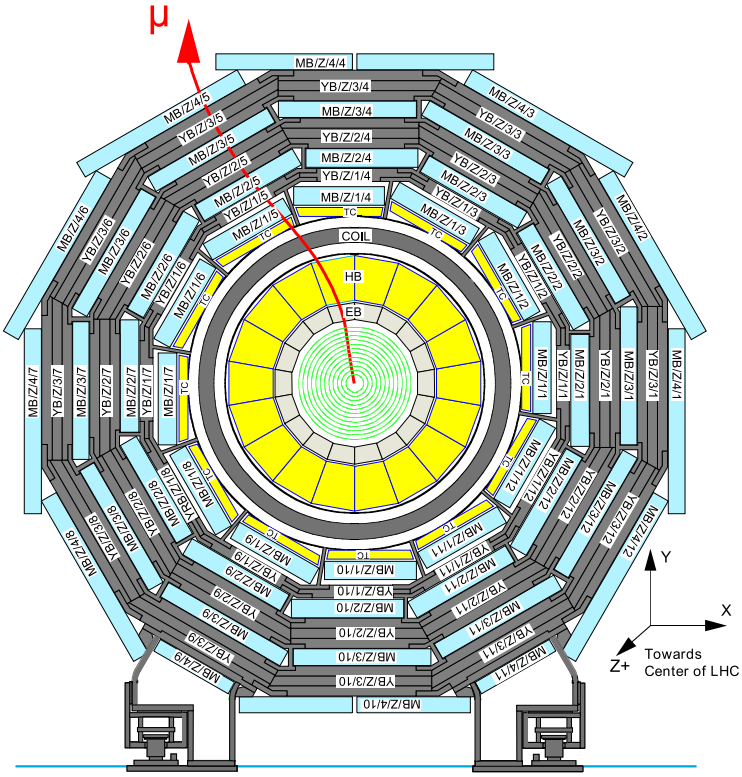

Figure 3.11: *Layout of the CMS barrel muon DT chambers in one of the 5 wheels [59].*

Cathode strip chambers

Due to the high flux and the non-uniform fields in the endcaps, the DTs are not suitable in this part of the detector. Instead, Cathode Strip Chambers are used, arranged in four stations perpendicular to the beam axis on each end. Each station, arranged as a disc, consists of two rings, the inner one is equipped with eighteen 20°chambers and the outer one with thirty-six 10°chambers, giving full ϕ coverage.

A single chamber is made of seven trapezoidal panels forming six gas gaps. Within every gas gap, a plane of 1000 wires with 3.2 mm distance is arranged as depicted in Fig. 3.13, forming a multiwire proportional chamber. The cathode panels are divided into strips along the radial coordinate, providing a resolution of about 150 μm in ϕ, whereas the anode wires provide resolution along r of a few millimeters, because about eight wires are combined for the read-out.

Resistive Plate Chambers

The Resistive Plate Chambers are able to provide very precise timing information (< 4 ns) such that even under LHC design conditions an unambiguous bunch crossing identification is possible. The resolution is about a few nanoseconds.

The layout of a double gap RPC, used in CMS, is depicted in Fig. 3.14. It is made of two pairs of bakelite plates confining two gas volumes, called gaps. These gaps are filled with a mixture of 96% Tetrafluoroethane ($C_2H_2F_4$), 3.5% iC_4H_10 and 0.5% SF_4. The highly resistive plates are coated with graphite electrodes in order to apply the high voltage of

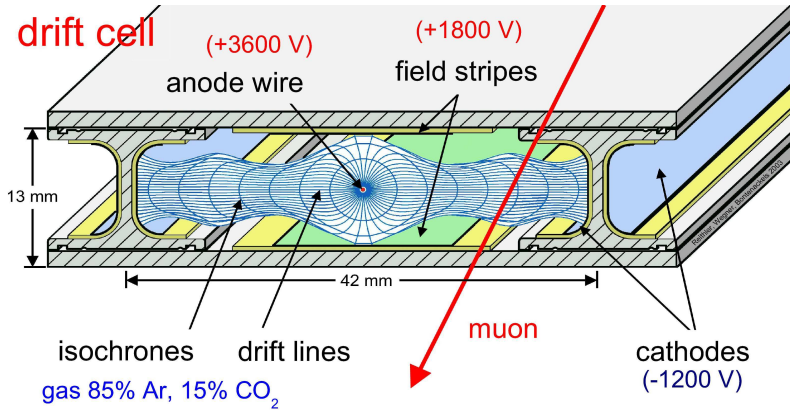

Figure 3.12: *Cross section of a CMS drift cell with drift lines of electrons and isochrones [42].*

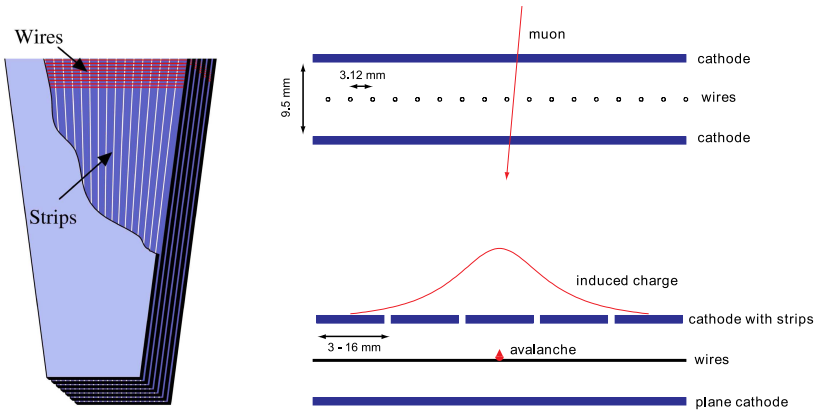

Figure 3.13: ***Left:*** *Layout of a CSC made of seven trapezoidal panels. The cut-out in the top panel reveals anode wires and cathode strips. Only a few wires are shown to indicate their azimuthal direction.* ***Right:*** *A schematic view of a single gap illustrating the principle of CSC operation [59].*

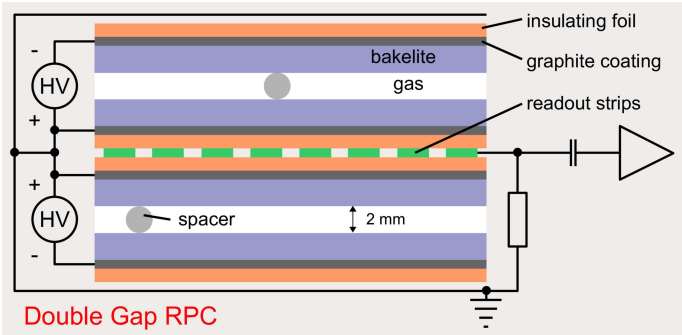

Figure 3.14: *Cross section of a double gap resistive plate chamber [58].*

approximately 10 kV. They cover an area of about $2x2$ m^2. The read-out strips in general allow for a better spatial resolutions, but only two read-out channels are available per RPC such that the spatial resolution of an RPC is about half its size.

The first two barrel muon stations are each sandwiched between two RPCs, the last two come with one RPC each. Hence, even muons with lower p_{T} that will be stopped in the middle of the MS will produce four hits in the RPCs. In the endcaps, there is only one RPC per muon station.

3.2.5 Trigger

The high design center-of-mass energy may open up new production channels, the high design luminosity increases statistics, having collisions at a rate of 40 MHz. But not all electronic channels of CMS can be stored persistently from every single bunch crossing. CMS has more then 10^8 channels, resulting in about 1 MB of data for each bunch crossing after zero-suppression. At a rate of 40 MHz, an amount of data of the order of 40 TB per second would have to be written to disk, if one was to store everything. This is both unnecessary and impossible, as most of the events are not of primary interest for most of the physicists and no storage system known today can handle that huge amount of data. Hence a careful selection has to be applied, done by the *online trigger system*.

The reduction is done in two consecutive steps called Level-1 (L1) trigger and High-Level-Trigger (HLT).

Level-1 Trigger

The L1 trigger is based on hardware pipeline processors with hardly any dead time, while the high-resolution data is held in pipelined memories in the front-end electronics. Every 25 ns, it provides a decision. To do so, it makes use of local, regional and global components. The Local Muon Trigger basically searches for clustered hits in the muon chamber and the Local Calorimeter Trigger for energy deposits in the calorimeter trigger towers. The Regional Triggers combine their information in a limited spatial region in order to form electron or muon candidates and rank them as a function of energy or momentum and quality. The four regional objects with the highest rank are all passed to the Global Muon Trigger and Global Calorimeter Trigger, which further select the four highest rank objects from the entire experiment and pass them to the Global Trigger, which finally takes the decision. In case the event gets accepted, the HLT takes over. Some L1 requirements (L1 seeds) are listed in Tab. 3.2; the entity of L1 triggers reduce the event rate to 30 kHz.

L1 seed	Threshold (GeV)
L1_SingleMu10	10
L1_DoubleMu3	3, 3

Table 3.2: *L1 trigger requirements.*

High-Level-Trigger

Being based on software, the HLT menu, that is, the requirements to pass HLT selection, can be changed during operation. The HLT makes use of the high-resolution data that were read out from the pipelined memory. Equipped with this information and a PC farm of approximately 1000 computers, it runs algorithms to determine type and multiplicity of particles in a certain event. This collection then runs through the possible *trigger paths* and a trigger fires, when the requirements are met. That provided, the event is written to tape. There are different paths with all kind of different collection of requirements – that can be one isolated muon (electron) above a certain p_{T} threshold, large missing transverse energy, many jets above a certain p_{T} threshold, etc. For every event the fired triggers are stored, such that later on the analyst can access this information and use it to select events. In this analysis, the triggers in Tab. 3.3 have been used, which implies the quoted cuts. The entirety of all trigger paths sum up to an event rate of about 100 Hz, resulting in 100 MB/s to be stored on tape.

A more elaborate explanation can be found in [60].

Trigger name	Trigger description	p_{T} threshold	required seed
HLT_IsoMu15	at least **one** isolated muon	15	L1_SingleMu10
HLT_Mu15	at least **one** muon	15	L1_SingleMu10
HLT_DoubleIsoMu3	at least **two** isolated muons	3, 3	L1_DoubleMu3
HLT_DoubleMu3	at least **two** muons	3, 3	L1_DoubleMu3

Table 3.3: *HLT triggers and their associated cuts.*

3.2.6 Luminosity Monitoring

Eq. 3.6 already implies that measuring the beam parameters provides a certain estimate of the luminosity. But the parameters cannot be measured to a high precision such that the error on the calculated luminosity will not be smaller than 10%.

Another way to determine the luminosity is adopted in the TOTEM experiment [44]. It is designed to determine the total cross section of LHC and the rate of inelastic and elastic processes. These quantities can in turn be used to fix the integrated luminosity:

$$N = N_{\mathrm{inel}} + N_{\mathrm{el}} = \sigma_{\mathrm{tot}} \cdot \int L\,dt = \sigma_{\mathrm{tot}} \cdot L_{\mathrm{int}} \tag{3.11}$$

To derive the total cross section from a rate measurement, one has to apply the optical theorem:

$$\sigma_{\mathrm{tot}} = \frac{4\pi}{p^*}\Im(F(0)), \tag{3.12}$$

where p^* is the momentum of the scattering particles in the rest frame. It relates σ_{tot} with the imaginary part of the forward scattering amplitude $F(0)$ by extrapolating the elastic cross section to zero momentum transfer:

$$\sigma_{\mathrm{tot}} = \frac{16\pi}{1+\rho^2}\frac{(dN_{\mathrm{el}}/dt)_{t=0}}{N_{\mathrm{inel}} + N_{\mathrm{el}}}, \tag{3.13}$$

where ρ is the ratio of the real to the imaginary part of the forward scattering amplitude.

The offline luminosity measurements are done making use of "standard candles". The Drell-Yan process provides this possibility as its production rate can be measured precisely and its cross section is high enough to have reasonable statistics in a short time, e.g. at design luminosity a rate of 30 Hz is expected for $Z \rightarrow l^+l^-$.

3.3 Reconstruction

Once data is written to tape, the offline reconstruction can take place. As it is not crucial to do the offline reconstruction on a time scale of few μs as in the HLT system, the whole detector information is used and all possibilities of particle trajectories are checked and compared to each other. The objects, that are used in this analysis, are muons, jets and missing transverse energy and their method of reconstruction is explained below.

3.3.1 Muon Reconstruction

The muon reconstruction algorithm starts in the innermost layer of muon chambers and works its way from the inside out. First, the innermost and outermost hits detected in CSC or DT are combined to *track segment candidates* and for each combination the number of hits that can be fitted to this particular candidate are counted. If a sufficient number of hits can be assigned to the candidate, it will be upgraded to a *track segment*. This track segment is then extrapolated to the next subdetector layer. This may include layers of RPCs as well, using the Kalman filter technique [61] that accounts for multiple scattering and other material effects. If suitable hits are found, these are combined with the track segment to form a new one and a new fit is done. In consecutive steps, all layers up to the outermost are included. Now, backward Kalman filter technique is used to work its way back to the innermost layer. The track parameters are defined performing a fit with all associated hits. Finally, the track is extrapolated back to the nominal IP and a vertex constrained fit is applied updating the track parameters. This defines the *standalone muon*.

Interpolating back the standalone muon to the inner tracker and taking into account material effects defines a region of interest (RoI) in the tracker, where the muon should have come from. Pairs of hits in the RoI are combined to form a seed for the muon trajectory candidate, where the two hits forming a seed must come from different layers. These layers must be pixel or stereo strip layers. Then again the Kalman filter technique is used to reconstruct tracks with the information of all layers. As the last step the tracker track segments are combined with standalone track segments to form global tracks and a final fit is done. The best fit defines a global muon. The reconstruction efficiency for a muon is about 95 to 99%. Among others, a muon track is defined by these parameters:

- χ^2/ndf: The χ^2 of the fitted track divided by the number of degrees of freedom. A usual value for a good muon is smaller than 10.
- Number of valid hits: The number of valid hits that are assigned to a muon track. An ordinary muon has few tens hits.
- d_0: The muon impact parameter in the $x-y$-plane w.r.t. the primary vertex, normally smaller than 0.2 cm.

After the reconstruction, further quantities defining the muon's quality are calculated. E.g. the *muon compatibility* [62] is a number that quantifies how MIP-like the muon behaved traversing the calorimeters. Therefore, characteristic signatures from MIPs along the muon's trajectory are identified in the ECAL and HCAL according to the energy loss stemming from a muon.

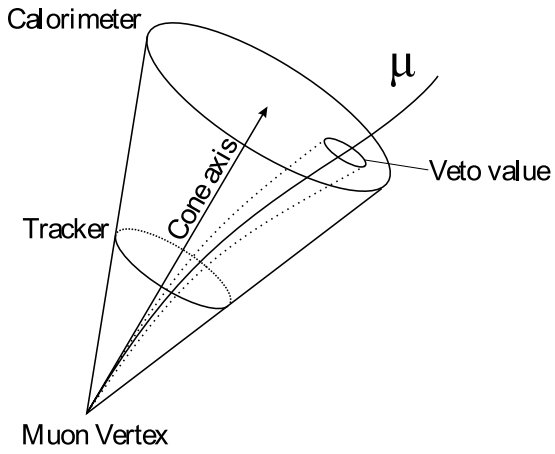

Figure 3.15: *The cone and the veto-cone for muon isolation.*

Another important feature, which is helpful to distinguish between prompt muons coming e.g. from W decays and non-prompt muons produced in b-jets, is the *muon isolation*. In a cone of $\Delta R = \sqrt{(\Delta\phi)^2 + (\Delta\eta)^2} < 0.3$ around the muon's trajectory, the p_{T} (E_{T}) of other tracks is summed up in the tracker (ECAL/HCAL) to determine the *track isolation* (*calorimeter isolation*). An inner cone of $R < 0.015$ is taken out in order to not count p_{T} (E_{T}) leaking from the muon itself, cf. Fig. 3.15.

Muon Energy Scale

Muons with a p_{T} above a certain value are not stopped in the detector and their energy is not known, but as stressed before, their track is used to determine the transverse momentum making use of the apparent bending [63]:

$$p_{\mathrm{T}}[\,\mathrm{GeV}] = \frac{B[\mathrm{T}]\rho[\mathrm{m}]}{3.3} \tag{3.14}$$

Thus, the momentum is linearly B-field dependent. The alignment of the muon system, of the tracker, and the alignment with respect to each other is important as well to get the bending right. The scale is known within one percent from CRAFT[12] data.

3.3.2 Jet and Missing Transverse Energy Reconstruction

The objects *jets* and *missing transverse energy* are both built from the same source, the *calotowers*. The former is a combination of calorimeter activity in clustered cells. For example gluons or quarks that are radiated from a hard scattering initial (final) parton, the so-called initial (final) state radiation (ISR/FSR), produce an accumulation of aligned

[12] **C**osmic **R**un **A**t **F**our **T**esla

hadrons. There have been and there are many attempts being made to distinguish between the different jet sources, but only b-jets have a promising probability of being identified. The second object built from calotowers, the missing transverse energy, is the total transverse imbalance of all calorimetric depositions.

A jet is an object that contains mostly pions, kaons and other hadrons. π^0 mesons can decay electromagnetically such that a jet has in general electromagnetic and hadronic contributions. The partonic source of a jet is a colored gluon or quark. The hadronization of a single quark or gluon to numerous hadrons happens due to the confinement in QCD, as empirically no objects charged under $SU(3)_C$ have been observed in asymptotic states. These hadrons fly approximately into the direction of the initial colored object. While traversing the detector, they mainly deposit their energy in the calorimeter. So it makes sense to form calotowers containing consecutive ECAL and HCAL cells. Approximately nine ECAL crystals cover one HCAL cell. Combined, they form the pseudo-projective calotower. Hence, a calotower represents the jet energy in a certain direction, defined in the $\eta - \phi$-plane. How this looks like is visualized in Fig. 3.16.

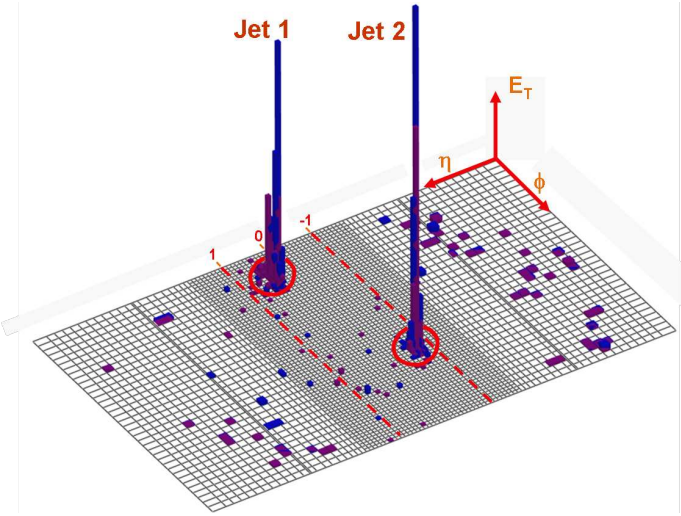

Figure 3.16: *The $\eta - \phi$-segmentation of the CMS hadron calorimeter [64].*

Jet Reconstruction

There are many algorithms to form jets out of calotowers. The one adopted in this thesis is the *Seedless Infrared-Safe Cone* jet algorithm (SISC) [65]. The key idea is to define circular enclosures (cones) in the $\eta - \phi$-plane, which are defined by their calotower content (points). All distinct cones, meaning having different point content, should be found by the algorithm and tested for stability. In order to find all distinct cones it is sufficient to test all circles, whose circumference lies on a *pair* of points. This is depicted in Fig. 3.17.

First, a *proto-jet* collection is formed: For each calotower i all other calotowers j are found that lie within a radius of $2R$ with R=0.5 in the $\eta - \phi$-plane. If no other calotowers are found, i is already a stable cone and promoted to a proto-jet. If j calotowers are found ($j \geq 1$), $2j$ circles in the $\eta - \phi$-plane can be drawn, with the i-th and the j-th calotowers on the edge of the circle. The factor 2 represents the number of possible circles defined by

two points ij. Each circle defines **four** possible cones, as there are **four** permutations with the initial "edge towers" included or excluded. Then every cone is checked for stability, i.e. if it is stable under addition/subtraction of edge towers. Unstable cones are omitted afterwards. After having considered all circles for all initial calotowers, the list of cones that have not been labeled as unstable are explicitly checked for stability, and if stable, are added to the list of proto-jets.

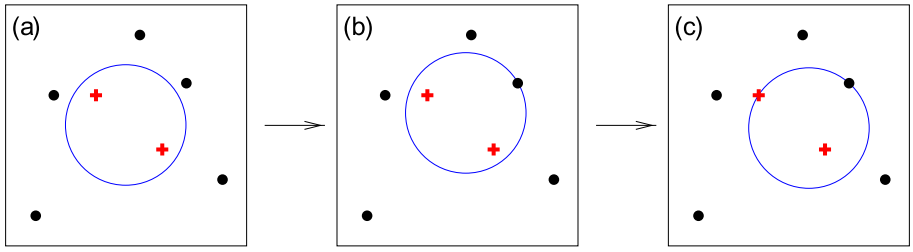

Figure 3.17: *The SISC jet algorithm: (a) Some initial circular enclosure; (b) moving the circle in a random direction until some enclosed or external point touches the edge of the circle; (c) pivoting the circle around the edge point until a second point touches the edge [65].*

These proto-jets can have very little p_{T}, thus the second step starts with removing all proto-jets with $p_{\mathrm{T}} < p_{\mathrm{T,min}}$. Then, ambiguities, i.e. overlaps between proto-jets, are resolved. The surviving objects are the final jets.

Jet Energy Scale

The HCAL is a sampling calorimeter. Thus, not the total jet energy is measured, as the jet deposits energy in the absorber material as well. The jet algorithm, even if infrared safe and collinear safe[13], tend to loose fractions of a jet. Both effects lower the jet energy. On the other hand, pile-up events that are produced along with the hard interaction will contribute to calorimetric activity, adding an a priori unknown amount of energy; an η dependence will complicate things. Summing up, the jet energy scale (JES) has to be corrected for certain influences, that is called jet energy scale corrections. A detailed description of such corrections can be found in Ref. [66].

$\not\!\!E_{\mathrm{T}}$ Reconstruction

In CMS, a nearly full 4π solid angle coverage is achieved, but a complete hermeticity can never be fulfilled, since at least two openings for the beam pipes are necessary. Hence, high energetic, low p_{T} particles escape detection, and therefore missing total energy is not a viable event characteristic. However, these undetected particles carry low *transverse* momentum and the imbalance of transverse energy in the calorimeter is indeed a useful quantity.

In the SM calorimetric *missing transverse energy* ($\not\!\!E_{\mathrm{T}}$) occurs in events with muons or neutrinos, indicating itself a process of interest. The muon p_{T} is reconstructed as described in Sec. 3.3.1 and the $\not\!\!E_{\mathrm{T}}$ is corrected for it, so *true* $\not\!\!E_{\mathrm{T}}$ is only produced in the SM by

[13] IR safe: adding low-energy calotower/ a soft particle does not change the set of stable cones; collinear safe: the splitting of one calotower/a particles momentum into two collinear ones does not change the set of stable cones

neutrinos, which have an interaction length of about one light year and hence do most likely not interact in the detector.

Beyond the SM, many theories predict weakly interacting particles that would add to the $\not{E}_{\mathrm{T}}$ distribution, like unparticle stuff. Hence it is very important to understand detector effects that would add to $\not{E}_{\mathrm{T}}$, e.g. dead cells, dead material, wrongly calibrated cells and so on, in order to not misidentify these effects as new physics.

Missing transverse energy [67] is built from calotowers being defined in a two-dimensional space $(\eta - \phi)$. Expressed in Cartesian coordinates, $\vec{\not{E}}_{\mathrm{T}}$ becomes:

$$\vec{\not{E}}_{\mathrm{T}} = \begin{pmatrix} \not{E}_{\mathrm{X}} \\ \not{E}_{\mathrm{Y}} \end{pmatrix} = \sum_n \begin{pmatrix} \sin\theta_n \cos\phi_n \\ \sin\theta_n \sin\phi_n \end{pmatrix} \tag{3.15}$$

where $\not{E}_{\mathrm{X}}$ and $\not{E}_{\mathrm{Y}}$ refer to the missing energy along x and y, respectively, of the CMS coordinate system. It's magnitude is referred to as $\not{E}_{\mathrm{T}}$. The scalar transverse energy (E_{T}) of an event is defined as the scalar sum:

$$E_{\mathrm{T}} = \sum_n E_n \sin\theta_n. \tag{3.16}$$

$\vec{\not{E}}_{\mathrm{T}}$ is corrected for various effects. As described above, jets undergo jet energy scale corrections, which of course have an impact on $\not{E}_{\mathrm{T}}$. This is called *Type I* corrections and can algebraically be written as:

$$\vec{\not{E}}_{\mathrm{T}}^{\,\text{Type I}} = \vec{\not{E}}_{\mathrm{T}} - \sum_{\mathrm{N_{jets}}} \left[\vec{p}_{\mathrm{T}_i}^{\,\mathrm{corr}} - \vec{p}_{\mathrm{T}_i}^{\,\mathrm{raw}}\right]. \tag{3.17}$$

Next step accounts for unclustered energy response and out-of-cone energy and are done on top of Type I corrections, according to the formula

$$\vec{\not{E}}_{\mathrm{T}}^{\,\text{Type II}} = \vec{\not{E}}_{\mathrm{T}}^{\,\text{Type I}} + c \times \sum_{\mathrm{N_{jets}}} \left[\vec{p}_{\mathrm{T}_j}^{\,\mathrm{IC7}} - \vec{p}_{\mathrm{T}_j}^{\,\mathrm{IC5}}\right], \tag{3.18}$$

where $\vec{p}_{\mathrm{T}_j}^{\,\mathrm{IC5}}$ and $\vec{p}_{\mathrm{T}_j}^{\,\mathrm{IC7}}$ are the transverse momenta of a reconstructed jet by iterative cone algorithm of cone sizes 0.5 and 0.7, respectively, and the sum runs over all jets above a certain threshold.

A further applied correction accounts for muons. The muons deposit little energy in the calorimeter as they are MIPs and their p_{T} is reconstructed using hits from the tracker and the muon system. After identifying those entries in the calorimeter left from muons, $\vec{\not{E}}_{\mathrm{T}}$ is reevaluated as:

$$\vec{\not{E}}'_{\mathrm{T}} = \vec{\not{E}}_{\mathrm{T}} + \sum_\mu \vec{E}^{\,\mu}_{\mathrm{T,calo}} - \sum_\mu \vec{p_{\mathrm{T}}}^{\,\mu}. \tag{3.19}$$

The resolution of $\not{E}_{\mathrm{T}}$ is in general sensitive to all kind of detector effects, as it is a global observable, and thus determining the various effects on its performance is challenging. The resolution is parametrized as:

$$\sigma(\not{E}_{\mathrm{T}}) = A \oplus B\sqrt{E_{\mathrm{T}} - D} \oplus C \cdot (E_{\mathrm{T}} - D), \tag{3.20}$$

where the A term accounts for effects due to electronic noise, pile-up and underlying events, B represents the probabilistic nature of energy deposits in the calorimeter, C accounts for

non-linearities, cracks and dead material and D is an offset correlated with A. Note that in rather "clean" events containing no or only one jet as well as muons $\sigma(\not{E}_{\mathrm{T}})$ is dominated by A and the resolution of the muon p_{T}, as $(E_{\mathrm{T}} - D)$ is small. In case wrong hits are assigned to a muon track during muon reconstruction, the fitted track can be very different from the true one and a wrong p_{T} is assigned to this muon. This bias is forwarded to $\not{E}_{\mathrm{T}}$. Hence, a good muon reconstruction algorithm is important to ensure a meaningful $\not{E}_{\mathrm{T}}$.

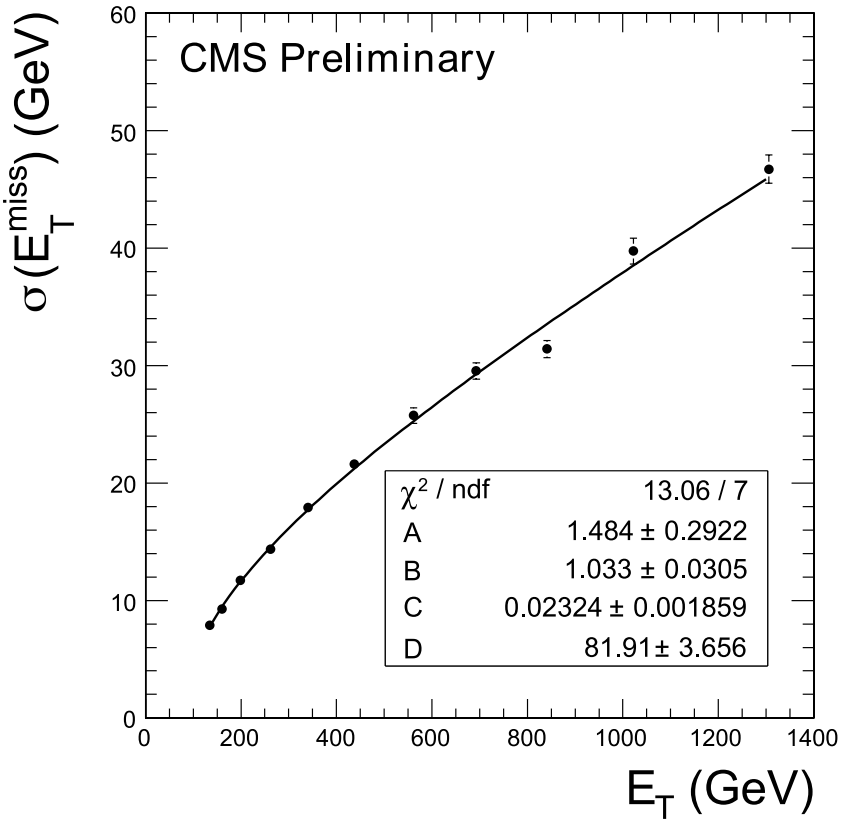

Figure 3.18: *$\sigma(\not{E}_{\mathrm{T}})$ vs. E_{T} for QCD dijet samples without pile-up for $20 < \hat{p}_{\mathrm{T}} < 800$ GeV (black dots) [68]. The resolution fit is shown by the black line. The fit parameters correspond to the terms in Eq. 3.20 with appropriate units.*

Chapter 4

Monte Carlo Simulation

Since this is a model dependent search, the signals of the new physics and of the SM backgrounds have to be known in detail. With the help of Monte Carlo (MC) generators, such events are generated in pp-collisions at a given center-of-mass energy, in this study 10 TeV. Afterwards the detector response is simulated.

4.1 Generation with Pythia

In order to do carry out a feasibility study with the aim of determining the signal significance, one needs event samples that contain the new searched for signal and of course samples containing the possible background events. The SM background samples are centrally produced and distributed. The CMS Data Bookkeeping System (DBS) [69] is a bookkeeping tool offering an easy way to locate the ready-to-use copies of samples from all over the world. Signal samples are only being produced centrally for a few signals; in case one searches a new exotic signal, the samples have to be produced individually.

Pythia8 [28] is a MC generator that generates particle interactions at tree level and is capable of simulating parton showers. Various parameters can be varied and tuned to match certain conditions, e.g. the center-of-mass energy can be set to the desired value and a special parametrization of the parton density function is ought to be chosen from various possibilities. Here CTEQ5L is used. Pythia8 provides the generation of a large variety of process and, more importantly for this study, offers the implementation of new processes.

An Unparticle plug-in by S. Ask [70] makes use of this possibility. After installing and configuring Pythia8, used in version 8.120 for the spin-1 case[1], the plug-in is added and configured such that Pythia puts out the generated events in the desired output format, HepMC::GenEvent in this case. This format stores 4-vectors of all produced particles in a list and the corresponding particle ID to distinguish between different kinds.

4.2 In and out of CMSSW

The production of samples at generator level was done outside of the CMS software framework (CMSSW) with standalone, custom-made Pythia. To make use of the powerful CMS

[1] and now available in version 8.125_private [71] for the spin-0 case

software framework the format has to be adapted to its specifications. IOMC [72] provides such an interface. Consequently, the output file is converted into a ROOT file, ready to pass through all the steps of CMSSW. First, the cmsDriver tool produces a collection of all specified generation steps, which can be GEN, SIM, and RECO. GEN collocates all generated particles in the GenParticleCollection and subsequently the simulation is performed. The particles are passed through the detector simulation, which simulates the detector response for every single trajectory, just the way a real collision would produce particles traversing the detectors producing hits and depositing energy. This is called FullSIM. There is as well the option to do fast simulation, FastSIM, which speeds up the simulation roughly by a factor of 10, but is less precise. Afterwards, further required steps are done, these are DIGI, L1, DIGI2RAW and HLT, where DIGI digitizes the simulated hits, L1 performs the L1 trigger selection, DIGI2RAW converts the digitized hits to the RAW format. The RAW format is equivalent to the data coming out of CMS with real collisions. HLT executes the High Level Trigger selection. The data format is called SIM and contains all hits and energy deposits.

Then, the reconstruction is performed; this and subsequent steps are identical for simulated and real data. The methods of reconstruction for the most interesting particles are described in Sec. 3.3. The data format after this step is called RECO and contains high level physics objects. This is not the end of the chain. The official doctrine encourages the user to reduce further the amount of data that is stored per event and thus to apply basic cuts on particle properties using the PhysicsAnalysisToolkit (PAT). In many use cases, the analysis is performed on this format, called PAT.

4.3 MUSiC

The MUSiC[2] group at Aachen [73] has developed a framework, which very much suits the analyst's needs. High-level physics objects are readily obtained making use of the PXL format, cuts can easily be applied and are steered via a single text file. Additionally, a "plot factory" provides histograms of all basic properties of electrons, muons, jets and more recently photons [74]. This holds for generator and reconstruction level. Cross cleaning, matching and trigger/reconstruction efficiency calculations are further valuable features. So the analyst can readily start his analysis without having to deal with CMSSW peculiarities.

The work flow of the whole production process is shown in the following picture, Fig. 4.1. Given are the names of the reconstruction step, the current framework and the data format with its approximated size per event. The PXL format used within the analysis is very small (3 KB/event) leading to a manageable amount of data and the possibility to re-do the analysis on short time scales.

4.4 Signal Monte Carlo

As described in Sec. 2.2 the unparticle parameter space is defined by three variables, the scaling dimension $d_{\mathcal{U}}$, the unparticle renormalization scale $\Lambda_{\mathcal{U}}$ and the coupling strength λ.

[2] **M**odel **U**nspecific **S**earch **i**n **C**MS

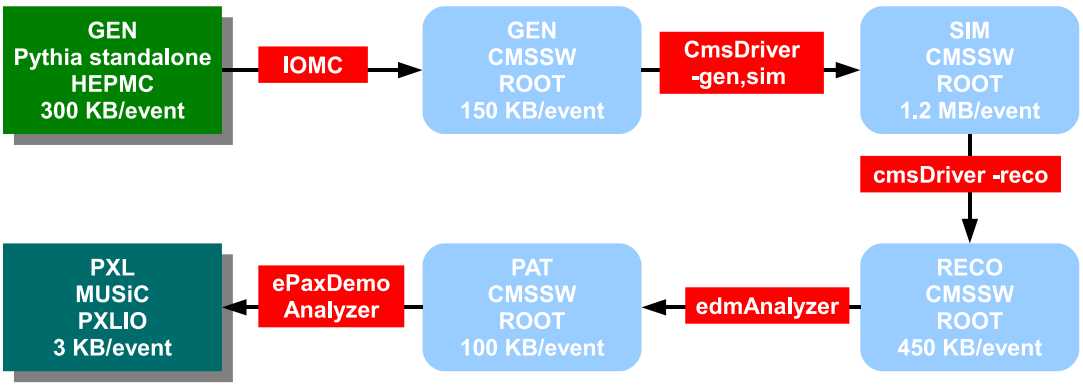

Figure 4.1: *The production flow of the produced samples is shown. They pass the simulation and the reconstruction, and are then skimmed twice via the PAT and finally via MUSiC.*

So in general, one has to produce signal samples in a three-dimensional grid in this space. To reduce the data volume and needed CPU power, the coupling was fixed to unity - it can be rescaled later - such that a two-dimensional dependency is left. At a grid with 90 parameter points[3] signal samples with approximately 10 K events have been produced for the channel $q\bar{q} \to \mathcal{U} + Z(\mu\mu)$. The matrix element for the process $f(p)\overline{f}(p') \to \mathcal{U}(P_\mathcal{U})Z(k)$ has been calculated in Ref. [26] and recently included in Pythia8 [70]. The characteristic final state topology is two opposite-sign (OS) muons and missing transverse energy.

Already at generator level, certain cuts have been applied, namely a $\hat{p}_T$-cut of 50 GeV and an $\hat{m}$-cut of 100 GeV. $\hat{p}_T$ ($\hat{m}$) is the transverse momentum (invariant mass) of the hard process. The $\hat{p}_T$-cut was applied in order to enhance statistics in the tails, since no search is done in low $\not{E}_\mathrm{T}$-bins anyway. A comparison of the unparticle p_T spectrum for $\hat{p}_T = 20, 50\,\mathrm{GeV}$ is shown in Fig. 4.2. As expected the samples agree above the $\hat{p}_T$-cut. The $\hat{m}$-cut on the other hand was mainly applied to speed up generation. Finally, the Z was forced to decay into a pair of muons, as well in order to enhance statistics.

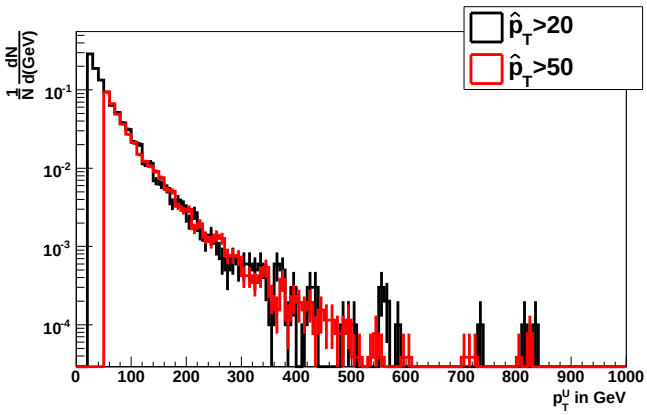

Figure 4.2: *The $\mathcal{U}$ p_T is drawn on generator level for different $\hat{p}_\mathrm{T}$ cut values normalized with respect to each other and the black histogram normalized to unity.*

[3] with $d_\mathcal{U} = 1.000001$, 1.01, 1.02, 1.03, 1.04, 1.05, 1.06, 1.07, 1.08, 1.09, 1.1, 1.2, 1.3, 1.4, 1.5 and $\Lambda_\mathcal{U} =$ 0.5, 1.0, 2.0, 5.0, 10.0 and 100.0 TeV

Basic properties have been inspected in order to cross-check the MC generator. In Fig. 4.3 (left) the p_{T} of the Z boson is plotted against the p_{T} of the unparticle at generator level for the space point $d_{\mathcal{U}} = 1.5, \Lambda_{\mathcal{U}} = 2$ TeV in the vector unparticle case. Most of the entries are along the bisectrix, meaning that their p_{T} is in balance, as expected from Fig. 2.3. On reconstruction level, there is no unparticle and no Z boson at hand, but only $\not{E}_{\mathrm{T}}$ and the two muons coming from the Z. Hence the p_{T} of the combined muons was plotted against $\not{E}_{\mathrm{T}}$. Again a good correlation was found, see Fig. 4.3 (right).

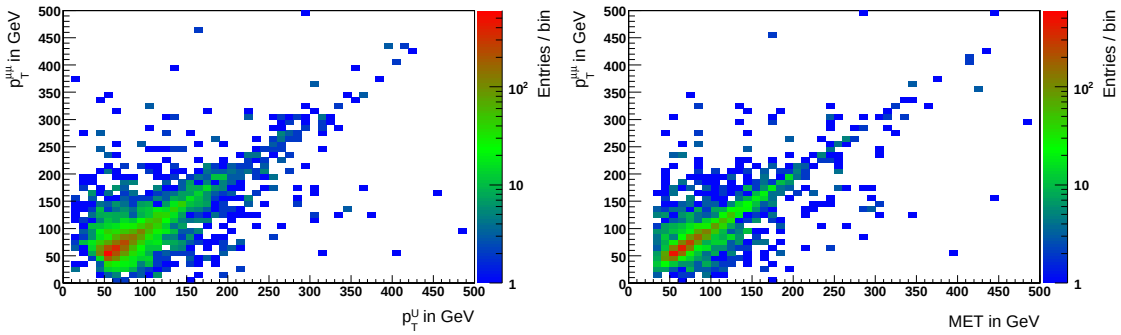

Figure 4.3: *Left: The Z p_{T} is drawn against the $\mathcal{U}$ p_{T} on generator level. Right: The Z p_{T} is drawn against the $\not{E}_{\mathrm{T}}$ on reconstruction level. The empty region on the left-hand side originates from a pre-selection cut of 30* GeV $\not{E}_{\mathrm{T}}$ *, see Sec. 5.1.*

One also has to check if the unparticle is the dominant source of $\not{E}_{\mathrm{T}}$ in the final state. Two quantities have been looked at. First, a histogram of the difference in ϕ between the $\not{E}_{\mathrm{T}}$ on reconstruction level and the unparticle on generator level is inspected, and followed by the difference in p_{T} of the two. Plots are to be found below, Fig. 4.4. The means are consistent with zero and have a reasonable width. Hence, the unparticle is the dominant source of $\not{E}_{\mathrm{T}}$ in the final state of the signal.

For a given process and a given amount of data, the signal sensitivity increases with increasing cross section. For the process under study, the cross section is parameter space point dependent, hence depends on $d_{\mathcal{U}}$ and $\Lambda_{\mathcal{U}}$. This is shown in Fig. 4.5 at leading order (LO) for the vector unparticle case. The cross section was calculated for the space points marked with a white circle. The quadratic[4] dependence on λ is omitted as it is set to unity. The cross section for a scenario with e.g. $\lambda = 0.9$ is obtained by multiplying with 0.81. A k-factor[5] for NLO QCD processes is not published in the literature for the processes under study. A value of 1.3 is used in this study as was done in Ref. [75], since it is expected to be similar [76].

4.5 Standard Model Background Monte Carlos

A SM event containing two OS muons and $\not{E}_{\mathrm{T}}$ is considered background to the signal, since it possesses the same topology. Isolated muons are only very rarely faked by other objects, as photons, electrons, and jets are usually stopped before they reach the muon system and

[4] Quadratic, because for real unparticle production there is only one unparticle vertex.
[5] A k-factor is the ratio between the NLO and the LO cross sections.

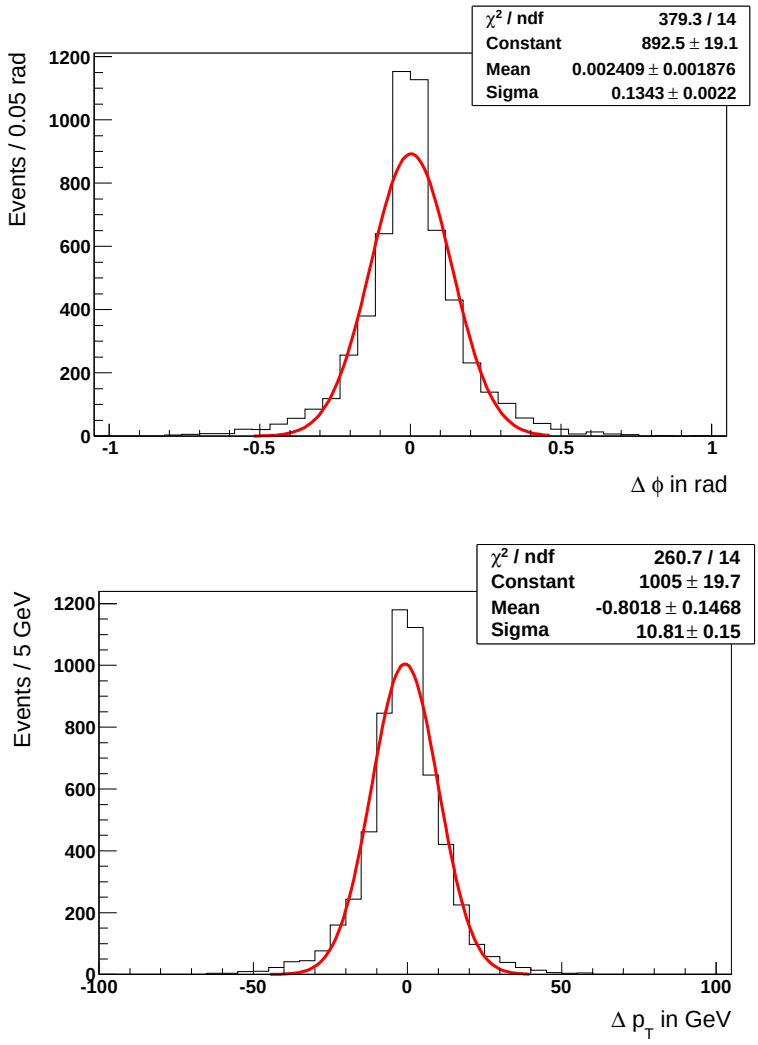

Figure 4.4: *Control plot to check whether the $\not{E}_T$ in the final state is mainly due to the unparticle.*

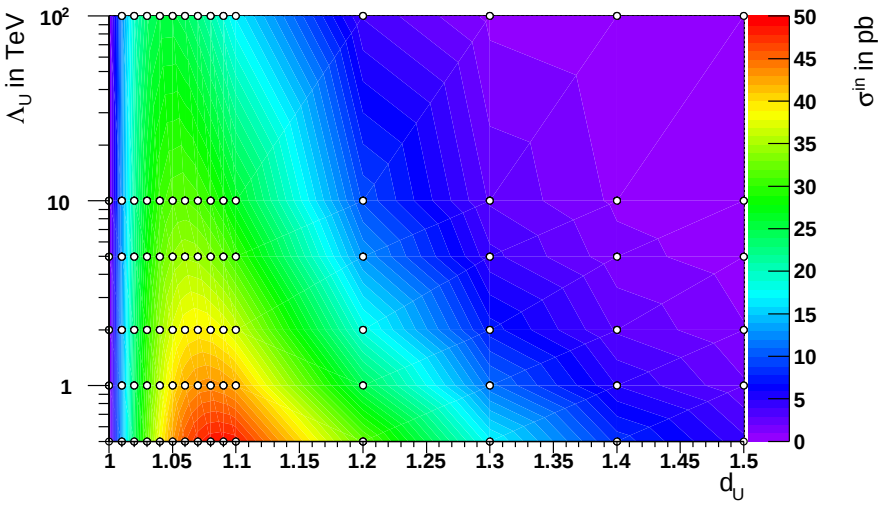

Figure 4.5: *The cross section for real vector unparticle production is shown. It was calculated for the space points marked with a white circle.*

therefore cannot produce hits therein. Only very hard jets with hadronic leakage into the muon system sometimes do so, and again a small fraction of that is falsely reconstructed as isolated. So SM events that do not contain two genuine OS muons are highly suppressed. As described in Sec. 3.3, various effects have an impact on $\not\!\!E_{\mathrm{T}}$ and introduce *fake* $\not\!\!E_{\mathrm{T}}$.

The different backgrounds to this signal can be divided into irreducible ($ZZ \to \mu^+\mu^- 2\nu$) and reducible (other) backgrounds:

- $ZZ \to \mu^+\mu^- 2\nu$: This background is *irreducible*, since it has exactly the same topology as the signal. One Z boson decays muonically and the other one into neutrinos leading to approximately $\not\!\!E_{\mathrm{T}}$ of the amount of Z p_{T}.

- $t\bar{t} \to \mu^+\mu^- + X$: $t\bar{t}$ events play a major role at the LHC, since the tops decay into various final states, ranging from fully hadronic states with six or even more jets to dileptonic states with two leptons, two jets and $\not\!\!E_{\mathrm{T}}$. Thus this background has to be considered in many analyses. Its fairly high cross section – compared to the one of the signal – of 375 pb at NLO makes it even more necessary to deal with it. The almost free tops couple always ($V_{tb} \cong 1$) weakly to b-quarks under radiation of a W. When both W bosons decay muonically into a muon plus a muon neutrino ($W \to \mu\nu$), the signal topology is reproduced. The invariant mass of the two muons is distributed over a wide range and not peaked at the Z resonance, which provides a handle to discriminate $t\bar{t}$ events from signal events.

- $\gamma^*/Z \to \mu^+\mu^- + X$: Drell-Yan events do not contain two muons and physical $\not\!\!E_{\mathrm{T}}$ simultaneously. γ^*/Z can either decay into two charged leptons, or two neutrinos, (or 2 jets) thus containing only one part of the signature. In case γ^*/Z decays into two muons along with occasional fake $\not\!\!E_{\mathrm{T}}$, Drell-Yan contributes to the background. Its cross section is 3700 pb, hence the tails of its $\not\!\!E_{\mathrm{T}}$ distribution have to be taken care of. The higher the amount of fake $\not\!\!E_{\mathrm{T}}$, the lower the possibility to occur. Consequently, a high $\not\!\!E_{\mathrm{T}}$-cut will reduce this contribution.

- WZ with $W \to l + \nu$: In case the Z decays into two muons and the W decays leptonically, the neutrino leads to $\not\!\!E_{\mathrm{T}}$ in the final state and this process contributes to the background. The cross section is comparable with the ZZ cross section, but a third lepton in the finale state allows to readily monitor its contribution. However, a veto on a third lepton has not been applied.

- $W^+W^- \to \mu^+\mu^- + X$: As in $t\bar{t}$, when both W bosons decay muonically, this produces a signal-like signature. The SM cross section for inclusive WW production is 74.1 pb. The invariant $\mu^+\mu^-$ mass distribution is not peaked either, so a huge fraction ($\approx 90\%$) can easily be cut away.

- W +Jets with mis-reconstructed objects: Here, two isolated muons are rare, as one has to be a fake. So only a very limited number of events coming from W +Jets contain the required two OS leptons. Almost never, the combination of the fake and the real muon has an invariant mass around the Z mass. $\not\!\!E_{\mathrm{T}}$ is produced by the neutrino, but usually only of the order of 40 GeV. The huge cross section of 40 nb is more than compensated by the rate with which a fake muon is reconstructed, as

this dominates the probability of being accepted in this case. In the used sample, the probability is 0.5‰. So the bottom line is that the contribution from W +Jets have been considered in this study, but no event passes all selection criteria.

- QCD with mis-reconstructed objects: In order to contribute to the background, two fake isolated muons are needed in QCD events. Prompt muons can occur in B-meson decays, but they are typically not isolated. Hence QCD events can be even more suppressed by a two-isolated-muon requirement. A large amount of transverse energy, produced by multijet events, can lead to higher fake $\not{E}_{\mathrm{T}}$, but huge transverse energy is usually produced in events with high $\hat{p}_{\mathrm{T}}$ and the QCD cross section drops steeply with $\hat{p}_{\mathrm{T}}$. One could argue that it would still lead to problems because of the high cross section (millibarn for low p_{T} events), but additionally the invariant mass of the two (fake) muons has to be close to the Z mass. In combination, those requirements are so uncommonly fulfilled such that none of the $3 \cdot 10^7$ probed events will pass the selection criteria. Hence, its contribution is neglected as well.

A summary of important sample properties is given in Tab. 4.1, where information about the used MC generators, cross sections, k-factors, etc. can be found. The DBS entries are given in Appendix C. The cross sections at NLO have been derived using MCFM in version 5.3 for Z, W +Jets, ZZ, WZ, WW and $t\bar{t}$. The PDFs (CTEQ6L1) are accessed using the LHAPDF library in version 5.7.

The cross section uncertainties Δ_σ were taken from Refs. [77, 78] for Z/W and $t\bar{t}$, respectively. ZZ, WZ and WW uncertainties are estimated adding scale uncertainties [79] and an assumed parton density function uncertainty of 5% in quadrature. The uncertainty on signal cross sections was set to 10%.

process	cross section in pb @ order	Δ_σ	branching fraction	MC generator, all @ order	no. of events
$Z \to l^+l^-$	3700 NLO	2.9%	0.034	MG, FastSIM	9‘921‘728
$t\bar{t}$ incl.	375 NLO	23.4%	0.11*0.11	MG, FullSIM	946‘644
$ZZ \to 2l2\nu$	10.5 NLO	6.0%	0.20*0.034*2	MG, FullSIM	116‘200
WZ incl.	32.4 NLO	7.0%	0.33*0.034	MG, FullSIM	246‘550
WW incl.	74.1 NLO	6.6%	0.11*0.11	MG, FullSIM	204‘722
W +Jets incl.	45‘600 NLO	4.3%	n.a.	MG, FullSIM	9‘426‘092
QCD	up to 10^9 LO	n.a.	n.a	PY, FullSIM	$\approx 3 \cdot 10^7$
$ZZ \to 4l$	10.5 NLO	6.0%	0.034*0.034	MG, FullSIM	264‘350
$\mathcal{UZ}$	< 50 NLO	10%	0.034	PY, FullSIM	$\approx$ 12‘000

Table 4.1: *A summary of sample properties is shown. The branching fraction (BF) is displayed to first digit precision. See Particle Data Book [8] for details. PY stands for Pythia and MG for MadGraph.*

Chapter 5

Analysis

The aim of this study is to evaluate the potential of CMS to discover unparticle stuff via $\not{E}_{\mathrm{T}}$ in the final state. Of course, if no signal can be found, an exclusion limit is set. $\not{E}_{\mathrm{T}}$ can also be produced in weak SM processes, in which a weak gauge boson decays into a lepton and a neutrino. The neutrino usually does not interact within the detector. An imperfect detector with noise and finite resolution as well as an imperfect reconstruction fake $\not{E}_{\mathrm{T}}$, too. Hence a careful selection has to be applied such that events from SM background or events containing fake $\not{E}_{\mathrm{T}}$ are efficiently refused and events containing unparticle physics pass this selection. This is done via so-called cuts on kinematic quantities that are derived based on electronic signals recorded by the different detectors, see Sec. 3.3. The bottom line is, if more events with a particular topology will be found than expected from SM, and this excess is statistically relevant, a signal of new physics is found. Further effort has then to be made to investigate which underlying theory describes best the new physics.

A conventional cut-based analysis perfectly suits the needs of this study, since only few discriminative quantities exists. So the search strategy is rather straightforward. It is not expected that a different technique such as *Boosted Decision Trees* or *Neural Networks* would gain much sensitivity, if at all.

The analysis can be divided into the following steps: Firstly, the selection of events is presented. Then the systematic uncertainties are reviewed. Afterwards, a procedure for estimating sensitivity is introduced, followed by an explanation of the optimization procedure and the developed data driven methods. Lastly, the results are shown.

5.1 Event Selection

In contrast to a lepton collider, which is a "signal machine", a pp collider can be thought of as a "background machine" producing mainly elastic pp and low-p_{T} QCD events. Therefore, high luminosity and good triggering is needed to firstly produce interesting events at a decent rate and secondly find them; a common needle in a haystack problem. The very first selection that is applied to the data is the L1 trigger and the HLT, see Sect. 3.2.5. If no trigger fires, the event is not recorded. The actual trigger thresholds for different trigger menus are yet to be set and fine-tuned. The trigger p_{T} measurement is not very precise, hence a trigger cut should be rather loose in order to collect all possibly interesting events, and harder cuts can be done after offline reconstruction on more precise quantities.

The event selection is rather straightforward and its steps are subsequently presented. They include pre-selection and quality cuts, which are applied on muon quantities, and further physics-motivated cuts on the invariant dimuon mass, on the jet multiplicity and finally on $\not{E}_{\mathrm{T}}$ or Z p_{T}.

Pre-Selection and Quality Cuts

Within the pre-selection only events with two global opposite-sign muons within the detector and trigger acceptance and with p_{T} above a certain minimum are selected. Additionally at least 30 GeV of $\not{E}_{\mathrm{T}}$ is required. The entity of pre-selection and quality cuts[1] are

Pre-selection cuts:

- $\not{E}_{\mathrm{T}} > 30$ GeV,
- Two global, triggered OS muons with $p_{\mathrm{T}} > 10\,\mathrm{GeV}$ and $|\eta| < 2.1$,

Quality cuts:

- Muon global $\chi^2/\mathrm{ndf} < 10$, i.e. combined tracker and muon system,
- Muon number of valid hits > 10,
- Muon isolation in the tracker $< 6\,\mathrm{GeV}$ and in the calorimeter $< 20\,\mathrm{GeV}$ in a cone of $\Delta R < 0.3$,
- Muon compatibility[2] > 1.0, and
- Vertex compatibility: Impact parameter $|d_0| < 2$ mm.

The quantities, which have been cut on, are explained in Sec. 3.3. This ensures that only "good" muons enter the selection and that fakes and non-prompt muons are refused.

The χ^2/ndf distribution for the different background processes and for two signal points[3], are shown in Fig. 5.1. What stands out, is the χ^2/ndf of muons originating from Z bosons. That is not a physical effect, but stems from simulation. All samples with the exception of the Z sample have been simulated using the full simulation – for the Z sample fast simulation was used in order to gain statistics, which is a trade-off to the induced systematic. However, the χ^2/ndf for the Z sample is smaller in FastSIM than in FullSIM. Hence, more background events pass the selection and the result is conservative. The applied cut of 10 GeV is rather loose and does not increase sensitivity, but rejects badly reconstructed muons.

Additionally the tracker isolation for reconstructed muons is depicted in Fig. 5.2, for the same samples as in Fig. 5.1. The tacker isolation is similar for samples with only genuine muons and low expected jet multiplicity. For $t\bar{t}$ and W +Jets the tails are much longer, as more hadronic activity is expected and possible B-mesons from W decays can produce

[1] partly taken from [80]

[2] defined as 0.8*CaloCompatibility + 1.2*SegmentationCompatibility, characterizing how MIP-like the muon behaves whilst traveling through the detector [62]

[3] parameter space coordinates for the two signal samples: $d_{\mathcal{U}} = 1.1$ and 1.5 at $\Lambda_{\mathcal{U}} = 2$ TeV, a high and a low cross section point

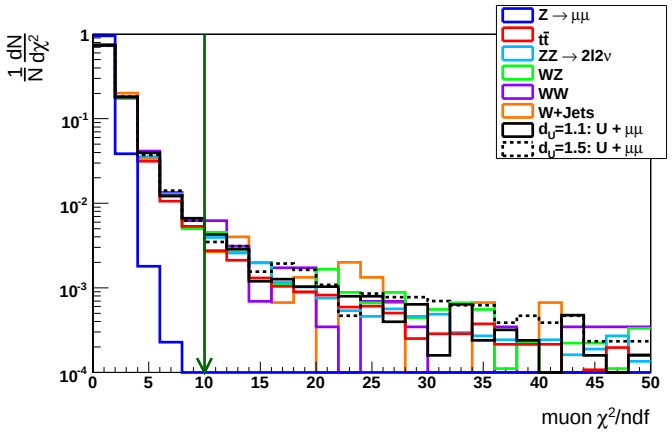

Figure 5.1: *The χ^2/ndf histogram from the muon reconstruction after pre-selection cuts is shown for all background samples and two signal samples normalized to unity.*

non-isolated muons. The applied cut of 6 GeV is again rather loose in order not to cut to hard on the signal yield, but it still cuts away fake and non-isolated muons.

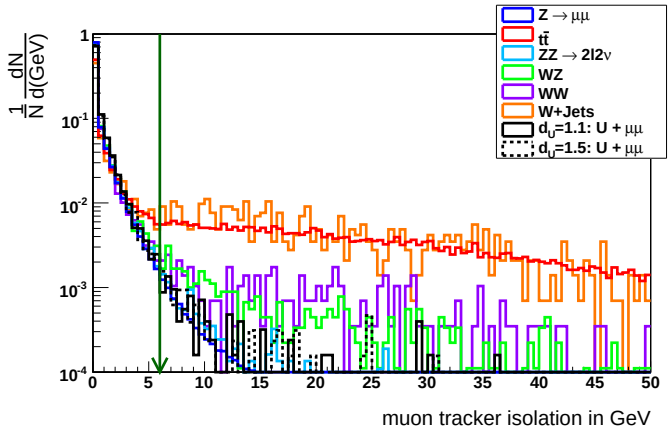

Figure 5.2: *The muon tracker isolation histogram from the muon reconstruction after pre-selection cuts is shown for all background samples and two signal samples normalized to unity.*

Now, after having ensured high muon quality, the signal's significance, which will in detail be defined in Sec. 5.3, has to be enhanced. This is done by applying physics-motivated cuts.

Invariant Dimuon Mass Selection

The mother of the two muons in signal events is a Z boson, hence the invariant mass of the two muons should be close to the Z mass. As the Z has an intrinsic width – it is an unstable particle, so its width is $\Gamma = 1/\tau$ – the distribution of the invariant dimuon mass follow a Breit-Wigner distribution convoluted with a Gaussian distribution with the maximum around the Z mass. By contrast, the invariant mass spectrum of two uncorrelated muons is more or less flat, containing no prominent peak. This motivates a selection criterion

that rejects dimuon events with a reconstructed dimuon mass lying outside of a symmetric window ΔM around the Z resonance.

The reconstructed invariant dimuon mass for all background samples and two signal samples are shown in Fig. 5.3. Used are the two muons with the highest p_{T}. One can easily see that the cut efficiency is best for samples which contain no Z boson. The actual cut value is to be determined by optimization, see Sec. 5.4. $\Delta M = \pm 8\,\mathrm{GeV}$ is used in this analysis.

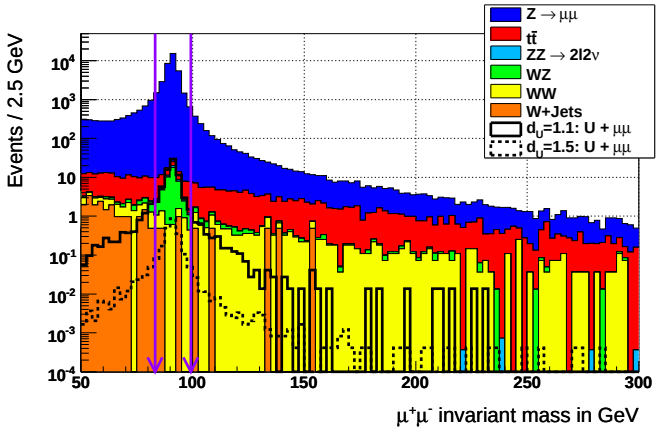

Figure 5.3: *Shown are the invariant mass spectra for all background samples stacked and two signal samples on top after pre-selection and quality cuts.*

Jet Selection

Jets are not of major interest in this study, but still provide information that can be used to discriminate signal and background. No jets are produced at LO for the signal, but for example at least two jets for $t\bar{t}$. Hence the jet multiplicity has significant discrimination power. On the other hand, no one knows how the jet environment will be at the LHC, since there are large uncertainties in the modelling of the parton leftovers from collisions for such high beam energies. So an additional jet in the final state is quite likely, either coming from initial/final state radiation or from some parton remnant. Thus, a *jet veto* could unintentionally cut off a huge fraction of signal events. Hence a *jet cut* on jet multiplicity with $N_{\mathrm{jets}} < 2$ is applied rather than a veto, cf. Fig. 5.4. To study the influence of this cut, the analysis was done without the jet cut for one parameter space point, see Sec. 5.2.

Jets have to be properly selected as well. In this study the jet collection consists of jets within an $|\eta|$ range of 2.5 that have a transverse momentum p_{T} of $50 < p_{\mathrm{T}} < 500$ GeV[4] and deposit at least 5% of their energy in the hadron calorimeter, in order to reject electrons and photons from the jet collection.

The jet multiplicity criterion cuts off approximately 50% of the $t\bar{t}$ contribution but not more than 2% of the signal contribution. The multiplicity for the W +Jets sample seems to be odd, as the zero multiplicity has a propability of one. But keep in mind the previous

[4]Note that requiring a jet $p_{\mathrm{T}} > 30\,\mathrm{GeV}$ results in a *harder* cut in terms of multiplicity since more jets enter the selection, thus having more events with more than one jet.

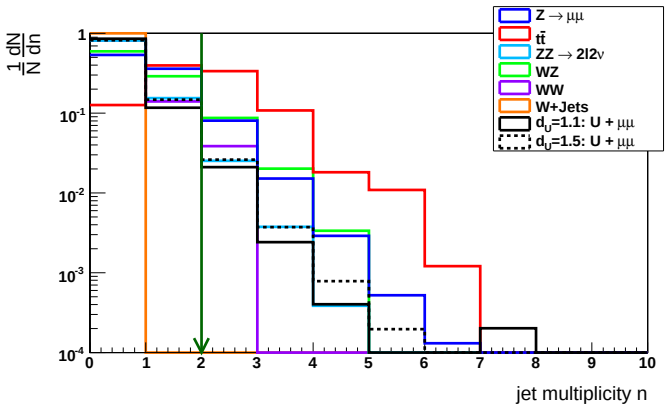

Figure 5.4: *The jet multiplicity is shown for all background samples and two signal samples normalized to unity after pre-selection, quality and invariant mass cut. A jet is an object with at least 50* GeV *reconstructed transverse momentum but not more than 500* GeV*.*

applied cuts. Only one event out of 10^7 produced events passes these criteria, hence only a single bin does contribute.

Missing Transverse Energy or Z p_{T} Selection

$\not{E}_{\mathrm{T}}$ is thought to be experimentally challenging, since it depends on a multitude of variables and all their uncertainties enter in $\not{E}_{\mathrm{T}}$'s uncertainty. In many cases, the uncertainty $\sigma_{\not{E}_{\mathrm{T}}}$ mainly depends on $\sum E_{\mathrm{T}}$, as described in Sec. 3.3.2, but in this study $\sigma_{\not{E}_{\mathrm{T}}}$ depends mainly on the muon resolution, since rather clean events are assured via the selection criteria.

However, if $\not{E}_{\mathrm{T}}$ shall not be a reliable quantity at start-up conditions, a simplified approach to look for unparticles is to search for deviations in the Z p_{T} spectrum in comparison to the SM expectation. The unparticle and the Z boson are recoil partners, providing an additional source of transverse momentum leading to possible differences. Remember that the SM Z boson in Drell-Yan processes can only be boosted by initial state radiation. Of course both strategies could be performed and subsequently combined. This is only reasonable in the case, where a jet cut was applied, since ISR/FSR produces jets resulting in large p_{T} smearing of the Z p_{T} distribution. So if the p_{T} analysis can be kept up with real data has to be investigated. Later on, we will see that the p_{T} analysis is only meaningful for larger integrated luminosity, since the discrimination power is less then in the $\not{E}_{\mathrm{T}}$ analysis.

The $\not{E}_{\mathrm{T}}$ in signal events is highly correlated with the p_{T} of the unparticle, cf. Sec. 4.4. How often an unparticle is produced depends on the cross section, which is a function of the tested parameter space point. The p_{T} distribution of unparticle events is monotonically decreasing. Hence, the optimal cut value for $\not{E}_{\mathrm{T}}$ (p_{T}) is in general parameter space point dependent. This analysis is optimized for best expected exclusion limits, cf. Sec. 5.4. The $\not{E}_{\mathrm{T}}$ (p_{T}) distribution for all background and again two signal samples is plotted in Fig. 5.5 (Fig. 5.6). For the high cross section point, a rough estimate is to cut at 80 GeV $\not{E}_{\mathrm{T}}$ (300 GeV p_{T}). This is quite a difference, which seems odd, since $\not{E}_{\mathrm{T}}$ and Z p_{T} is correlated. However, the discrimination happens earlier in $\not{E}_{\mathrm{T}}$, since muonic Drell-Yan events do not contain physical $\not{E}_{\mathrm{T}}$. So the background is reduced in $\not{E}_{\mathrm{T}}$. For the lower cross sections the separation between signal and background is better for larger $\not{E}_{\mathrm{T}}$ (p_{T}),

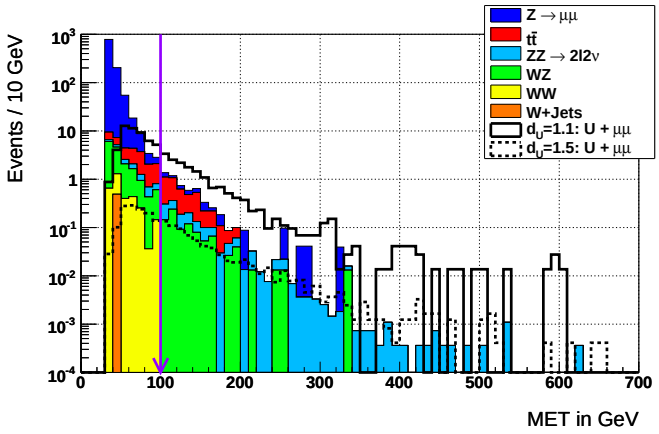

Figure 5.5: *The $\not{E}_{\mathrm{T}}$ spectra are stacked for all background samples and two signal spectra are superimposed in black having applied all previous cuts.*

hence a cut larger than 80 GeV seems reasonable. The optimization revealed that it is not of great importance, where the $\not{E}_{\mathrm{T}}$-cut (p_{T}-cut) is placed. It is set to 100 GeV (300 GeV).

The impact of the various cuts on all background sample and two signal samples is shown in Tab. 5.1. The stated efficiency is an overall efficiency of triggers, acceptance, and analysis cuts. The efficiency is highest for the signal, being 11% to 16%. This seems small, but of course most of the produced events have an unparticle p_{T}, and hence $\not{E}_{\mathrm{T}}$, close to the production cut of 50 GeV.

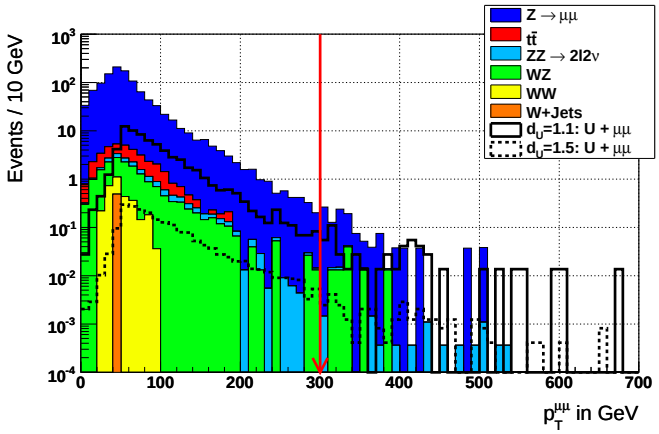

Figure 5.6: *The p_{T} spectra of the combined OS muons are stacked for all background samples and two signal spectra are superimposed in black.*

5.2 Systematic Uncertainties

After having carried out the event selection, the number of signal events passing this selection can be compared to the selected number of background events. How well, if at all, a signal can be seen, will be quantified by statistical tests, but beforehand one has to think about "How precisely do I know the event numbers?", since there are various reasons, why these are not known to infinite precision. These reasons are termed systematic

Cut	No. of surviving events for the given process							
	Z (ll)	$t\bar{t}$	ZZ (2l2ν)	WZ	WW	W +Jets	signal	signal
no cut	367‘103	35‘301	43.1	3205	7431	$3.8 \cdot 10^6$	164	4.8
PS+Q cuts	1470.2	302.9	4.7	21.0	31.1	31.8	79.9	2.4
($\not{E}_{\mathrm{T}} > 100$ GeV)	(5.1)	(76.4)	(1.0)	(1.3)	(2.3)	(0.0)	(20.7)	0.9
$\Delta M^{\mathrm{cut}} = 8$ GeV	1139.8	32.8	3.7	15.7	2.8	0.5	68.3	2.1
	(2.1)	(7.2)	(0.8)	(1.0)	(0.1)	(0.0)	(17.7)	0.8
$N_{\mathrm{jets}} < 2$	1034.3	17.2	3.6	14.0	2.7	0.5	66.4	2.1
$\not{E}_{\mathrm{T}} > 100$ GeV	1.2	3.0	0.8	0.9	0.0	0.0	16.8	0.76
$\epsilon^{\not{E}_{\mathrm{T}}}$	$3.3 \cdot 10^{-6}$	$8.5 \cdot 10^{-5}$	$1.9 \cdot 10^{-2}$	$2.8 \cdot 10^{-4}$	0.0	0.0	0.10	0.16
$p_{\mathrm{T}} > 300$ GeV	1.2	0.0	0.015	0.09	0.0	0.0	0.6	0.03
$\epsilon^{p_{\mathrm{T}}}$	$3.3 \cdot 10^{-6}$	0.0	$3.5 \cdot 10^{-4}$	$2.8 \cdot 10^{-5}$	0.0	0.0	$3.7 \cdot 10^{-3}$	$6.3 \cdot 10^{-3}$

Table 5.1: *The cut-flow is shown for all background and twp signal sample at $d_{\mathcal{U}} = 1.1$ ($d_{\mathcal{U}} = 1.1$) and $\Lambda_{\mathcal{U}} = 2$ TeV. The numbers represent expected numbers of events in 100 pb^{-1} at $\sqrt{s} = 10$ TeV. The last line states the overall efficiency. The bracketed numbers are with a $\not{E}_{\mathrm{T}}$-cut of 100 GeV. PS+Q cuts stands for pre-selection + quality cuts.*

and statistical uncertainties and have to be taken into account whilst calculating their significance.

Systematic uncertainties come from different sources, thus have an impact on all, few, or just one sample such that full, partial, or no correlation at all is present. The considered systematics are listed and described in detail below.

Luminosity

As described in Sec. 3.2.6, there are different ways to determine the luminosity. The one with the smallest expected uncertainty for a search like the presented one, the Z counting method, is used. How the actual value is obtained for this method is described in the Data Driven Methods paragraph, see Sec. 5.5. The luminosity uncertainty is conservatively set to 5%. As the number of expected events is $N_{\text{evt}} = \sigma \cdot \mathcal{L}$ for every sample, the error is fully correlated for all samples.

Cross Section

Cross sections for a wide range of processes like Z, W, and $t\bar{t}$ will be measured with early data and these values and their errors can be used in other analyses. Although there have been no collisions yet, MC studies have been carried out on how well it is expected to measure these cross sections. For other processes, especially double vector boson production, the cross sections are so small that there will be too few events to measure these precisely, or at all, in 100 pb^{-1}. Their cross sections and errors have to be obtained by other means.

An estimate can be achieved by varying the renormalization scale and the factorization scale within reasonable range and monitoring the change in terms of cross section. The largest deviation is taken as *scale uncertainty*. Then parameters of the parton density functions that model the incoming partons can be varied to estimate the *pdf uncertainty*. Both are then added in quadrature and the result is interpreted as the cross section error. The values are given in Tab. 4.1. They are implemented as uncorrelated for all samples, albeit this is not exactly true.[5]

Muon Energy Scale and Resolution

The p_{T} of a muon is obtained by the muon reconstruction and the subsequent fit. The track fit yields different quantities, of which one is the muon p_{T}. By how much a muon is bent depends on the strength of the magnetic field, which is only known to a certain precision. If the strength of the B-field is different from the assumed value, the derived p_{T} has a bias. Another source of error is an imperfect alignment, especially among different detector components, which can lead to systematically higher or lower muon energies in comparison to the true value. The assumed alignment status of the CMS detector in this thesis is *ideal alignment*, although *start-up alignment* – an unaligned detector – was available as well. At first sight, this seems to be a strong source of bias. However, the CMS detector is already aligned to some degree making use of millions of cosmic muons traversing all detector

[5] E.g. the WW and the WZ cross section error is obviously correlated since these processes occur at similar Q^2 such that the parton density function uncertainties at this Q^2 are present in both processes.

components. These have been collected during CRAFT08 and CRAFT09[6] runs. The performance of the muon resolution has been checked and found to be close to the ideal alignment [81]. Hence, assuming ideal alignment is well motivated.

Nevertheless, in order to estimate the impact of misalignment, the analysis has been carried out varying the muon energy scale up and down by 1% for every reconstructed muon and its impact on $\not{E}_{\mathrm{T}}$ and subsequently on significance was studied. This 1% is motivated by results obtained from the MuScleFit[7] group on CRAFT08 data for low p_{T} muons ($\lesssim 200$ GeV) using tag-and-probe methods. The impact on the signal significance is negligible.

The muon resolution characterizes the precision the muon p_{T} can be measured with and this quantity is subject to uncertainties, too. In order to predict the impact of that error, a first approach is to smear the muon's momentum with a Gaussian of reasonable width and compare the resulting significance with the former one obtained for unsmeared muons. If no effect can be seen the error can be neglected. In fact, combining the systematic uncertainty of the muon energy scale and a smearing of 1% of the muon p_{T} changes the significance by less than 0.05σ for parameter space point $d_{\mathcal{U}} = 1.1$, $\Lambda_{\mathcal{U}} = 2$ TeV using 100 pb^{-1}.

In case these uncertainties played a non-negligible role, one would have to consider them fully correlated for all samples.

Jet Energy Scale

Due to various effects that have to be taken into account, the jet energy scale is prone to errors, see Sec. 3.3.2. For 100 pb^{-1} an uncertainty of 5% is expected [66]. A data-driven method, how this value is thought to be obtained is described in [82]. To estimate its impact, the JES was shifted up and down by 10%, and $\not{E}_{\mathrm{T}}$ was corrected accordingly. The analysis was run again and the change in significance was calculated. It is small enough to not be considered further. For an uncertainty of 10% the significance increases by 0.1σ for the JES-down case ans decreases by 0.25σ for the JES-up case for 100 pb^{-1}. This systematic uncertainty of course effects all jets of all samples.

Jet Cut

To study the influence of omitting the jet cut, the analysis was re-run without it for the parameter space point $d_{\mathcal{U}} = 1.1$, $\Lambda_{\mathcal{U}} = 2$ TeV. The significance drops by 0.6σ for 100 pb^{-1}. This is due to more events from $t\bar{t}$ passing the selection.

Sensitivity Dependence of the $\not{E}_{\mathrm{T}}$ Shape

The shape of the $\not{E}_{\mathrm{T}}$ distributions predicted by the MC generators is another source of systematic uncertainty. If these are well described will be subject to studies with real data. In order to estimate the influence of the shape, the analysis was re-run for one parameter space point *without* taking into account the shape. That means, that a usual "one bin"-counting experiment has been performed. To do so, the distributions under study were

[6] Cosmic Run at Four Tesla 2008/2009

[7] **Mu**on **Sc**ale **Fit**

rebinned into two bins, the first one ranging from 0 to 100 GeV and the second one ranging from 100 GeV to 1000 GeV. The significance for $d_{\mathcal{U}} = 1.1$, $\Lambda_{\mathcal{U}} = 2$ TeV decreases by 0.25σ for 100 pb^{-1}.

Monte Carlo Statistical Uncertainty

In MC generation the probabilistic nature of particle interaction is modeled using random number generation. They are prone to statistical fluctuations. At a given integrated luminosity $\mathcal{L}$ the number of expected events for a given process with cross section σ is

$$N_{\text{exp}} = \mathcal{L} \cdot \sigma. \tag{5.1}$$

For every process a certain number of events N_{sim} has been generated, resulting in a weight w with $w = \frac{\mathcal{L} \cdot \sigma}{N_{\text{sim}}}$, which is applied to every generated event. But not all events make it into the final selection, hence only $N_{\text{exp}}^{\text{cut}} = w \cdot N_{\text{sim}}^{\text{cut}}$ are expected to pass the selection. The random error on the number of expected events passing the selection is then

$$\sigma_{N_{\text{exp}}^{\text{cut}}} = w \cdot \sqrt{N_{\text{sim}}^{\text{cut}}}. \tag{5.2}$$

In general, this is true for every bin. However, if statistics are low, most of the entries would be zero. Hence, the error is calculated for the whole contemplated region and is used as an upper limit estimate on the per-bin error. If the error on the whole contemplated region is small, the error in each bin is even smaller than that.

Another problem arises, when too few events have been produced resulting in large weights. Particularly with regard to samples, where no events pass early selection criteria, the efficiency of later steps can not be determined, forcing the analyst to apply an 68% upper limit of

$$N_{\text{exp}}^{\text{cut}} = 1.15 \frac{\mathcal{L} \cdot \sigma}{N_{\text{sim}}}. \tag{5.3}$$

The importance of the MC error can be estimated as follows. The weights can be determined from bare event numbers or their corresponding integrated luminosity, as $w = {}^{N_{\text{exp}}}/_{N_{\text{sim}}} = {}^{\mathcal{L}_{\text{exp}}}/_{\mathcal{L}_{\text{sim}}}$. For all but QCD and W +Jets processes, a corresponding luminosity of at least 2.5 fb^{-1} is available in comparison to the assumed 100 pb^{-1} used in this study. For signal processes a corresponding luminosity of 10 to 100 fb^{-1} was produced. Hence, $w < {}^{1}/_{25} = 0.04$. If $N_{\text{sim}}^{\text{cut}} \approx 6$, the random error on the number of expected events passing the selection is of the order $w\sqrt{6}$ and the relative one $w/\sqrt{6} = 0.016$, so $< 2\%$. Consequently, the MC error has been neglected in this analysis.

5.3 Statistical Method

A statistical test was carried out in order to quantify, how well the sought-after signal can be excluded in its absence or be seen in its presence in the data. Mathematically seen, this is a hypothesis test [83]. First, a *null hypothesis* is formulated. This is the hypothesis stating that the SM is valid and that there is no new physics beyond it. The *alternative hypothesis* states that there is new physics leading to non-SM contributions in the distribution of the studied quantity.

To perform the statistical test, a quantity that distinguishes between the two hypotheses, i.e. a so-called *test statistic*, has to be defined. This test statistic can in general be freely chosen, but it makes sense to choose it such that it best separates the two hypothesis and minimizes the possible error rate. There are two errors in statistics: The "error of the first kind", representing the probability to falsely discover an absent signal and the "error of the second kind", stating the probability of excluding a signal albeit its presence.

These two probabilities, traditionally called p-values, define the significances, with which the hypotheses can be rejected. In oder to claim a discovery, the error of the first kind is requested by convention to be smaller than $2.85 \cdot 10^{-7}$ - motivated by the probability for a Gaussian, one-sided 5σ deviation – and in the absence of a signal, the error of the second kind, again by convention, has to be smaller than 5% – motivated by a two-sided, 2σ deviation. Hence, an exclusion usually requires less data than a discovery. Significance can be expressed in bare probability, but is traditionally translated in Gaussian standard deviations.

The CL_s-method [84–86] provides a framework to obtain the error rates explained above. The implementation that is used in this work is called HybridCalculator [87]. It is part of the RooFit package [88], which is an add-on to ROOT [89]. The HybridCalculator calculates confidence levels (CL) that are identified with the error rates. If this identification is valid is in general to be proven by a coverage test, i.e. studying the coverage for the particular application of the CL_s method. This test is not performed within this thesis, and has not been performed yet in general. An example for a coverage test performed on a different statistical method can be found in Ref. [74]. But it has been argued [90] that the CL_s-method by construction overcovers. In other words, the false exclusion and the false discovery rates are less or equal to the confidence levels calculated via the CL_s-method. Only in pathological cases like counting experiments with small numbers of events, the false discovery rate can undercover.

The Test Statistic

A common ansatz to discriminate *signal+background* from *background only* is to just count event numbers in a certain region of a distribution. That may be $\not{E}_{\mathrm{T}}$, invariant mass, a neural network output, or any other quantity one can think of. In case the background shape is different from the signal+background shape, a *per-bin counting experiment* can gain sensitivity. A per-bin counting experiment counts event numbers in a certain region as well, namely in a bin, but the combination of individual channels is the crucial point. The event numbers in every bin of the quantity's distribution under inspection can be interpreted as an independent Poisson counting experiment with mean μ and probability distribution

$$P(\mu; n) = \frac{\mu^n \mathrm{e}^{-\mu}}{n!}, \tag{5.4}$$

with the probability $P(\mu; n)$ to find n events if μ are expected. μ reflects the underlying hypothesis and is set to the number of events expected under one such hypothesis, i.e. $\mu = s + b$ or $\mu = b$. b $(s + b)$ reflects the number of events expected under the background only (signal+background) hypothesis; of course s depends on the parameter space point.

The likelihood ratio Q_i of the two, defined as

$$Q_i(d_{\mathcal{U}}, \Lambda_{\mathcal{U}}) = \frac{P(\mu = s_i(d_{\mathcal{U}}, \Lambda_{\mathcal{U}}) + b_i; n_i)}{P(\mu = b_i; n_i)} \qquad n \in \mathbb{N}_0\,,\ \mu > 0 \tag{5.5}$$

with the number of expected signal (background) events s_i (b_i) in the i-th bin, quantifies if the actually measured event count n_i in this bin is rather *signal+background-* or *background only*-like, i.e. Q_i being larger or smaller than unity, respectively. In fact, the Neyman-Pearson lemma [91] states that using this likelihood ratio minimizes the type I and type II error rates. In order to collect the information from every bin in one number,

$$Q(d_{\mathcal{U}}, \Lambda_{\mathcal{U}}) = \prod_{i=1}^{N} Q_i(d_{\mathcal{U}}, \Lambda_{\mathcal{U}}) \tag{5.6}$$

is calculated and for convenience converted further to -2ln$Q$ [92].

As described in Sec. 5.1, the final variables to perform the statistical test on, is the $\not{E}_{\mathrm{T}}$ or alternatively the Z p_{T} distribution as a simplified approach.

The HybridCalculator

The test itself requires some detailed explanation. The HybridCalcultor, as already referred to in its name, is a hybrid method that calculates Frequentist confidence levels, but allows for Bayesian treatment of systematics. That means, that the determination of significance is done by repeating *pseudo-experiments* – as well called *toy experiments*. Within every repetition, systematic and random errors are considered, resulting in different possible outcomes. The knowledge about the systematics are included via priors. A prior is a pdf describing the shape of the assumed systematic. These priors are being marginalized[8] by means of repetition. The various outcomes, i.e. different Qs, are then filled into a histogram. This is done for data diced according to the *signal+background* and the *background only* model. Hence, there are always two distributions to be looked at.

The procedure for every toy experiment goes as follows. One toy experiment consists of different steps. At first, the distribution of the variable in question ($\not{E}_{\mathrm{T}}$ or p_{T}) is interpreted as an extended probability density function, with the normalization being the expected number of events in the inspected range. This distribution is obtained with an corresponding luminosity of approximately 2.5 fb^{-1} or more. Therefore, this template pdf has a very small statistical error. The template pdf is done for every sample, namely the various background samples plus the signal samples, hence for every parameter space point. Since the expected number of events $N_{\mathrm{exp},i}$ for sample i, cf. Eq. 5.1, is subject to uncertainties, the uncertainty of luminosity and cross section are considered. This is implemented making use of two relative factors being diced using the assumed priors: For the cross section a Gaussian G^{xs} with $G^{\mathrm{xs}} = G(\sigma_{\mathrm{corr}}; 1, \sigma_{\hat{\sigma}})$ and for the luminosity a Gaussian G^{lumi} with $G^{\mathrm{lumi}} = G(\mathcal{L}_{\mathrm{corr}}; 1, \sigma_{\hat{\mathcal{L}}})$ is assumed, where $\sigma_{\hat{X}}$ is the systematic

[8] Be $P(A)$ ($P(B)$) the probability of event A (B). The marginal probability is then the unconditional probability $P(A)$ of the event A; that is, the probability of A, regardless of whether event B did or did not occur. If B can be thought of as the event of a random variable X having a given outcome, the marginal probability of A can be obtained by summing or, more generally integrating, the joint probabilities over all outcomes for X.

uncertainty on the quantity's mean $\hat{X}$. Both Gaussians are centered around unity. Hence, $N_{\text{exp},i}$ can be decomposed as

$$N_{\text{exp},i} = \hat{\mathcal{L}} \cdot \mathcal{L}_{\text{corr}} \cdot \hat{\sigma} \cdot \sigma_{\text{corr}}. \tag{5.7}$$

The used error values are to be found in Sec. 5.2 or in Tab. 4.1. The resulting $N_{\text{exp},i}$ are then the weights for adding up all background pdfs forming the *background only model* and all background+signal pdfs forming the *signal+background model*. The normalization of these two models are thus $\sum N_{\text{exp},i}$, where the sum runs over the considered samples, so only background samples for the background only model and background and signal samples for the background+signal model.

For each model, the HybridCalculator then draws one number N'_{exp} from a Poisson $P(\mu)$ with mean μ being the normalization $\sum N_{\text{exp},i}$ of one of the two models to account for the random error. Then the HybridCalculator dices N'_{exp} *unbinned* pseudo data events according to the model's pdfs. Although the pdf looks like a binned distribution – it is constructed from binned MC distributions – it is an unbinned one. This is important for the construction of the likelihood ratios. For simplicity's sake, above statements explained the construction of the likelihood ratio for a *binned* data set making use of a Poisson-ratio. The construction of the test statistic used in the HybridCalculator is a smidgen more difficult, more general. Now, a negative log-likelihood ratio -2ln$Q$ of *extended* log-likelihood functions according to the two hypotheses ($\mathcal{L}^E_{sb}$ and $\mathcal{L}^E_b$) is used, cf. [93], with

$$Q = \frac{\mathcal{L}^E_{sb}}{\mathcal{L}^E_b}, \text{ and } \mathcal{L}^E = \mathcal{L}^E(\underline{x}; \theta, \mu) = \frac{\mathrm{e}^{-\mu}\mu^n}{n!} \prod_{i=1}^{n} f(x_i; \theta). \tag{5.8}$$

The Poisson pdf expresses the probability of obtaining $n = N'_{\text{exp}}$ events, when the expected number of events is $\mu = \sum N_{\text{exp},i}$. The product runs over n diced data points x_i with $n = N'_{\text{exp}}$ and $f(x_i; \theta)$ is the pdf describing either the SB model or the B model.

Summarizing, the HybridCalculator dices unbinned datasets according to the models taking into account systematics via priors, calculates the negative log-likelihood ratios and fills them into histograms. Hence the histograms for the two hypotheses each contain N_{toys} entries.

The Interpretation

After having carried out all pseudo-experiments, the two resulting histograms, the $-2\ln Q$ distribution for the background (B) model and the signal+background (SB) model, see an example in Fig. 5.7, have to be analyzed. By definition, the median of the SB model is in the negative range, since for SB-like data, the nominator in Eq. 5.5 is larger than the denominator and hence its negative natural logarithm is smaller than zero, and vice versa for B-like data. One could think of using the separation of the medians as a measure of the sensitivity. This fails, since the RMS values of the two distributions could be large and thus the two $-2\ln Q$ distributions overlap. The RMS values depend of course on the assumed systematic errors. A first approach would rather be to look at the separation divided by the sum of RMS values.

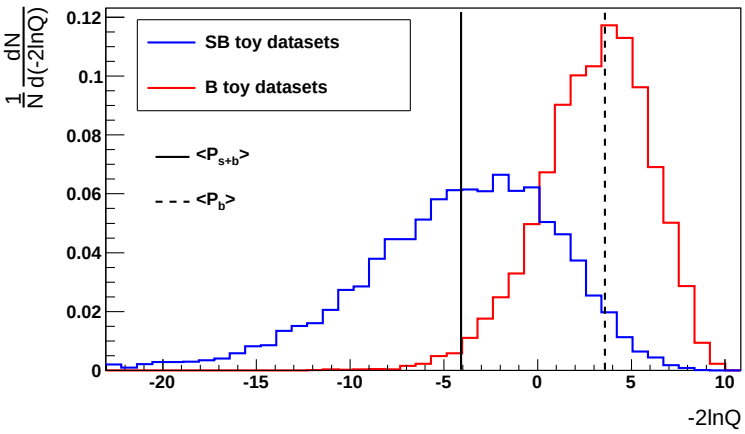

Figure 5.7: *Examples of the $-2\ln Q$ distribution for both hypotheses.*

The distributions may look Gaussian in some cases, but there is no general functional form, which these distributions follow. However, for every distribution a 68% region[9] around the median can be delimited, meaning that 68% of the toy experiment's Qs are within this region, stated as 1σ vicinity, see Fig. 5.8. This region is used to estimate a statistical error on the significance, see error bands in the plots in the results section.

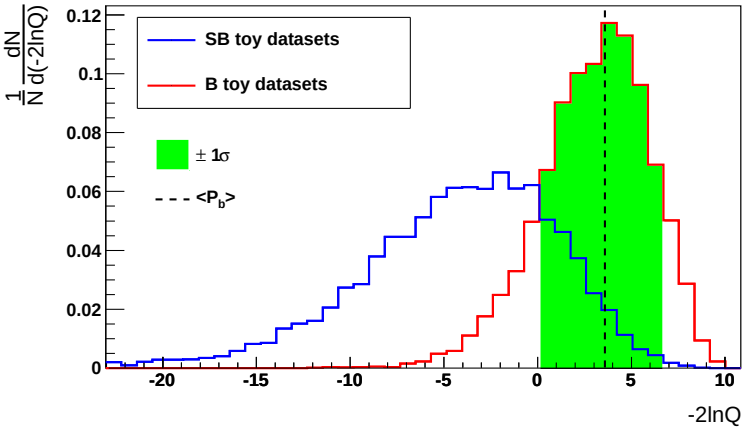

Figure 5.8: *CL_s plot with hatched 68% regions.*

Be $x \equiv -2\ln Q$ and $\mathcal{P}_b(x)$ ($\mathcal{P}_{s+b}(x)$) the $-2\ln Q$ distribution interpreted as pdfs with normalization N_{toys} for the B-model (SB-model). With these pdfs the confidence levels for the two hypotheses are defined. The integral

$$CL_b = \int_{X_0}^{\infty} \mathcal{P}_b(x)dx \tag{5.9}$$

is being analyzed in order to determine if the B-only hypothesis is true. The lower integration border X_0 corresponds to the $-2\ln Q$ measured by data or is obtained by yet

[9] motivated by a Gaussian 1σ vicinity

another single toy experiment or is set to be the median of $\mathcal{P}_b(x)$ obtained by MC. In the absence of data, the latter option is the most reasonable one, because the median reflects the $-2\ln Q$ value with 50% possible outcome on each side under perfect modeling of the experimental environment.

Now, X_0 can in general be found to be on the right-hand side of the the median of $\mathcal{P}_b(x)$, $\langle\mathcal{P}_b(x)\rangle$, meaning that even less events than under the B-only hypothesis are found. This is possible in case new physics lead to destructive interference effects. CL_b is then smaller than 0.5. X_0 close to $\langle\mathcal{P}_b(x)\rangle$ results in a CL_b around 0.5 reflecting no deviation from the SM, cf. Fig. 5.9 (left). In the last case where X_0 is on the left-hand side of $\langle\mathcal{P}_b(x)\rangle$ the data contains more than just background events and CL_b is larger than 0.5.

This modus operandi is repeated for the signal+background case. CL_{s+b} is defined as

$$CL_{s+b} = \int_{X_0}^{\infty} \mathcal{P}_{s+b}(x)dx \tag{5.10}$$

and an X_0 larger than $\langle\mathcal{P}_{s+b}(x)\rangle$ means that less then the expected signal+background is measured and CL_{s+b} is smaller than 0.5. An X_0 close to $\langle\mathcal{P}_{s+b}(x)\rangle$ reflects the coincidence of expected and measured signal+background events resulting in an CL_{s+b} of 0.5, cf. Fig. 5.9 (right). If even more events are found in data, X_0 is smaller than $\langle\mathcal{P}_{s+b}(x)\rangle$ and thus CL_{s+b} is larger than 0.5.

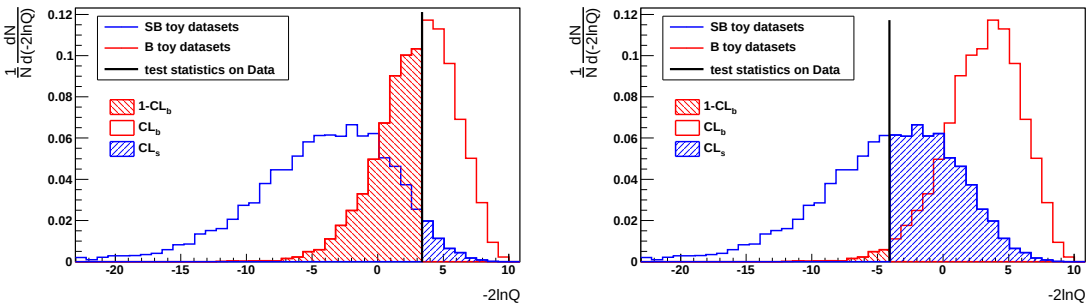

Figure 5.9: *CL_s plots with two possibilities of X_0.*

As mentioned above, the identification between error rates and confidence levels has to be made. $1 - CL_b$ is interpreted as the type I error rate and CL_{s+b} as the type II error rate. Hence, a discovery can be claimed if an excess of more than 5σ is measured in data:

$$1 - CL_b \leq 2.85 \cdot 10^{-7}. \tag{5.11}$$

A problem arises, as computing time is limited, such that only a limited number of toy experiments N_{toys} can be generated. This results in model pdfs that are exactly zero for certain regions smaller and larger than the median, i.e. the pdf dies out. The larger N_{toys}, the larger is the region populated by the pdf. Consequently, the integrals that are calculated to determine CL_b and CL_{s+b} are only known to a certain precision. In order to make a proposition about a one-sided 5σ deviation, at least the inverse times of toy experiments have to be carried out, thus approximately 3.5 million. Then, there is a good chance that ONE outcome ($-2\ln Q$) lies outside of the integral borders, giving a CL_b value larger than

zero but smaller or equal to $2.85 \cdot 10^{-7}$. The statistical uncertainty on that one outcome is one. A statistically satisfying result would rather be 10 with an uncertainty of three requiring the generation of 35 M toy experiments. 35 K toy experiments – corresponding to 4σ – need about 2 h to be run and computing time scales linearly; 2000 h for 35 M events is a reasonable estimate for a single job. This is too much and unwieldy as multi-threading is not available. In order to abate CPU time, N_{toys} is set to 33 K for the $\not{E}_{\text{T}}$ analysis and to 10 K for the p_{T} analysis and hence for both the CL_b has to be obtained by other means.

An approach is to fit a function to the tail of $\mathcal{P}_b$ and hence extrapolating the pdf to unpopulated regions. The integral from $-\infty$ to $\langle \mathcal{P}_{s+b}(x) \rangle$ normalized to the overall integral is then an estimate for $1 - CL_b$:

$$1 - CL_b = \frac{\int_{-\infty}^{\langle \mathcal{P}_{s+b}(x) \rangle} \mathcal{P}_b(x)}{\int_{-\infty}^{+\infty} \mathcal{P}_b(x)} = \frac{\int_{-\infty}^{\langle \mathcal{P}_{s+b}(x) \rangle} \mathcal{P}_b(x)}{N_{\text{toys}}} \tag{5.12}$$

As the analytical form of the tails is unknown, different functions have been fitted:

- Rational function: $C \frac{1}{(x-x_0)^2}$ fitted to the left tail of $\mathcal{P}_b$,
- Exponential: $\exp\{C + ax\}$ fitted at the left tail of $\mathcal{P}_b$,
- Voigtian: A convolution of a Breit-Wigner distribution with a Gaussian distribution fitted to $\mathcal{P}_b$ over the whole region.

An example – for $d_{\mathcal{U}}$ =1.2 and $\Lambda_{\mathcal{U}}$ =2 TeV and 1 fb^{-1} integrated luminosity – showing these three possibilities is given in App. B. The Voigtian fit shows the smallest χ^2/ndf of 1.5. The exponential fit has a χ^2/ndf of 2.4 and the rational function a χ^2/ndf of 59.3. These numbers and the plots in App. B suggest the usage of the Voigtian fit. However, for smaller statistics the $-2 \ln Q$ distribution is usually deformed and/or spiky, making a fit over the whole range impossible. Since the exponential fit is only done in the tail and provides a reasonable χ^2/ndf, this fit is used in this analysis to calculate $1 - CL_b$.

As an exclusion limit is usually set by convention at 95% CL, so for the CL_{s+b} value applies $1 - CL_s \leq CL$, hence:

$$CL_{s+b} \leq 0.05. \tag{5.13}$$

A careful inspection of the performance of CL_{s+b} revealed unphysical effects in regions with little or no signal resulting in too strong exclusion limits [84–86]. A remedy provides the modified Frequentist re-normalization to the CL observed for the background only hypothesis

$$CL_s \equiv \frac{CL_{s+b}}{CL_b}, \tag{5.14}$$

which is proven to be conservative. Bottom line is, the exclusion at 95% CL is given by

$$CL_s \leq 0.05. \tag{5.15}$$

5.4 Optimization

In order to set the best possible exclusion limit, an optimization was performed varying the cut parameters $\not{E}_{\mathrm{T}}^{\mathrm{cut}}$ and ΔM^{cut}. The $p_{\mathrm{T}}^{\mathrm{cut}}$-value was not optimized. In general, this is best be done for every point in unparticle parameter space individually. Starting with parameter space point ($d_{\mathcal{U}} = 1.5, \Lambda_{\mathcal{U}} = 2$ TeV) revealed that an optimization does not have a huge impact on expected limits. So the optimization was performed for this one point and inherited to the others. Shown are the CL_s values in a matrix of different $\not{E}_{\mathrm{T}}^{\mathrm{cut}}$ and ΔM^{cut} values. At the white points the analysis was run. It is clear from Fig. 5.10 that the cut values have little impact on the derived CL_s value, as CL_s only changes by a few percent over the whole contemplated region. However, of the two ($\not{E}_{\mathrm{T}}^{\mathrm{cut}}$,$\Delta M^{\mathrm{cut}}$)-pairs with the best limit, (80,4) and (100,8), the latter one is chosen. The higher $\not{E}_{\mathrm{T}}^{\mathrm{cut}}$ value reduces the impact of fake $\not{E}_{\mathrm{T}}$ and the larger ΔM^{cut} increases the number of signal events passing the selection.

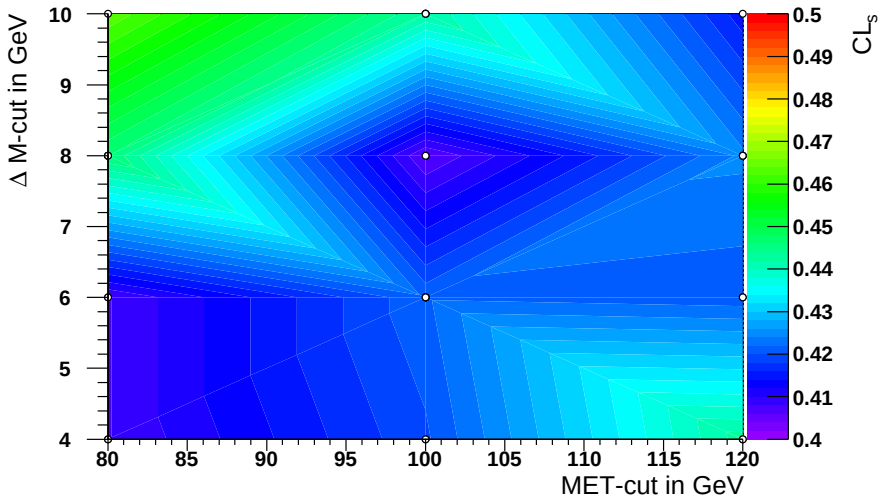

Figure 5.10: *Shown are the CL_s values in a matrix of different $\not{E}_{\mathrm{T}}^{\mathrm{cut}}$ and ΔM^{cut} for 1* fb^{-1}.

The impact of the cut values on the expected limits are even smaller for the Z p_{T} analysis, since the shape of the background and the signal distribution are even more similar. Hence, the optimization was not performed and the $p_{\mathrm{T}}^{\mathrm{cut}}$ was set to 300 GeV.

Thus, the entity of used cuts are:

- Pre-selection cuts,
- Quality cuts, cf. Sec. 5.1
- Reconstructed invariant dimuon mass within $m_Z \pm 8GeV$,
- Jet multiplicity $N_{\mathrm{jets}} < 2$ with jet p_{T} between 50 and 500 GeV, and
- $\not{E}_{\mathrm{T}} > 100$ GeV or $p_{\mathrm{T}} > 300$ GeV.

5.5 Data Driven Methods

Once data will be available, the data cannot only be used in order to search for signals, but as well to check, if the MC generators simulate the background appropriately. E.g. QCD is quite complicated to model, therefore its estimation from data is the preferred choice. Another example is to extract the luminosity from data. In general, these methods are coined *data driven methods*. Due to a lack of real data, MC data is used to show how the procedures work. The main question to be answered is "What if don't trust my MC generator?". To answer this question again with MC data sounds illogical, but this is rather a proof of principle and shows that the methods are in place, ready for data taking.

The main backgrounds to the signal come from Z, $t\bar{t}$, ZZ and WZ. The Z contribution is expected to fall very rapidly with increasing $\not{E}_{\mathrm{T}}$, since the higher the amount of fake $\not{E}_{\mathrm{T}}$, the lower is its probability to occur. Unfortunately, there is no method in place to predict the $\not{E}_{\mathrm{T}}$ distribution from Z with data driven means. But in order to cross-check, if the distribution can be trusted, the significance is studied under variation of muon energy scale and resolution, see Sec. 5.2. WZ can be monitored measuring the rate of events that pass all selection criteria and have a third lepton in the final state. So I will concentrate on $t\bar{t}$ and ZZ data driven estimations as well as luminosity estimation.

5.5.1 $t\bar{t}$ Estimation (ABC-method)

In case one does not trust the $\not{E}_{\mathrm{T}}$ distribution of $t\bar{t}$ events, one can try to estimate this distribution by other means, e.g. looking at events that are not within the ΔM^{cut}, but lie outside of this region, the so called sidebands. Of course the sidebands are to be selected "not too far" from the Z resonance in order to assure reasonably similar kinematic properties. The left sideband was chosen to range from $(m_Z - 20\ \mathrm{GeV})$ to $(m_Z - 10\ \mathrm{GeV})$, and the right sideband from $(m_Z + 10\ \mathrm{GeV})$ to $(m_Z + 20\ \mathrm{GeV})$, cf. Fig. 5.11. Only pre-selection and quality cuts have been applied for Fig. 5.11.

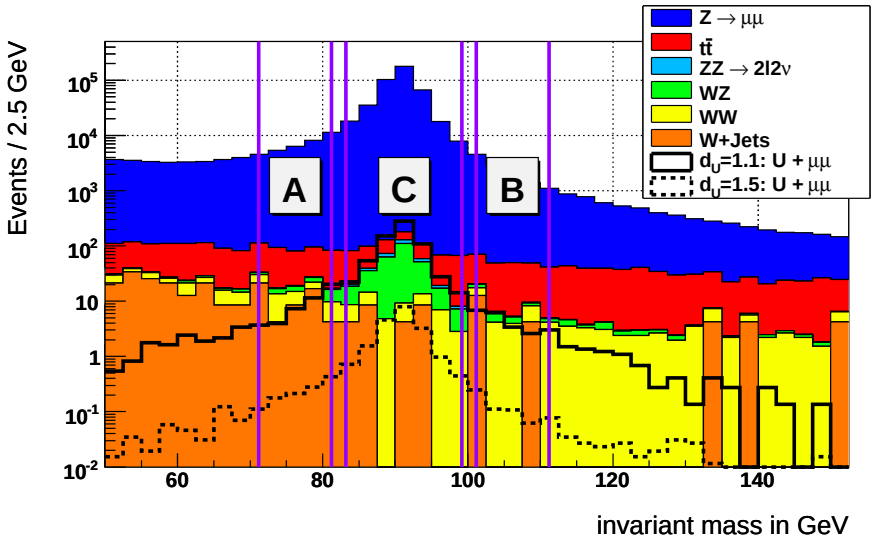

Figure 5.11: *Visualization of the used regions in the ABC method.*

The scheme is to add up the $\not{E}_T$ distributions for events in regions A and B in order to predict the one for those in C. Within these sidebands, the contributions from different backgrounds are shown in Fig. 5.12.

In the left sideband (A) above 100 GeV $\not{E}_T$, Z contributes with 1.5 events, $t\bar{t}$ with 54.2, WW with 1.1 and signal, at a high (low) cross section, with 5.9 (0.2), and the other backgrounds with less than one. For the right sideband (B): Z with 0.4, $t\bar{t}$ with 32.1, WW with 1.3 and signal 4.7 (0.1), the rest is again smaller than one. Thus we have a 10% possible signal contamination, and $t\bar{t}$ contributes most to the total background. The three $\not{E}_T$ distributions for $t\bar{t}$ alone are displayed in Fig. 5.13, for the signal region C (black), the left sideband A (red) and the right sideband B (green). The two $t\bar{t}$ sidebands are being added linearly and rescaled, since the two sidebands cover a mass region of 20 GeV– the signal only 16 GeV. The normalization is performed in the range from 60 to 90 GeV. The prediction, plotted in orange, agrees nicely with the MC from the signal region. This can be seen as a closure test. The jet cut was not applied within this method, since this would reduce statistics unnecessarily, and in order to avoid a jet energy scale dependence.

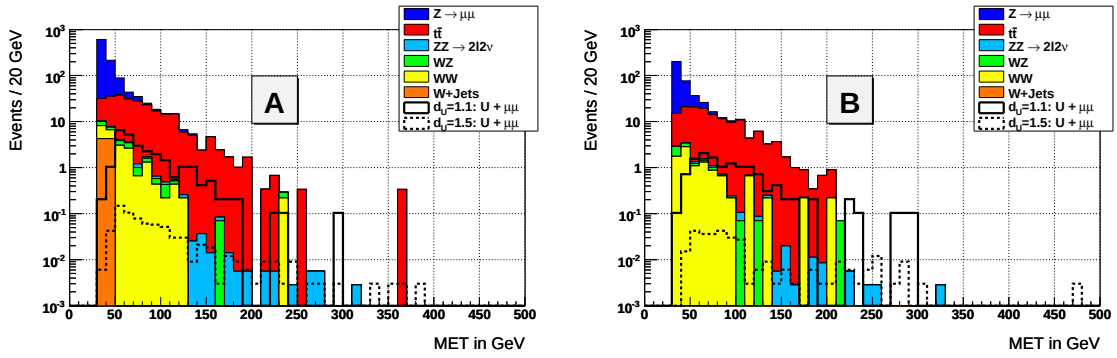

Figure 5.12: *For the sidebands, every contribution to the $\not{E}_T$ distribution is shown. $t\bar{t}$ dominates over all other backgrounds for $\not{E}_T > 100\,\text{GeV}$, the unparticle "contamination" depends on the assumed parameter space point, but is less than 10%.*

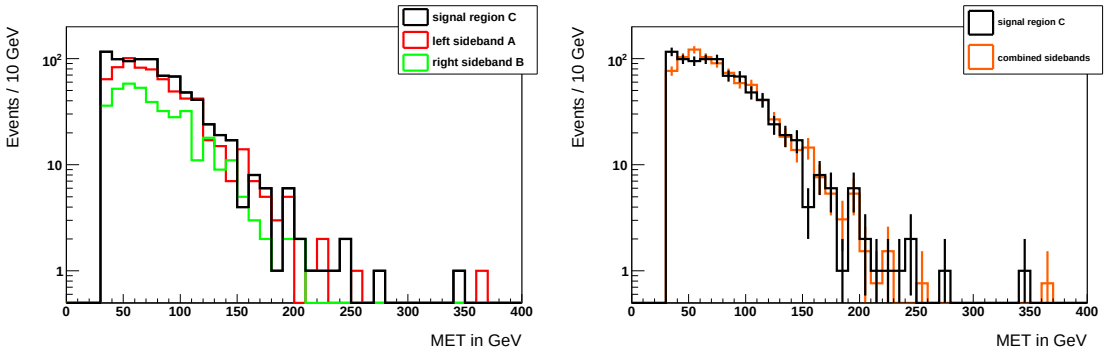

Figure 5.13: *The $\not{E}_T$ distributions from $t\bar{t}$ in the signal region (black) and the sidebands (green and red) is displayed (left) and the comparison of the combination (orange) of them to the $\not{E}_T$ distribution in C (right).*

The above method was done using the $t\bar{t}$ dimuon channel. There is as well the possibility to use the electron-muon channel with an invariant mass within the signal region. Since γ^*/Z does not decay into eμ, there would be no contribution from Drell-Yan. This approach has not been followed yet.

Additionally, counting $t\bar{t}$ events in the sidebands can be used to estimate the $t\bar{t}$ cross section uncertainty. The systematics are expected to be small, and the statistical error on the number of events in the sidebands is estimated as the square root of the sum of them $\sigma_{t\bar{t}} = \sqrt{54.2 + 32.1} = 9.3$ events, such that the relative error is approximately 10%, which is used in the analysis.

5.5.2 ZZ Estimation (422-method)

In order to estimate the ZZ $\not\!\!E_{\mathrm{T}}$ distribution, the following approach is used. One expects the kinematics for $ZZ \to 2l2\nu$ to be the same as for $ZZ \to 4l$. Four muons are rather easy to identify, whereas $ZZ \to 2l2\nu$ can be hard to distinguish from $Z \to 2l$. Two out of four muons are subtracted, hence the naming convention: muon multiplicity is changed from **four to two**.

So after reconstructing both Z bosons by finding the best combination of the four muons, the 4-vector of one randomly selected Z is subtracted from the $\not\!\!E_{\mathrm{T}}$ 4-vector. Hence, artificial $\not\!\!E_{\mathrm{T}}$ is introduced, as if two muons had been neutrinos. In Fig. 5.14 both, the original (black) and the artificial (red), $\not\!\!E_{\mathrm{T}}$ distributions from $ZZ \to 4l$ are shown. The red one is now compared to its counterpart from $ZZ \to 2l2\nu$. The normalization is done by applying a factor c_{422} that accounts for different branching fractions and selection efficiencies:

$$c_{422} = \frac{BF(Z \to \nu\nu) \cdot \varepsilon(4\mu)}{BF(Z \to \mu\mu) \cdot \varepsilon(2\mu 2\nu)}. \tag{5.16}$$

The good consistence shows the feasibility of the 422-method, and even not all possible corrections have been applied. For example, muon energy deposits in the calorimeter have not been corrected for. This "proves" the MIP characteristic of the muon.

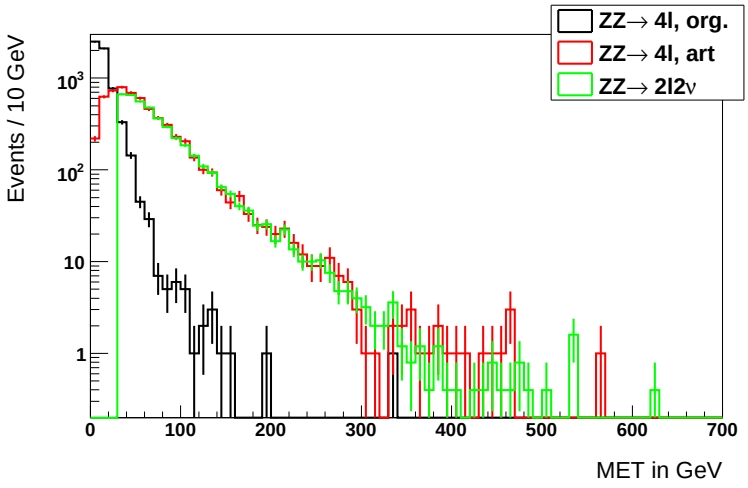

Figure 5.14: *The original $\not\!\!E_{\mathrm{T}}$ distribution from $ZZ \to 4l$ is shown in black, the artificially enhanced one in red, and the normalized $\not\!\!E_{\mathrm{T}}$ distribution from $ZZ \to 2l2\nu$ in green.*

For 100 pb^{-1}, the expected numbers of events for $ZZ \to 4l$ is about 10, maybe six events would be reconstructed containing four muons each with $|\eta| < 2.1$. This would lead to a relative statistical error of 40%. Hence, for the analysis the theoretical uncertainties quoted in table 4.1 are used and not the one derived within the 422-method. Once sufficient data will be collected such that the statistical error is smaller than the theoretical one, this should be done vice versa.

Even much smaller will be the number of $ZZ \to 4l$ events with $\not{E}_{\text{T}} > 100$ GeV. Hence, there will be no statistics to normalize to. Therefore, one has to trust the MC generator prediction as long as the integrated luminosity is too small.

5.5.3 Luminosity Estimation

The luminosity and its error can be estimated counting Z bosons, hence dimuon pairs around the Z mass. From MC and for 100 pb^{-1}, we obtain 1137.7 events from Drell-Yan with $\not{E}_{\text{T}} < 100$ GeV, 44.7 from other backgrounds and not more than 50 from signal. The statistical error on expected number of events of other backgrounds plus possible signal is thus $\sigma_{\text{stat}} = \sqrt{1140 + 47 + 51} = 35.2$ events, which corresponds to 3.1%. A crude estimate for the systematic uncertainty of the luminosity is derived by estimating how precisely other backgrounds can be subtracted from Z contribution. These 100 events on top of the 1100 from Z may be wrong by 30%. This results in relative systematic uncertainty of $\sigma_{\text{sys}} = 0.3 * 100/1100 = 2.7\%$. Adding the two errors in quadrature results in $\sigma_{\mathcal{L}} = 4.1\%$. Conservatively 5% has been used in this analysis.

5.6 The Discovery and Exclusion Limit

The HybridCalculator derives the negative log-likelihood ratio for data according to the different points in unparticle parameter space and for the SM. Fig. 5.15 shows the difference of the two medians in $-2 \ln Q$-space divided by the sum of the two RMS values, defined as Y,

$$Y = \frac{\langle \mathcal{P}_b(x) \rangle - \langle \mathcal{P}_{s+b}(x) \rangle}{RMS_b + RMS_{sb}}, \tag{5.17}$$

where $\langle \mathcal{P}(x) \rangle$ is the median of corresponding the model. The plots show how well the two hypotheses differ from each other for parameter space points within the red-yellow-green region for 100 pb^{-1} and 1 fb^{-1} using $\not{E}_{\text{T}}$ (top/middle). On the very left side and in the upper right corner no difference to the SM can be detected (violet). For the bottom plot, the Z p_{T} was used as input for 1 fb^{-1}. The discrimination is much worse. Therefore, exclusion limits and discovery potential are only shown for $\mathcal{L}_{\text{int}} = 1$ fb^{-1}.

It is remarkable, that all three plots have the same topology. The cross section as a function of $d_{\mathcal{U}}$ and $\Lambda_{\mathcal{U}}$ follows the same topology. It can be concluded, that the kinematics do not change much over parameter space and that the exclusion and discovery reach is mainly cross section dependent.

The interpolation used for this and following plots works as follows: First, known points (X, Y, Z) are collected in a TGraph2D object. TGraph2D then linearly interpolates a Z value for any (X, Y) point by joining the existing points to form Delaunay triangles [94] in (X, Y). These are then used to define flat planes in (X, Y, Z).

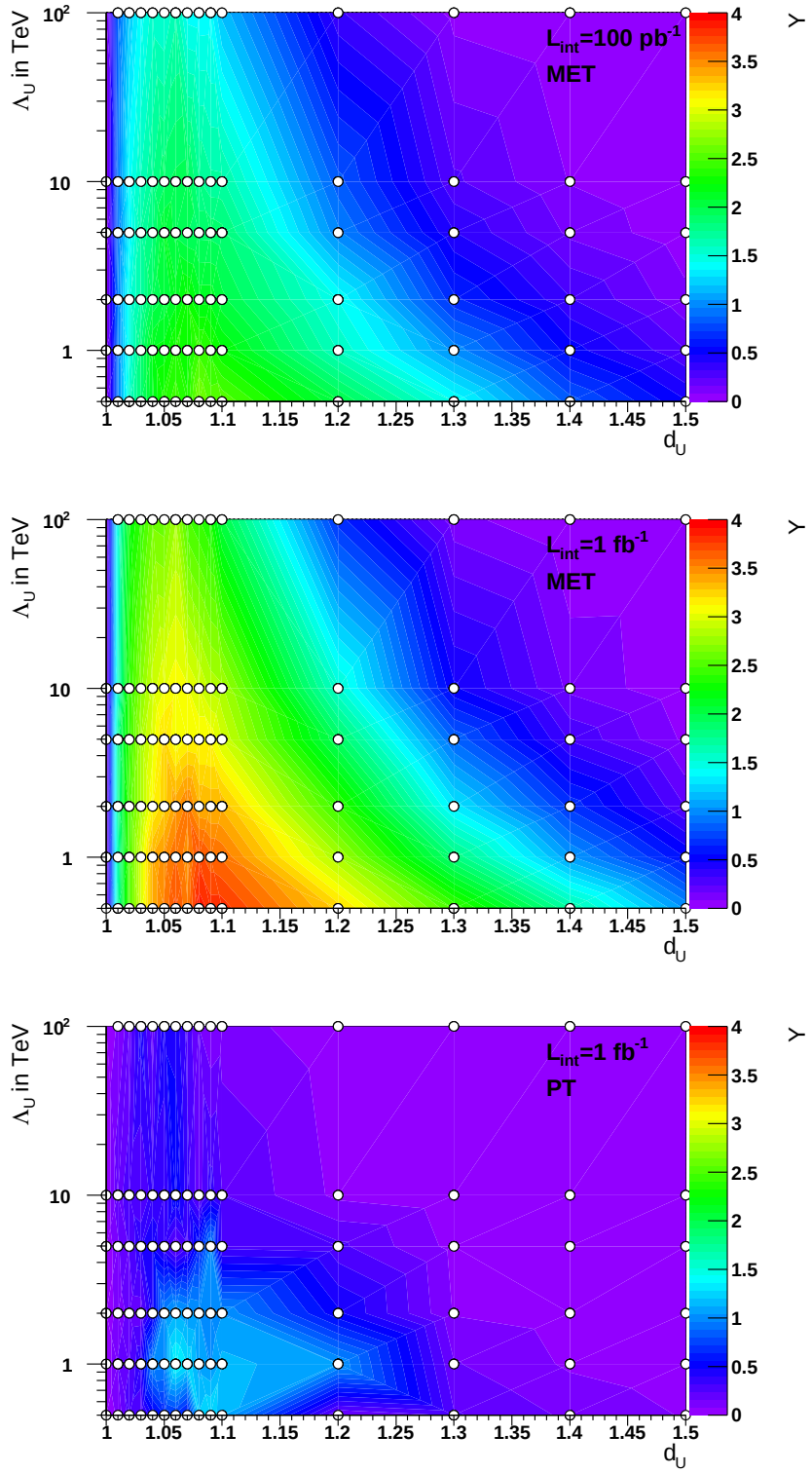

Figure 5.15: *The difference* $(\langle \mathcal{P}_b(x) \rangle - \langle \mathcal{P}_{s+b}(x) \rangle)$ *divided by* $(RMS_b + RMS_{sb})$ *is shown for 100* pb^{-1} *(top) and 1* fb^{-1} *(middle) using* $\not{E}_{\mathrm{T}}$ *as input for the statistical test. The bottom plot shows the same quantity for 1* fb^{-1} *using* p_{T} *as input.*

5.6.1 The Exclusion Limit for $\not{E}_T$

The exclusion limit using $\not{E}_T$ as input is calculated for two different values of integrated luminosity – 100 pb^{-1} and 1 fb^{-1} – taking into account all non-negligible systematic uncertainties. For the case of no signal, a limit is set at 95% CL, stating that a realization of the unparticle model at this parameter space point can be excluded at least at the 95% CL. As explained in Sec. 5.3 CL_s is a measure for the false exclusion rate. In Fig. 5.16 (top) CL_s is plotted as a function of $d_{\mathcal{U}}$ and $\Lambda_{\mathcal{U}}$. The contour of the expected central 95% CL limit is shown with its statistical 1σ error band in Fig. 5.16 (bottom). Both plots are done for 100 pb^{-1}. Again, they follow the topology of the cross section plot. For $\Lambda_{\mathcal{U}} = 2$ TeV a limit on $d_{\mathcal{U}}$ can be set

$$1.01 < d_{\mathcal{U}} < 1.24 \quad \text{at 95\% CL for 100 pb}^{-1}. \tag{5.18}$$

The published LHC luminosity performance foresees to collect not more than ≈ 110 pb^{-1} at 10 TeV center-of-mass energy in the first run, cf. Tab.3.1. However, it is valuable to study how the exclusion limits scale with increasing luminosity, as a ramp-up to 14 TeV is a major challenge and could be delayed leading to more integrated luminosity at lower center-of-mass energy. Consequently, the study has been carried out for 1 fb^{-1} as well, shown in Fig. 5.17. Then, for $\Lambda_{\mathcal{U}} = 2$ TeV a limit on $d_{\mathcal{U}}$ can be set

$$1.01 < d_{\mathcal{U}} < 1.40 \quad \text{at 95\% CL for 1 fb}^{-1}. \tag{5.19}$$

5.6.2 The Discovery Limit for $\not{E}_T$

Going further, the discovery reach is presented analyzing the false discovery rate over unparticle parameter space. In Sec. 5.3 was argued that $1 - CL_b$ is a good measure for it. Again, two integrated luminosities have been studied, 100 pb^{-1} and 1 fb^{-1}, and the same systematic uncertainties as in the exclusion limit case were considered. Here[10], $\log(1-CL_b)$ is shown on a linear scale rather than $1 - CL_b$ on a logarithmic scale. The one-sided 5σ (3σ) limit corresponds to -6,54 (-2.86). Hence, $\log(1 - CL_b)$ is plotted as function of $d_{\mathcal{U}}$ and $\Lambda_{\mathcal{U}}$ in Fig. 5.18 (top) for 100 pb^{-1} and the contour plot is given in Fig 5.18 (bottom).

It is clear from Fig. 5.18 that an unparticle signal can be discovered at the desired 5σ CL. A combined search with the electron channel would increase sensitivity even more. Hence, unparticles can be discovered in early data. With more data, the discovery reach increases, see Fig. 5.19. For $\Lambda_{\mathcal{U}} = 1$ TeV an unparticle signal can be established for

$$1.05 < d_{\mathcal{U}} < 1.12 \quad \text{at a one-sided } 5\sigma \text{ CL for 100 pb}^{-1} \tag{5.20}$$

and for

$$1.02 < d_{\mathcal{U}} < 1.34 \quad \text{at a one-sided } 5\sigma \text{ CL for 1 fb}^{-1}. \tag{5.21}$$

[10] due to a bug in ROOT

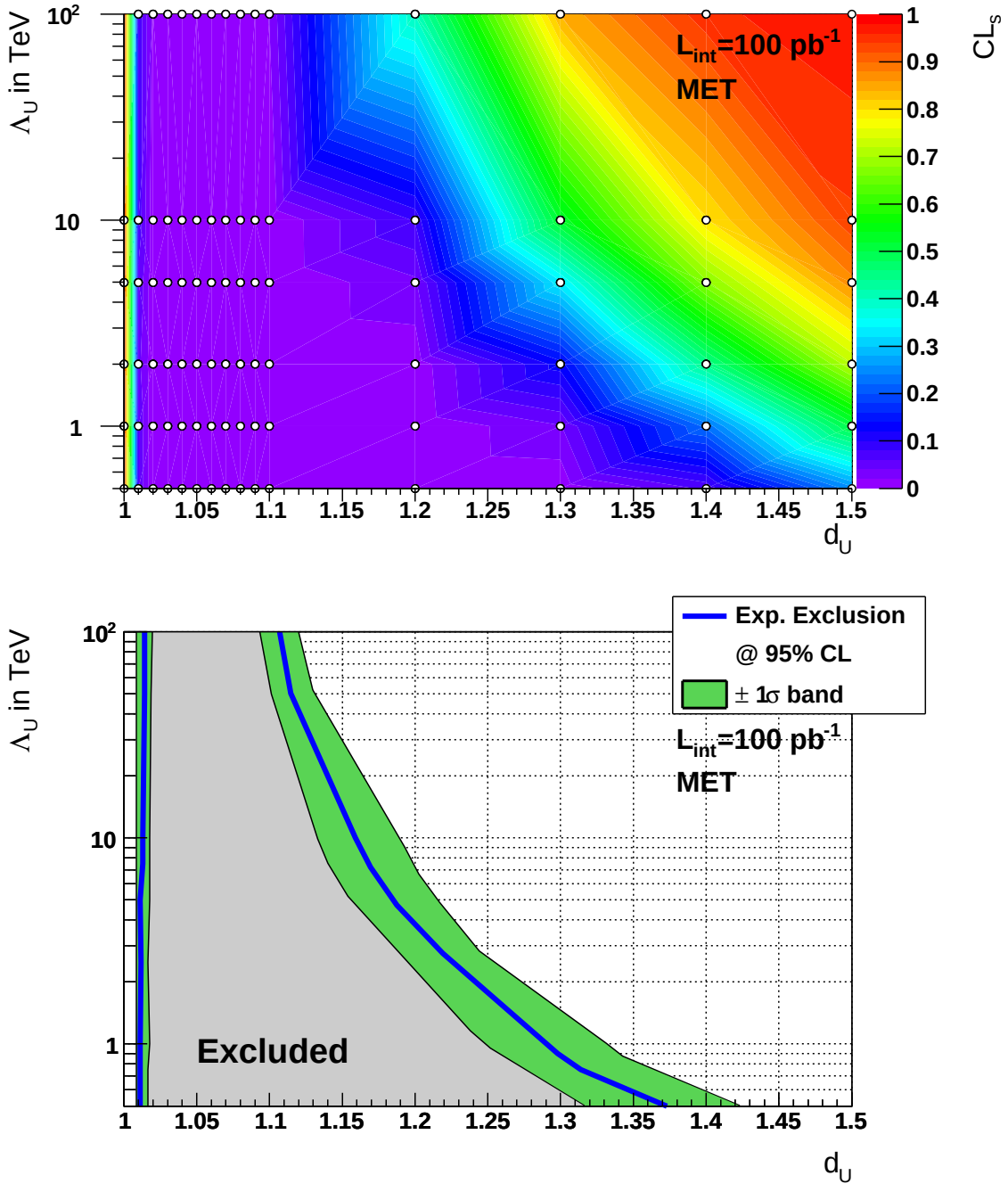

Figure 5.16: *CL_s as a function of $d_{\mathcal{U}}$ and $\Lambda_{\mathcal{U}}$ for 100* pb^{-1} *using* $\not{E}_{\mathrm{T}}$.

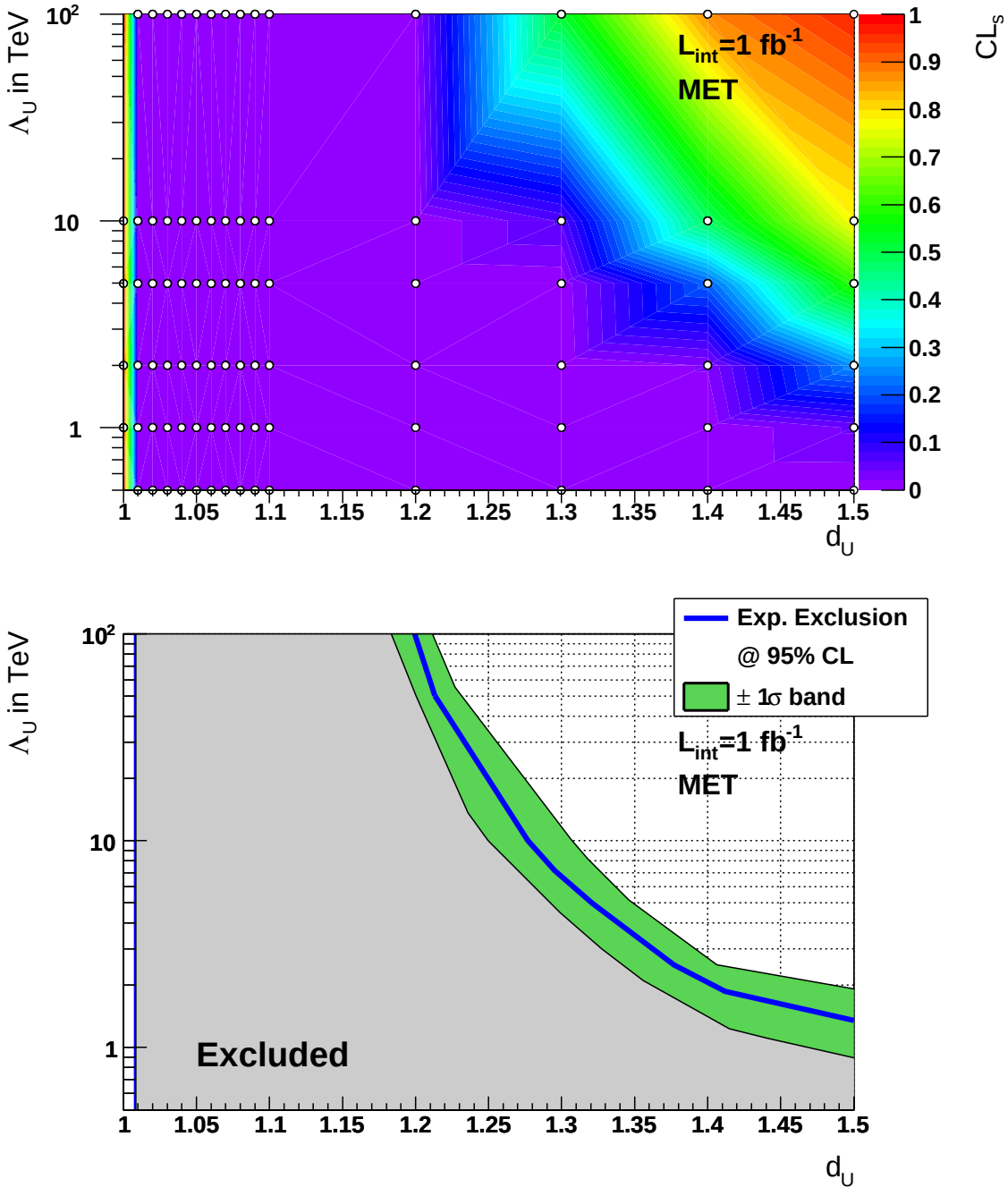

Figure 5.17: *CL_s as a function of $d_{\mathcal{U}}$ and $\Lambda_{\mathcal{U}}$ for 1* fb^{-1} *using* $\not{E}_{\mathrm{T}}$.

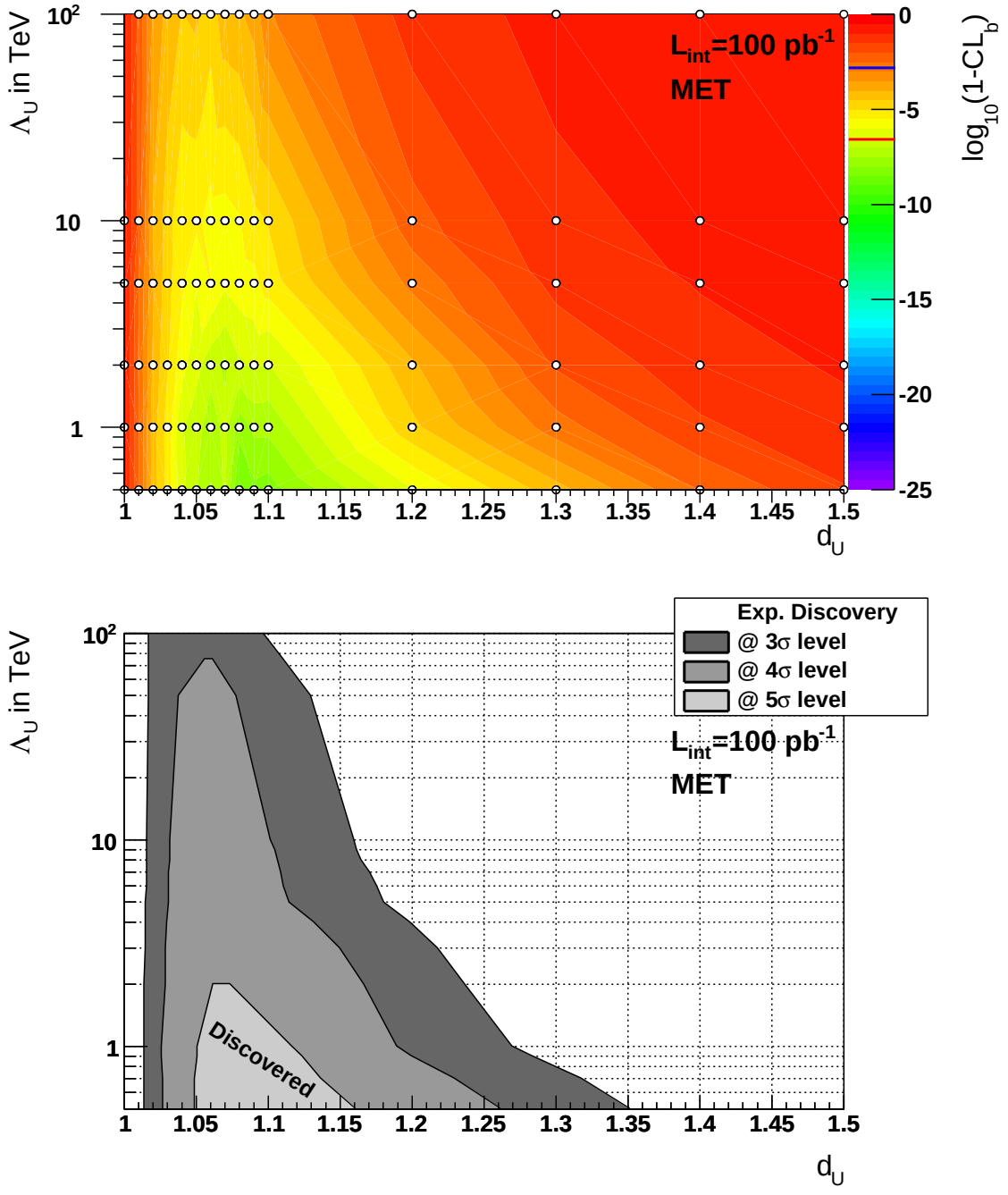

Figure 5.18: $\log(1 - CL_b)$ *as a function of* $d_{\mathcal{U}}$ *and* $\Lambda_{\mathcal{U}}$ *for 100* pb^{-1} *using* $\not{E}_{\text{T}}$.

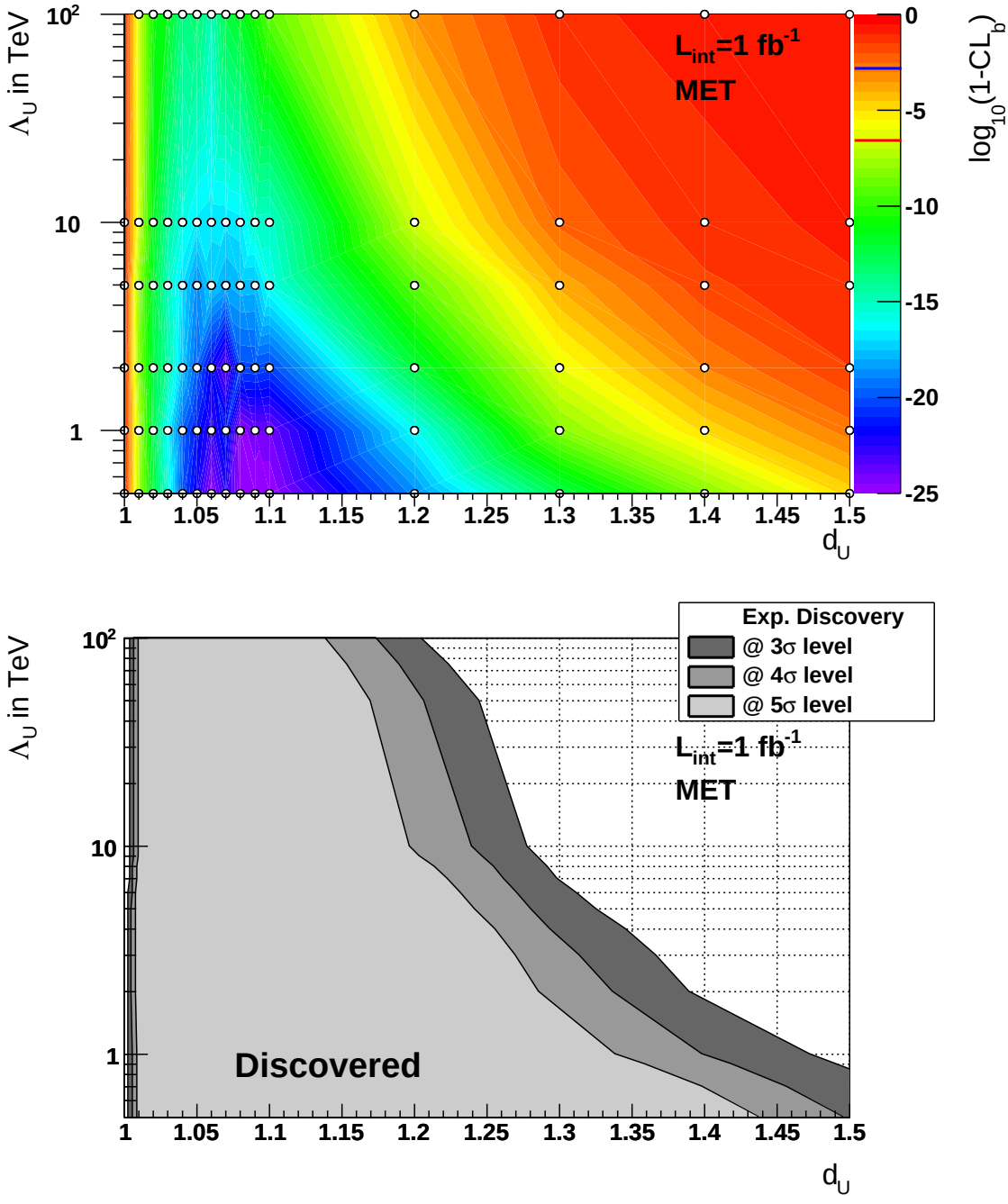

Figure 5.19: $\log(1 - CL_b)$ *as a function of* $d_{\mathcal{U}}$ *and* $\Lambda_{\mathcal{U}}$ *for 1* fb^{-1} *using* $\not{E}_{\text{T}}$.

5.6.3 The Exclusion and Discovery Limit for Z p_{T}

As can be guessed from Fig. 5.15 (bottom), both, the exclusion and the discovery reach, is much smaller, when the Z p_{T} is used as input for the statistical method, because the discrimination power of Z p_{T} is much smaller. For 100 pb^{-1} of integrated luminosity, no limits can be set. For 1 fb^{-1}, the exclusion limit is shown in Fig. 5.20 and the discovery reach in Fig. 5.21. An exclusion limit at 95% CL can only be set for the small violet regions, which roughly include points with $d_{\mathcal{U}}$ =1.07-1.09 and $\Lambda_{\mathcal{U}}$ =0.5-2.0 TeV. A discovery is not possible. The structure of the exclusion limit plot follows again the structure of the cross section plot, but more statistical fluctuations are already remarkable, whereas statistical fluctuations dominate the structure of the discovery plot. This is due to two reasons: On the one hand, there are only a small signal yields, and on the other hand, the region with best discrimination in Z p_{T}, i.e. the high p_{T} bins, are those with smallest statistic and the pdfs already die out with the known "jumping" characteristic.

5.6.4 Comparison to the Diphoton Study

Due to time constraints and the lack of the scalar matrix element in Pythia in the beginning, a full analysis for the scalar case has not been carried out. But a comparison of one parameter point between the diphoton channel and the dimuon channel is possible. In Ref. [30] a virtual unparticle was considered for the process $q\overline{q} \to \mathcal{U} \to \gamma\gamma$ with a virtual, scalar unparticle. Looking at Tab. 1 therein, the parameter space point represented by the second row is chosen. The LO cross section for the signal region – an invariant mass of the two photons between 500 and 1000 GeV– amounts to 0.76 pb. This corresponds to 7.6 signal events in 100 pb^{-1} taking into account the acceptance (10%), a diphoton efficiency (70%) and a k-factor of 1.34. 2.4 background events are expected. A sensitivity of 2.2σ is quoted in Fig. 4 of Ref. [30]. The sensitivity is not higher due to large background uncertainties.

In the scalar case for the process $q\overline{q} \to \mathcal{U} + Z(\mu\mu)$, the inclusive cross section for $\hat{p}_T >$ 50 GeV for the same parameter space point is 39.8 pb at NLO. The muon branching ratio of the Z boson is 0.033, resulting in 131.2 signal events. Assuming the same signal efficiency as in the vector case of 10.3%, leaves 13.5 signal events after all cuts to be compared to 5.7 background events. Be $\sqrt{5.7}$ the statistical error and $5.7 \cdot 20\%$ the systematic uncertainty. This adds up to an uncertainty of 3.5 events. A rough estimate for the sensitivity is $N_{\mathrm{sig}}/\sigma_{bkg}$. This results in a sensitivity of 3.8σ, which is statistically insufficient for a discovery. The sensitivity for the vector case is higher, since the cross section for the process is higher. This is due to the required spin-flip in the scalar case.

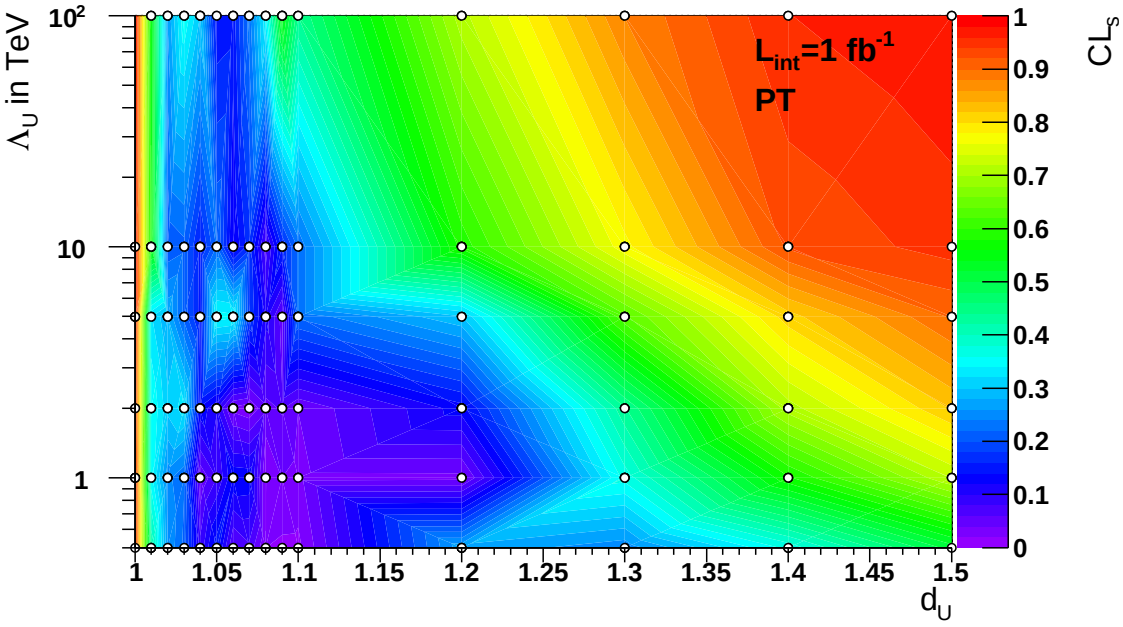

Figure 5.20: *CL_s as a function of $d_{\mathcal{U}}$ and $\Lambda_{\mathcal{U}}$ for 1* fb^{-1} *using Z* p_{T}.

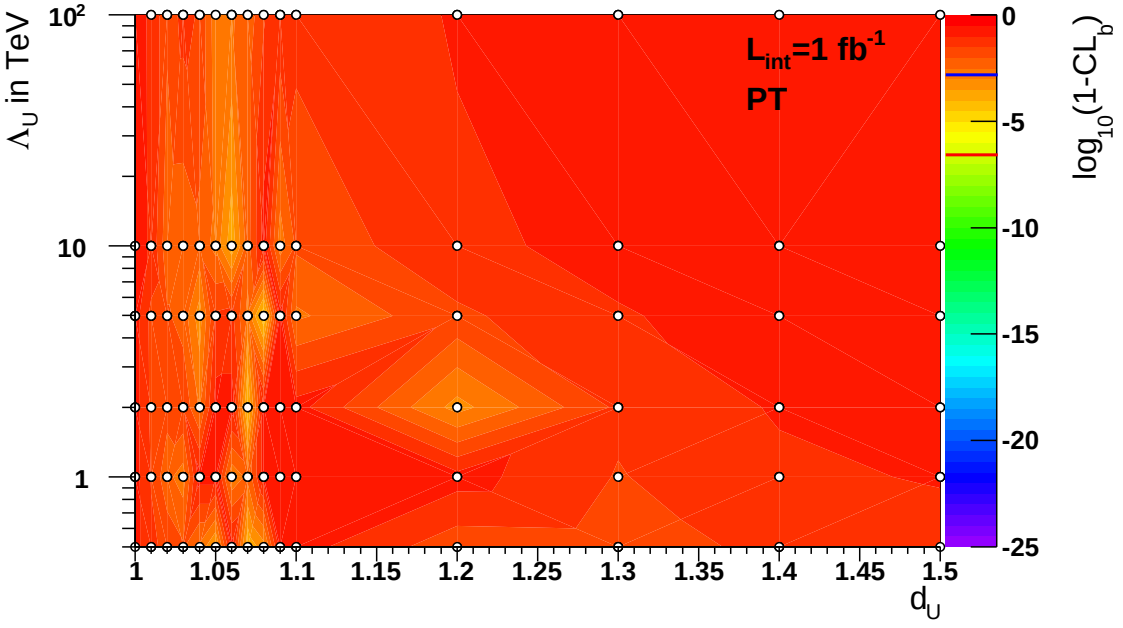

Figure 5.21: $\log(1 - CL_b)$ *as a function of $d_{\mathcal{U}}$ and $\Lambda_{\mathcal{U}}$ for 1* fb^{-1} *using Z* p_{T}.

Chapter 6

Conclusions and Outlook

Within this thesis a MC study for physics beyond the SM with the CMS detector has been presented. Unparticle events have been produced and their detector response has been simulated making use of the CMSSW software framework. All important SM backgrounds have been taken into account. After skimming, an event selection was carried out in order to separate signal from background and the analysis was performed with the HybridCalculator resulting in confidence levels for discovery and exclusion. Within the statistical test, various systematics have been incorporated where necessary, and neglected where possible.

The studied real vector unparticle signal in the process $q\overline{q} \to \mathcal{U}+Z(\mu\mu)$ can be discovered at a 5σ CL for certain regions in the unparticle parameter space with 100 pb^{-1} of data in the channel $\mu^+\mu^- + \not{E}_{\text{T}}$. In the absence of a signal, exclusion limits can be set for a wider range. The p_{T} analysis showed a much worse sensitivity and no discovery can be claimed, not even with 1 fb^{-1}. The discovery and exclusion potential of course increases with the collected amount of data. At LHC design conditions with higher beam energies and luminosities the discovery reach will be even larger.

A further optimization for every parameter space point could gain sensitivity. The electron channel is another possible source to increase sensitivity. As well a combination of the $\not{E}_{\text{T}}$ and the p_{T} analysis could be performed, but real data has to prove if this is feasible. At present it is unclear, whether the uncertainties from the p_{T} analysis would spoil the result of the $\not{E}_{\text{T}}$ analysis.

Recently, the scalar matrix element for the process $q\overline{q} \to \mathcal{U} + Z$ has been included in Pythia8. A full study of this process should now be carried out and compared to the existing $q\overline{q} \to \mathcal{U} \to \gamma\gamma$ study.

Appendix A

Unparticle Event Displays

Unparticle events visualized with FIREWORKS are shown in the $r - \phi$-plane. The reconstructed muon trajectories and the muon stations with simulated hits inside are colored red, missing transverse energy is pink and a jet in the second picture is green. The red and blue entries around the jet are the ECAL and HCAL depositions. The inner blue circle represents the inner tracker and reconstructed tracks appear in light green. Low p_{T} particles are omitted.

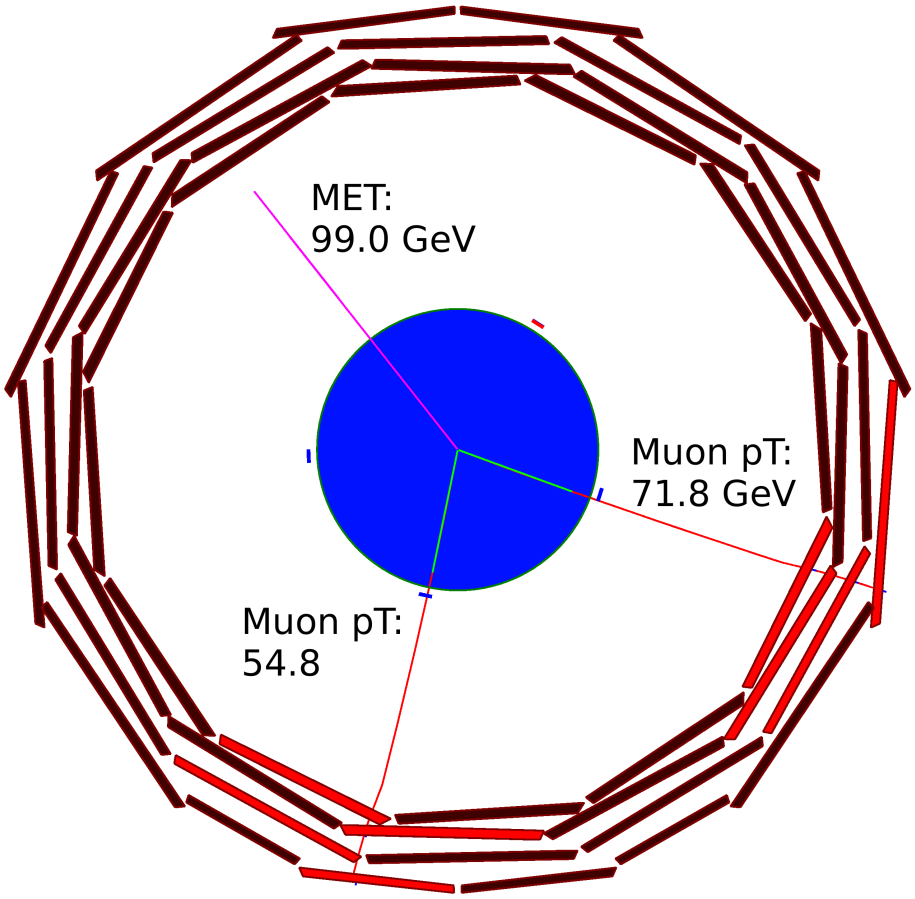

Figure A.1: *An unparticle event with two muons and missing transverse energy.*

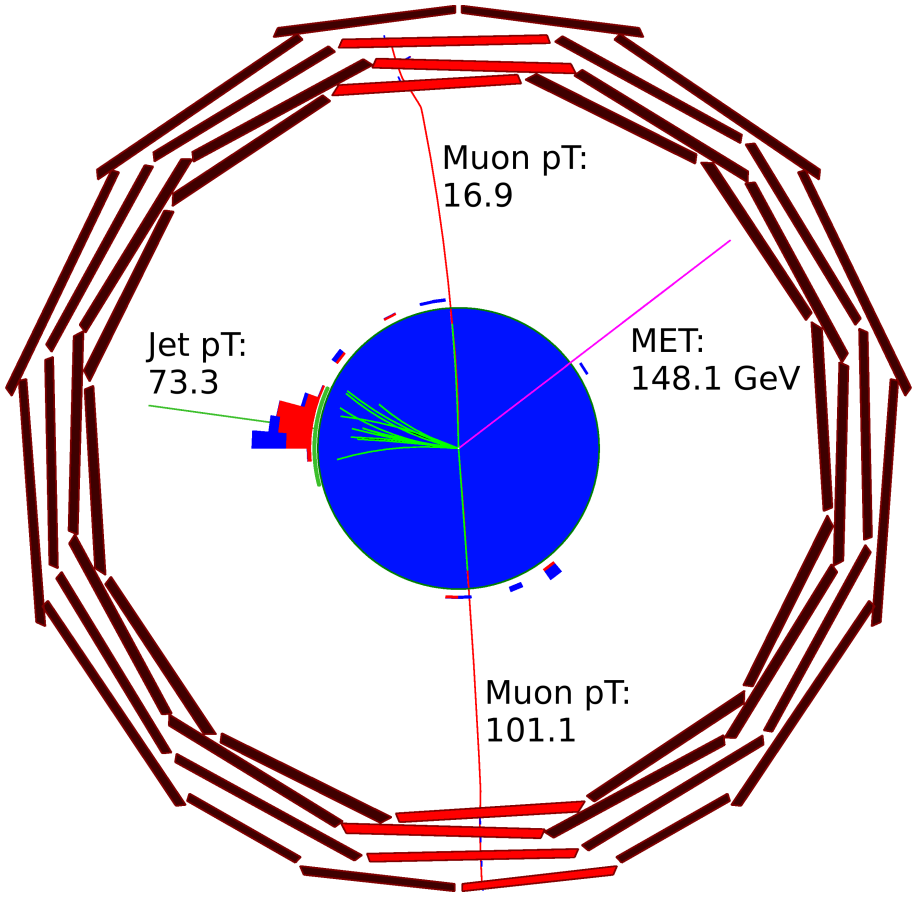

Figure A.2: *An unparticle event with two muons, missing transverse energy, and one jet.*

Appendix B

Different Fits to $\mathcal{P}_b$

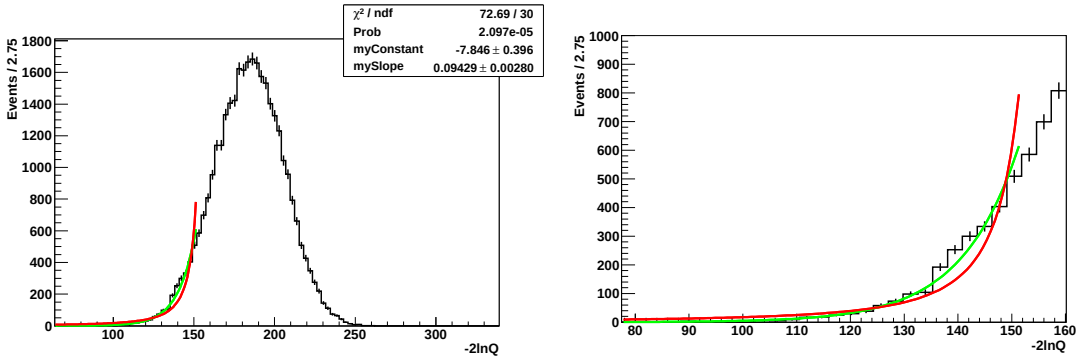

Figure B.1: *The exponential fit (green) and the rational function fit (red) to $\mathcal{P}_b$ is shown. A χ^2/ndf of 2.4 is found for the exponential and 59.3 for the other. The right plot is a zoom into the tail of the left plot.*

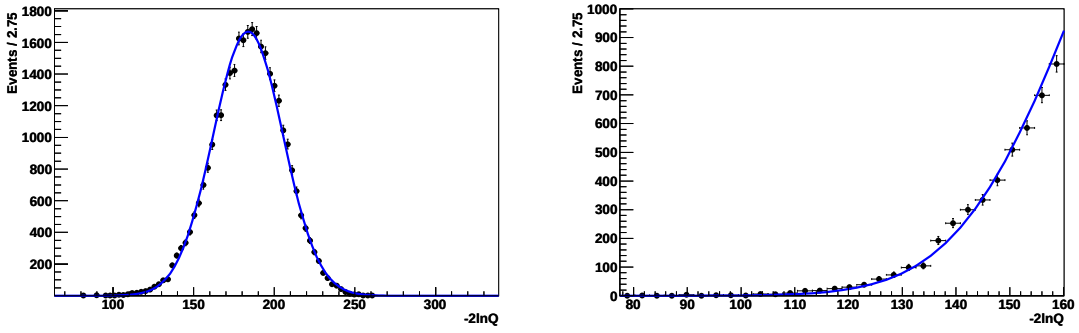

Figure B.2: *The Voigtian fit (blue) to $\mathcal{P}_b$ is shown. A χ^2/ndf of 1.5 is found. The right plot is a zoom into the tail of the left plot.*

Appendix C

Samples

The used samples can be found on DBS. The background samples are:

- /Zjets-madgraph/Winter09_IDEAL_V11_FastSim_v1/GEN-SIM-DIGI-RECO,
- /ZZ_2l2n/Summer08_IDEAL_V11_redigi_v1/GEN-SIM-RECO,
- /ZZ_4l/Summer08_IDEAL_V11_redigi_v1/GEN-SIM-RECO,
- /WZ_inclu/Summer08_IDEAL_V11_redigi_v1/GEN-SIM-RECO,
- /TTJets-madgraph/Fall08_IDEAL_V11_redigi_v10/GEN-SIM-RECO,
- /WJets-madgraph/Summer08_IDEAL_V11_redigi_v1/GEN-SIM-RECO,
- /WW/Summer08_IDEAL_V11_redigi_v1/GEN-SIM-RECO,
- /QCDptXX/Summer08_IDEAL_V11_redigi_v3/GEN-SIM-RECO, with XX ranging from 15 to 3000

The signal samples can be found on ph_analysis_02 servers and are called:

- /Unparticle_dU_LU/jansen-Unparticle_dU_LU_RECO- // bfb9b1ca5534929b93d8c7d7bdccf0e7/USER,

where dU and LU have to be replaced according to the parameter space point under study. 90 samples are available.

Bibliography

[1] A. Maslow, *"A Theory of Human Motivation"*, Psychological Review **50**(4) (1943):370-96.

[2] S.L. Glashow, Nucl. Phys. **22** (1961) 579.

[3] S. Weinberg, Phys. Rev. Lett. **19** (1967) 1264.

[4] S.L. Glashow, J. Iliopoulos and L. Maiani, Phys. Rev. **D2** (1970) 1285.

[5] A. Pich, *"Aspects of Quantum Chromodynamics"*, arXiv: 0001118 [hep-ph].

[6] DESY. TESLA - An International, Interdisciplinary Center for Research, 2001, `http://tesla.desy.de/new_pages/TDR_CD/brochure/`.

[7] F. Halzen, A. D. Martin, *"Quarks and Leptons: An Introductory Course in Modern Particle Physics"*, John Wiley & Sons, 1984.

[8] Particle Data Group, *"Particle Data Book"*, Phys. Lett. B **667**, 1 (2008).

[9] W.-M. Yao et al., *"Review of Particle Physics"*, J. Phys. **G33** (2006) 1.

[10] ALEPH Collaboration, `http://aleph.web.cern.ch/aleph/dali/Z0_examples.html`.

[11] ALEPH, DELPHI, L3 and OPAL *"The LEP Working Group for Higgs Boson Searches"*, arXiv: 0306033 [hep-ex].

[12] The CDF and DØ Collaborations, *"Combined CDF and DØ Upper Limits on Standard Model Higgs-Boson Production with up to 4.2* fb^{-1} *of Data"*, FERMILAB-PUB-09-060-E.

[13] S. Martin, *"A Supersymmetry Primer"*, arXiv: 9709356v5 [hep-ph].

[14] P. Ginsparg, *"Applied Conformal Field Theory"*, Lectures given at Les Houches summer session, arXiv: 9108028 [hep-th].

[15] B. Grinstein, K. Intriligator, I. Rothstein, *"Comments on Unparticles"*, arXiv: 0801.1140 [hep-ph].

[16] J. Polchinski, *"SCALE AND CONFORMAL INVARIANCE IN QUANTUM FIELD THEORY"*, Nucl. Phys. B **303**, 226 (1988).

[17] private communications with H. Georgi.

[18] S. Coleman, J. Mandula, *"ALL POSSIBLE SYMMETRIES OF THE S MATRIX"*, Phys. Rev. **159**, 1251 (1967).

[19] H. Georgi, *"Unparticle Physics"*, Phys. Rev. Lett. **98**, 221601 (2007).

[20] H. Georgi, *"Another Odd Thing About Unparticle Physics"*, Phys. Lett. B **650**, 275 (2007).

[21] H. Georgi, Y. Kats, *"An Unparticle Example in 2D"*, arXiv: 0805.3953v1 [hep-ph].

[22] M. Strassler, *"Why Unparticle Models with Mass Gaps are Examples of Hidden Valleys"*, arXiv: 0801.0629 [hep-ph].

[23] J.J. van der Bij, S. Dilcher *"HEIDI and the unparticle"*, Phys. Lett. B **655**: 183-184 (2007).

[24] T. Banks and A. Zaks, *"On the Phase Structure of Vector-Like Gauge Theories with Massless Fermions"*, Nucl. Phys. B **196** (1982) 189.

[25] J. Blümlein, V. Ravindran, W. van Neerven, *"Relations among polarized and unpolarized splitting functions beyond leading order"*, arXiv: 9806355v1 [hep-ph].

[26] K. Cheung, W.-Y. Keung and T.-C. Yuan, *"Collider Phenomenology of Unparticle Physics"*, Phys. Rev. D **76** (2007) 055003 .

[27] M. A. Stephanov, *"Deconstruction of Unparticles"*, arXiv: 0705.3049 [hep-ph].

[28] T. Sjostrand et al, *"PYTHIA 8.1"*, `http://home.thep.lu.se/~torbjorn/Pythia.html`.

[29] K. Cheung, *"Unparticle Phenomenology - A Mini Review"*, arXiv: 0809.0995 [hep-ph].

[30] The CMS Collaboration, *"Search for Unparticles in the Diphoton Final State"*, CMS PAS EXO-09-011.

[31] H. Georgi, *"Unparticle self-interaction"*, arXiv: 0904.1962 [hep-ph].

[32] V. Barger et al., *"Unparticle physics with broken scale invariance"*, arXiv: 0801.3771 [hep-ph].

[33] private communications with W.-Y. Keung.

[34] The LEP Collaborations ALEPH, DELPHI, L3 and OPAL and the LEP Electroweak Working Group, arXiv: 0612034 [hep-ex], `http://www.cern.ch/LEPEWWG`.

[35] The ALEPH, DELPHI, L3, OPAL and SLD Collaborations, the LEP Electroweak Working Group and the SLD Electroweak and Heavy Flavour Groups, Phys. Rept. 427 (2006) 257.

[36] I. Gogoladzea, N. Okadab, Q. Shafi, *"Unparticle physics and gauge coupling unification"*, Physics Letters B Volume 659 (2008) 357-360.

[37] D. Stancato, J.Terning, *"The Unhiggs"*, arXiv:0807.3961 [hep-ph].

[38] M. Luo, W. Wu, G. Zhu *"Unparticle physics and A_{FB}^b on the Z pole"*, Phys. Lett. B **659** (2008) 349-356.

[39] T. Kikuchi, N. Okada *"Unparticle Dark Matter"*, arXiv:0711.1506 [hep-ph].

[40] Lyndon Evans and Philip Bryant (editors), *"LHC Machine"*, JINST **3** S08001, 2008.

[41] `http://puhep1.princeton.edu/mumu/physics/`.

[42] C. Hof, *"Implementation of a Model-Independent Search for New Physics with the CMS Detector exploiting the World-Wide LHC Computing Grid"*, PhD Thesis, RWTH Aachen University, (2009).

[43] `http://atlas.web.cern.ch/Atlas/index.html`.

[44] `http://totem.web.cern.ch/Totem/`.

[45] `http://lhcb.web.cern.ch/lhcb/`.

[46] `http://aliceinfo.cern.ch/Collaboration/index.html`.

[47] P. Landshoff, *"The total cross section at the LHC"*, arXiv: 0709.0395 [hep-ph].

[48] CERN, CERN Photo Data Base, http://cdsweb.cern.ch.

[49] LHC Designreport, Vol. 1,2,3, `http://lhc.web.cern.ch/lhc/LHC-DesignReport.html`.

[50] `http://lhc-commissioning.web.cern.ch/lhc-commissioning/luminosity/09-10-lumi-estimate.htm`.

[51] `http://cms.web.cern.ch/cms/index.html`.

[52] The CMS Collaboration, S Chatrchyan et al., *"The CMS experiment at the CERN LHC"*, JINST **3** S08004, 2008.

[53] CMS Magnet Technical Design Report, `http://cmsdoc.cern.ch/cms/TDR/MAGNET/magnet.html`.

[54] CMS Tracker Technical Design Report, `http://cmsdoc.cern.ch/cms/TDR/TRACKER/tracker.html`.

[55] CMS ECAL Technical Design Report, `http://cmsdoc.cern.ch/cms/TDR/ECAL/ecal.html`.

[56] CMS HCAL Technical Design Report, `http://cmsdoc.cern.ch/cms/TDR/HCAL/hcal.html`.

[57] C. Grupen, *"Teilchendetektoren"*, BI-Wiss.-Verl., Mannheim (1993).

[58] D. Acosta, M. Della Negra, *"CMS physics : Technical Design Report"*, CERN-LHCC-2006-001 .

[59] CMS Moun Technical Design Report, `http://cmsdoc.cern.ch/cms/TDR/MUON/muon.html`.

[60] CMS Trigger Technical Design Report, http://cmsdoc.cern.ch/cms/TDR/TRIGGER-public/trigger.html.

[61] R. Frühwirth, *"Application of Kalman filtering to track and vertex fitting"*, Nucl. Instrum. Meth. A 262, 444 (1987), http://dx.doi.org/10.1016/0168-9002(87)90887-4.

[62] E. James et al, *"Muon Identification in CMS"*, CMS NOTE 2006/010.

[63] T. Hebbeker, *"Lecture notes on: Elementary Particle Physics"*, http://web.physik.rwth-aachen.de/~hebbeker/home_teaching.html.

[64] http://www.physics.utoronto.ca/research/subatomic/hep/events/images/.

[65] G. Salam, G. Soyez, *"A practical Seedless Infrared-Safe Cone jet algorithm"*, arXiv: 0704.0292v2 [hep-ph].

[66] The CMS Collaboration, *"Plans for Jet Energy Corrections at CMS"*, CMS PAS JME 2007/002.

[67] The CMS collaboration, *"$\not\!\!E_{\mathrm{T}}$ Reconstruction, Performance and Validation"*, CMS AN-2008/089 (2008).

[68] The CMS collaboration, *"$\not\!\!E_{\mathrm{T}}$ Performance in CMS"*, CMS AN-2007/041 (2007).

[69] https://twiki.cern.ch/twiki/bin/view/CMS/DBS-TDR.

[70] S. Ask, *"Simulation of Z plus Graviton/Unparticle Production at the LHC"*, arXiv: 0809.4750 [hep-ph].

[71] private communication with S. Ask.

[72] http://cmssw.cvs.cern.ch/cgi-bin/cmssw.cgi/CMSSW/IOMC/.

[73] The CMS Collaboration, *"MUSiC - An Automated Scan for Deviations between Data and Monte Carlo Simulation"*, CMS PAS EXO-08-005 (2008).

[74] S. Schmitz, *"Model Unspecific Search for New Physics with High p_{T} Photons in CMS"*, Diploma thesis, RWTH Aachen University, (in preparation).

[75] M. C. Kumar, Prakash Mathews, V. Ravindran, Anurag Tripathi, *"Unparticles in diphoton production to NLO in QCD at the LHC"*, Phys. Rev. D **79**, 075012 (2009).

[76] private communications with V. Ravindran.

[77] N.Adam et al, *"Towards a Measurement of the Inclusive W (ev) and Z (ee) Cross Sections in pp Collisions at $\sqrt{s} = 10$ TeV."*, CMS AN 2009/098.

[78] J. Andreas et al, *"Measurement of the $t\bar{t}$ cross section in the dilepton channels with L = 100 pb^{-1} using the CMS detector at $\sqrt{s} = 10$ TeV"*, CMS AN 2009/047.

[79] H. Pieta, *"Scale induced cross section uncertainties"*, https://twiki.cern.ch/twiki/bin/view/CMS/AachenScaleUncertainties.

[80] https://twiki.cern.ch/twiki/bin/view/CMS/MuonPOG.

[81] The CMS Collaboration, *"Studies of CMS Muon Reconstruction Performance with Cosmic Rays"*, CMS PAPER CFT 2009/014 (in preperation).

[82] The CMS Collaboration, *"Determination of the jet energy scale using* $Z \rightarrow e^+e^-$ *+ jet* p_{T} *balance and a procedure for combining data-driven corrections"*, CMS JME 2009/005.

[83] G. Cowan, *"Statistical Data Analysis"*, Oxford University Press, New York, 1998.

[84] A. L. Read, *"Modified Frequentist Analysis of Search Results (The* CL_s *Method)"*, Prepared for Workshop on Confidence Level, Geneva, Switzerland, (2000).

[85] A.L. Read, *"Presentation of search results: the* CL_s *technique"*, Nucl. Part. Phys. **28** (2002) 2693-2704.

[86] E. Gross, Al. L. Read, *"Prospects for Standard Model Higgs Search in the LEP 2000 run"*, Proceedings of 14th Rencontres de Physique de la Valle d'Aoste, (2000).

[87] D. Piparo and G. Schott, *"HybridCalculator class"*, http://root.cern.ch/root/html/RooStats__HybridCalculator.html.

[88] http://root.cern.ch/drupal/content/roofit.

[89] ROOT, a Data Analysis Framework, http://root.cern.ch/drupal/.

[90] Private communications with A. L. Read.

[91] S. Brandt, *"Statistical and Computational Methods in Data Analysis"*, Springer New York, 1997.

[92] V. Bartsch, G.Quast, *"Expected signal observability at future experiments"*, CMS NOTE 2005/004 (2005).

[93] W. J. Metzger, *"Statistical Methods in Data Analysis"*, http://www.hef.kun.nl/~wes/stat_course/statist_2002.pdf (2002).

[94] B. Delaunay, *"Sur la sphère vide"*, Bulletin of Academy of Sciences of the USSR **7** (1934), Nr. 6, S. 793-800.

List of Figures

List of Tables

Danksagung

So, ich bin dann mal weg.

Vorher möchte ich aber meinen Kollegen des III. Physikalischen Instituts danken, ohne deren Mithilfe diese Diplomarbeit nicht möglich gewesen wäre. Danke euch allen. Einen besonderen Dank gilt meinen "direkten Anlaufstellen", die da wären Carsten M., Markus M., Arnd M., Carsten H., Kerstin H., Metin A., Walter B. und Stefan S. Die unzähligen Diskussionen und Unterhaltungen über verschiedenste Aspekte und Themen sind wohl die Momente, in denen man am meisten lernt.

Ein großer Dank geht auch an die Computing-Leute: Michal B., Andreas N. und Thomas K., ohne die der Betrieb im Institut wohl lahmliegen würde.

Viele Vorträge habe ich gehalten in den letzten Monaten, sei es im CMS IIIA Meeting, im Freitagsseminar, oder auswärts im EXOTICA Meeting oder auf Tagungen und Konferenzen. Vielen Dank an T. Hebbeker, Arnd M. für das Korrekturlesen der Präsentationen. Danke an die Mitglieder der EXOTICA-Gruppe für wertvolle Kommentare.

Das Konzentrat meiner Diplomarbeit ist in einer CMS Analysis Note zusammengefasst. Vielen Dank an Arnd M., T. Hebbeker, Albert d.R., Greg L. fürs Gegenlesen.

Am Anfang meiner Diplomandenzeit war gar nicht klar, ob das gewählte Thema realisierbar ist. Einen MC Generator gab es zu diesem Zeitpunkt nicht für Unparticle-Ereignisse. Dank Stefan A. konnte das Thema aber in Angriff genommen werden.

Am Ende einer Diplomarbeit steht immer das große Korrekturlesen an. Ohne Korrekturen von T. Hebbeker, Arnd M., Casten M., Carsten H., Markus M., Kerstin H. wäre die Arbeit nicht, wie sie ist. Vielen Dank dafür.

Zum Schluss, aber nicht zuletzt, geht der größte Dank an meine liebe Familie und Freunde. Reiner, Hiltrud, Willem und Wibke, vielen Dank für eure Unterstüzung während der gesamten Studienzeit. Meine Freunde haben mich in den letzten Wochen vielleicht seltener gesehen als sonst, aber wenn doch, dann war es ihnen ein Leichtes, mich von meiner Diplomarbeit abzulenken. Meiner Freundin Christine möche ich in tiefster Zuneigung danken. Du wunderbarer Mensch. Deine Liebe machte den Stress unvergessen.